ENHANCED SUPERCONDUCTING PROPERTIES OF IRON CHALCOGENIDE THIN FILMS

A Dissertation

by

LI CHEN

Submitted to the Office of Graduate Studies of
Texas A&M University
in partial fulfillment of the requirements for the degree of

DOCTOR OF PHILOSOPHY

Chair of Committee,	Haiyan Wang
Committee Members,	Karl Hartwig
	Tahir Cagin
	Xinghang Zhang
Intercollegiate Faculty Chair,	Ibrahim Karaman

August 2013

Major Subject: Materials Science and Engineering

ABSTRACT

Among the newly discovered iron-based superconductor, FeSe with the simplest structure and a transition temperature (T_c) around 8 K arouses much research interest. Although its T_c is much lower than that of the cuprates, iron chalcogenide has low anisotropy, slow decrease of the critical current density (J_c) with increasing magnetic field and high upper critical field H_{c2} as well as easy composition control, which makes it a promising candidate to substitute NbSn/NbTi for high field applications. Compared with its bulk counterpart, iron-based superconductor thin film has a great potential in developing the ordered quasi-2D structure and is suitable for coating technology which has already been applied in $YBa_2Cu_3O_{7-x}$ coated conductors.

In this thesis, we first optimized pure FeSe thin films by different growth conditions using pulsed laser deposition (PLD) and post-annealing procedures. The microstructure properties of the films including the epitaxial quality, interface structure and secondary phase have been studied and correlated with the superconducting properties.

Second, we reported our initial attempt on introducing the flux pinning centers into $FeSe_{0.5}Te_{0.5}$ thin films either under a controlled oxygen atmosphere or with a thin CeO_2 interlayer. The microstructure of the $FeSe_{0.5}Te_{0.5}$ films including the epitaxial quality, the interface structure and the secondary phase have been studied and correlated with the in-field performance of the superconducting thin films to explore the pinning properties of these nanoscale defects.

Very recently, ion beam assisted deposition (IBAD) substrates have been used to grow high quality $FeSe_{0.5}Te_{0.5}$ tape with excellent in-field performance. The film on IBAD substrate involves multiple steps of seed layer and buffer layer deposition to establish the epitaxial growth template. Therefore a simplified and cost effective iron-based coated conductor is more desirable. Towards the practical application, we demonstrated the growth of superconducting $FeSe_{0.5}Te_{0.5}$ film on amorphous glass substrates for the first time. The film is highly textured with excellent superconducting properties, e.g., T_c of 10 K and J_c under self-field as high as 1.2×10^4 A/cm^2 at 4 K. Further optimization of the film growth with various nanoscale interlayers has been carried out.

In addition the Te rich iron chalcogenide thin film with composition close to the composition with antiferromagnetic (AFM) transition has been demonstrated. Compared to the $FeSe_{0.5}Te_{0.5}$ which claimed to be the optimum composition from the literature report, the $FeSe_{0.1}Te_{0.9}$ is even more promising for the high field application with its coexistence of super high upper critical field and high critical current density.

DEDICATION

Dedicated to my parents, my wife and my son

ACKNOWLEDGEMENTS

I would like to express my deepest appreciation to my advisor, Prof. Haiyan Wang. In the four years of Ph.D. study, she gave me lots of guidance and great advices on my research topic. She showed me the way to do research and helped me to build a rigid work style. I appreciate the great training opportunities provided by my advisor on the equipment, experimental design and process control, which are all important to my career in Materials Science and Engineering. Her effort and great personality make the group like a family, and I enjoyed every day in the labs and office and working with excellent students all over the world.

I thank all my committee members, Dr. Karl Hartwig, Dr. Tahir Cagin and Dr. Xinghang Zhang for their great help and advice on my research work. I want to thank Dr. Xinghang Zhang and Dr. Haiyan Wang for their great classes on the Fundamentals of Materials Science and Engineering and Thin Film Science and Technology. I also thank Dr. Andreas Holzenburg for the great class on Transmission Electron Microscopy as well as Scanning Electron Microscopy. I also appreciate all the great help from the former MIC staff, Dr. Zhiping Luo. He trained me on the TEM facilities and was always ready to help during my experiments.

I want to thank all group members and alumni including Dr. Zhenxing Bi, Dr. Joon-Hwan Lee, Dr. Chen-Fong Tsai, Dr. Michelle Myers, Dr. Ick-Chan Kim, Dr. Sungmee Cho, Dr. Aiping Chen, Tianlin Lu, Yuanyuan Zhu, Qing Su, Fauzia Khatkhatay, Liang Jiao, Wenrui Zhang, Jie Jian, Tommy Lynch and Clement Jacob.

They are all great researchers to work with and broadened my view. They are all great persons to hang out and make my life joyful at TAMU.

Last, thanks to my family, particularly, my parents and parents-in-law for their financial support and encouragement, and, to my wife, Qing Chang, for her support, love and our son George Chang Chen.

NOMENCLATURE

PLD	Pulsed Laser Deposition
PVD	Physical Vapor Deposition
TEM	Transmission Electron Microscopy
XRD	X-ray Diffraction
FWHM	Full Width at Half Maximum
SAED	Selected Area Electron Diffraction
FFT	Fast Fourier Transformation
SEM	Scanning Electron Microscopy
STEM	Scanning Transmission Electron Microscopy
VSM	Vibrating Sample Magnetometer
ZFC	Zero Field Cooling
FC	Field Cooling
PPMS	Physical Property Measurement System
PIT	Powder-In-Tube
RABiTS	Rolling-Assisted-Biaxially-Textured-Substrates
IBAD	Ion-Beam-Assisted Deposition
R	Resistance
ρ	Resistivity
T_c	Critical Transition Temperature
K	Kelvin

^{o}C	degrees Centigrade
J_c	Critical Current Density
J_c^{sf}	Self-Field Critical Current Density
$J_c^{in\text{-}field}$	In-Field Critical Current Density
H_{c2}	Upper Critical Field
H_{irr}	Irreversible Field
AFM	Antiferromagnetic
VAN	Vertically Aligned Nanocomposite
SMES	Superconducting Magnetic Energy Storage

TABLE OF CONTENTS

Page

LIST OF FIGURES

Page

LIST OF TABLES

Page

CHAPTER I

INTRODUCTION

1.1 Overview

In the first section of the introduction we summarize the brief history and applications of the superconductors. Several types of superconductors with layer structures are listed. Later on different types of iron based superconductors are compared and we focus on the structure and properties of the '11'-type iron chalcogenide superconductors. In the second section we review the recent progress on the bulk form $FeSe_{1-x}Te_x$ in the respects of synthesis, doping effect, pressure effect and the structure dependence of the superconducting properties. In the third section we compare the $FeSe_{1-x}Te_x$ (x = 0, 0.5 and 1) thin films with their bulk counterparts and illustrate the thin film growth conditions critical for the superconductivity including the substrate effect, thickness dependence, oxygen effect and composition variation. In addition $FeSe_{0.5}Te_{0.5}$ coated conductors on the ion-beam-assisted deposition (IBAD) MgO substrates, rolled textured metal substrates (RABiTS) and even amorphous substrates promising for practical application are discussed in this section.

1.1.1 Background

A superconductor is a material which has two characteristic properties including perfect conductivity (zero resistance) and perfect diamagnetism (Messiner effect), when it is cooled down below a critical transition temperature (T_c) [1]. Superconductivity was first discovered in mercury by Kamerlingh Onnes in 1911 and later found in a variety of materials, including simple elements (e.g., lead and mercury), metallic alloys (e.g., lead-

bismuth alloy), heavily-doped semiconductors (e.g., heavily boron-doped silicon carbide), ceramic compounds with layered structure (e.g., copper oxides) and even certain organic molecules [2]. One of the characteristics of superconductivity is that the electrical resistance of a material sharply drops to zero below certain low temperature. The characteristic transition temperature is known as critical transition temperature, T_c. In addition, a superconductor demonstrates perfect diamagnetism which completely expels the weak magnetic field in superconducting state. This phenomenon is called the Meissner effect [3]. Both zero resistance and Messiner effect are illustrated in Figure 1. 1 [4].

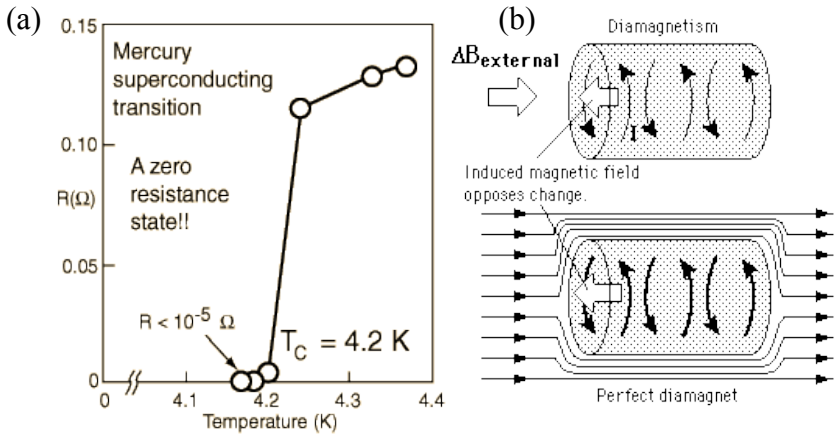

Figure 1. 1 Schematic illustrations of (a) zero resistance in mercury and (b) the Meissner effect. [4]

Superconductors exhibit superconducting properties only below the critical transition temperature T_c and the critical magnetic field H_c as illustrate in the Figure 1. 2.

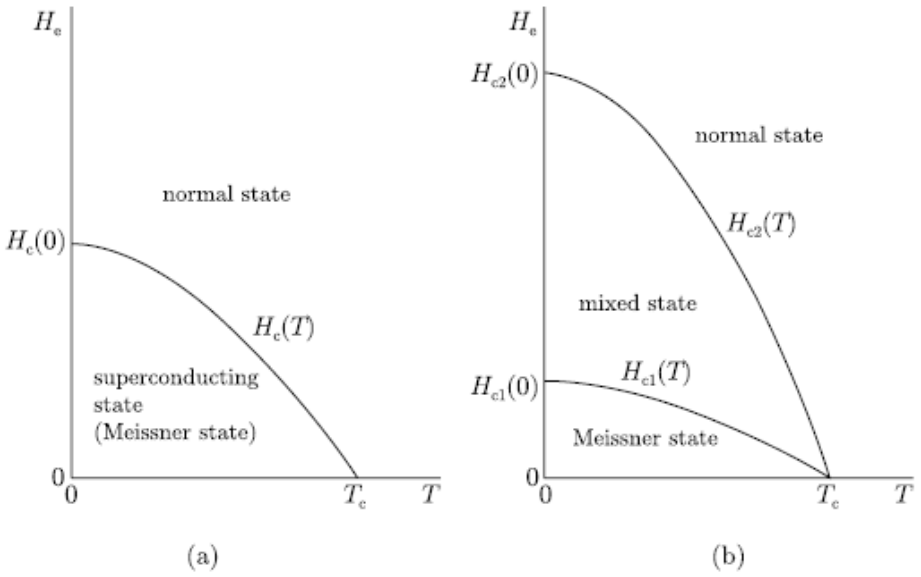

Figure 1. 2 Phase diagram of the field and temperature dependence of type I (a) and type II (b) superconductor. [4]

Depending on the response to the applied magnetic field, two types of superconductors can be categorized, namely, conventional "type I" superconductors and newly discovered unconventional "type II" superconductors. As early as in 1950, Landau-Ginzburg theory predicted the existence of type I and type II superconductors. In this theory, a type-I superconductor had positive free energy of the superconductor-normal metal boundary and the type II has negative energy.

In type-I superconductors, superconductivity is abruptly destroyed via a first order phase transition when the strength of the applied field rises above a critical field value H_c. When a type I superconductor is cooled below critical transition temperature T_c under a weak applied magnetic field, all of the magnetic flux lines are expelled from its interior by generating circulated super-current inside the material. The magnetization (M) is equal to the applied magnetic field with opposite direction when the applied magnetic

field H_e is below the critical field H_c (the maximum field a type I superconductor can sustain without breaking the superconducting state):

$$M = -H_e \ (M < H_c) \text{ (Equation 1. 1)}$$

When the intensity of the applied magnetic field is stronger than the critical field the superconductor will transit from superconducting state to normal state with a sharp drop of the magnetization to $M = 0$. The magnetization curve of type-I superconductors are depicted in Figure 1. 3 (a). This type of superconductivity is normally exhibited by pure metals, e.g. aluminum, lead, and mercury.

Furthermore, the following empirical equation describes the temperature dependence of critical field of type I superconductors:

$$H_c(T) = H_c(0)\left[1 - \left(\frac{T}{T_c}\right)^2\right] \text{ (Equation 1. 2)}$$

Type I superconductors are usually pure elements and alloys which exhibit superconductivity at very low temperature and can be explain by the BCS theory (conventional superconductivity theory). It was predicted by the BCS theory that the critical transition temperature of superconductors can not go beyond about 30 K [5].

Type-II superconductors are characterized by the formation of magnetic vortices under applied magnetic field. This occurs above certain critical field strength H_{c1}. The vortex density increases with increasing field strength. At a higher critical field H_{c2}, superconductivity is completely destroyed. It means there are two critical fields, between which it allows partial penetration of the magnetic field. The first, lower critical field occurs when magnetic flux vortices penetrate the material but the material remains superconducting outside of these microscopic vortices. The vortices

will align in a triangular shape pattern such as shown in Figure 1. 4 to minimize the energy. When the vortex density becomes too large or to say the field strength becomes larger than the critical value, the entire material becomes non-superconducting; this corresponds to the second, higher critical field. The phase diagrams of type I and type II superconductors on temperature-magnetic field plane are shown in Figure 1. 3 (a) and Figure 1. 3 (b). [4]

At the time when the Landau-Ginzburg theory predicted two types of superconductor, all the superconductors discovered were type I and the type II ones were considered not practical. Soon after that type-II superconducting behavior was first observed in experiments when superconducting alloys were investigated under a magnetic field. Most of the type II superconductors are alloys and perovskite ceramics with much higher T_c, J_c and H_c than the type I superconductors. In a type II superconductor, Messiner state, mixed state (vortex state) and normal state on the magnetization curve can be identified as illustrated in Figure 1. 3 (b).

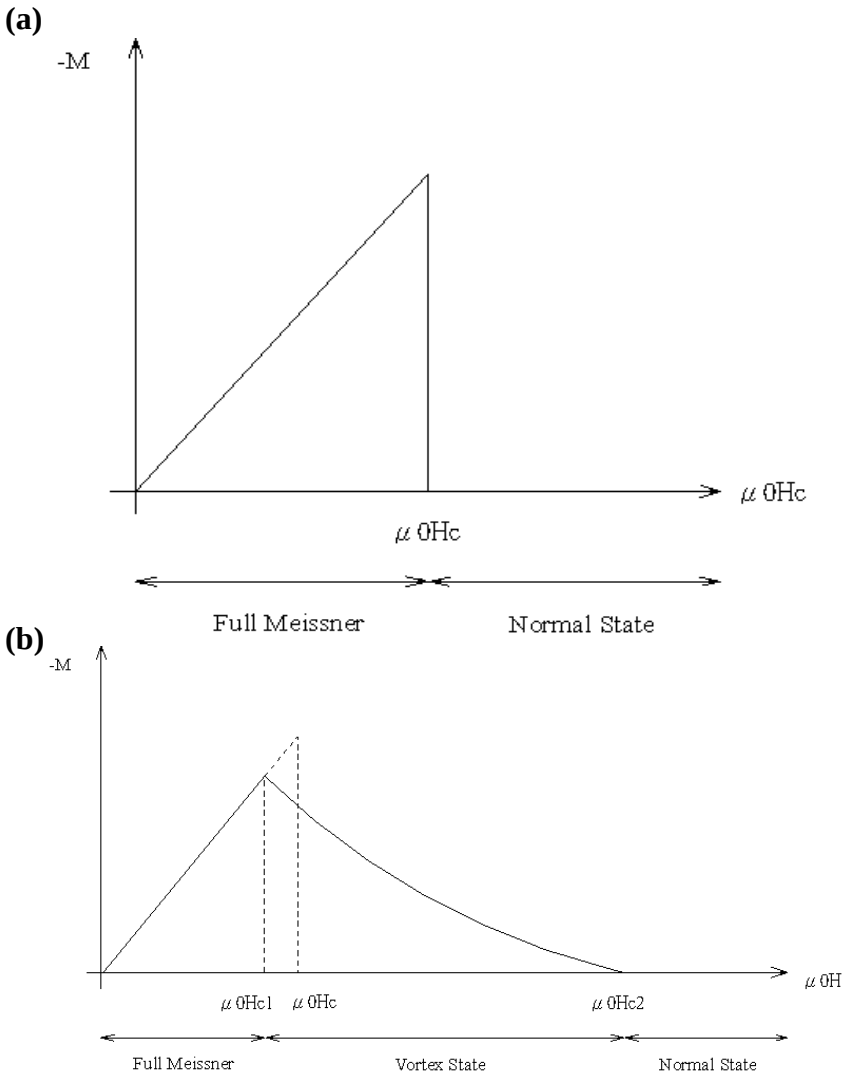

Figure 1. 3 Magnetization curve of type I (a) and type II (b) superconductor. [4]

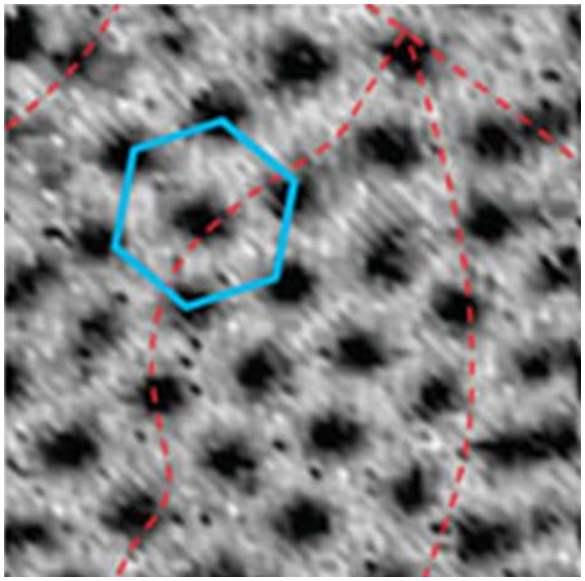

Figure 1. 4 STM imaging of the triangular vortex lattice in $NbSe_2$. [6]

The high T_c and superconducting behavior in type II superconductors cannot be explained by the conventional BCS theory. It is believed that the superconducting properties in type II superconductors relate to layer lattice structure. Examples of type II superconductors are nickel-based superconductors, cuprate as well as the iron-based superconductors. In 1986 Bednorz and Muller [7] discovered the La_2CuO_4 with a critical transition temperature of 35 K when certain amount of La^{3+} substituted by Ba^{2+}, which is one of the most important discoveries in modern condensed matter physics. One year later it was found replacing the lanthanum with yttrium (i.e., $YBa_2Cu_3O_{7-x}$) pushed the critical temperature to 92 K, which is higher than the boiling point of liquid nitrogen at 77 K at atmospheric pressure [8]. It started the research of exploration of the high temperature superconductors.

1.1.2 The Applications of Superconductivity

The application of superconductors is one of the most important reasons why so many studies were carried out on superconductor. The applications of superconductors are mainly based on its characteristics of zero resistance and Meissner effect.

The discovery and application of superconductors were highly dependent on the cryogenic technology of liquefication of the helium. The main cost to operate the superconducting equipment is for cryogens, and we prefer to use cheaper cryogens such as liquid H_2 and liquid N_2 instead of pricy and scarce liquid He which is the reason for pushing the T_c and looking for new superconductors. Another limitation is the critical current density J_c.

The superconductor cables made of the traditional high temperature cuprates superconductors such as $YBa_2Cu_3O_{7-x}$ (YBCO) and $Bi_2Sr_2Ca_2Cu_3O_{10+x}$ (BSCCO) were used to transport electricity. In conventional metal such as copper and aluminum transmission lines, about 10 ~ 15% of electricity is dissipated as heat due to the resistive loss. By replacing conventional metal transmission lines with superconductor transmission lines, the resistive loss can be prevented. Furthermore, with much larger current density in the superconducting cables, more than 7000% space-efficiency can be achieved.

In addition, superconducting magnet is another important application. Once the current is injected into the superconducting coil to generate strong magnetic field, the power supply can be switch off; and the current and magnetic field stays as long as $T < T_c$ and $H < H_c$.

Another application based on the strong magnetic field generated by superconductor coils is in the levitation system. The levitation train can travel at a quite amazing speed because it is levitated to avoid the frictional resistance. Superconducting coils can also be used to make motors and generators which will save 90% of the size and weight comparing to conventional devices. In addition in the medical equipment MRI the Superconductor magnet is also used to generate magnetic field of around 1.5 T. The MRI has spatial resolution to trace atomic nuclei.

Another large scale application of superconductor is the superconducting magnetic energy storage system which can improve the stability of power grids. In the year of 2000, American Superconductor installed a superconducting magnetic energy storage system (SMES) in Wisconsin. Each SMES units can reserve over 3 million watts to stabilize line voltage during a disturbance in the power grid. Figure 1. 5 (a)-(c) show the pictures of HTS cable, super-power grid and SMES, respectively.

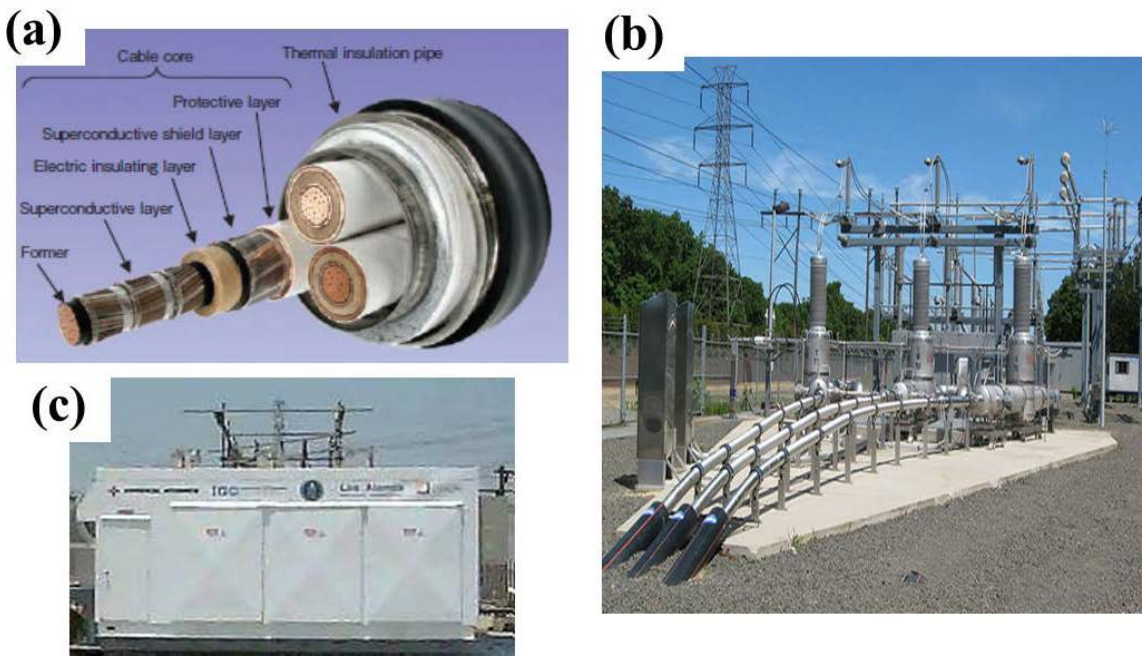

Figure 1. 5 (a) HTS power transmission cable, (b) superconducting power grid in Albany, New York, and (c) SMES. [9]

The newly discovered iron-based superconductor has relative low critical transition temperature, however the upper critical field is much higher than the high temperature superconductor such as cuprates and it is in favor of the superconducting energy storage system in which the stored energy is proportional to B^2. In addition the superconducting properties are weakly anisotropic which makes it especially useful for magnets applications.

1.1.3 Layered Structure in Superconductors

Layered structure is a common feature of the superconductor especially in the type II superconductors; here we listed several typical type II superconductors with different layer structures.

Cuprates

In 1986 Bednorz and Muller [7] discovered the La_2CuO_4 with a critical transition temperature of 35 K when certain amount of La^{3+} substituted by Ba^{2+}. One year later it was found that, replacing the lanthanum with yttrium (i.e., making YBCO) pushed the critical temperature to 92 K [8]. The structure of these materials strongly depends on the oxygen content. Optimum superconducting properties occur when $x \sim 0.07$, i.e., almost all of the O(1) sites are occupied, with few vacancies with the orthorhombic structure.

MgB_2

MgB_2 is actually an 'old' material, known since the early 1950s. But only recently it was discovered to be a superconductor (Akimitsu 2001, Nagamatsu *et al.* 2001) at a remarkably high critical temperature—about 40 K—for its simple hexagonal structure. MgB_2 possesses the simple hexagonal AlB_2-type structure (space group *P6/mmm*), which is common among borides. It has boron layers which are separated by hexagonal close-packed layers of magnesium. The magnesium atoms occupy the center of hexagons formed by borons and donate their electrons to the boron planes. MgB_2 exhibits a strong anisotropy in the B–B lengths: the distance between the boron planes is significantly longer than the in-plane B–B distance [10].

Nitride-based superconductors

This type of materials is similar to the metal-doped fullerenes, which show relatively high transition temperatures, the electron donor atoms sit in the interstitial sites between the adjacent fullerene balls.

A group from Hiroshima University reported b-ZrNCl, consisting of Zr–N double layers sandwiched between two close-packed chlorine layers. With lithium intercalation, the crystal changed from a semiconductor to a metal, and became a superconductor at 13 K [11].

Besides that, they reported the properties of the isostructural compound b-HfNCl. After electron-doping through lithium intercalation, they observed superconductivity with a T_c up to 25.5 K [12]. This transition temperature is higher than that observed in any intermetallic compound, which suggests transition temperatures of the layered nitride structures may be comparable to the layered copper oxide structures.

WO_3 superconductors

This topic is not quite new and it started ever since 1979 to calculate the property of alkali doped WO_3 [13]. Due to the localized surface superconductivity, superconductivity of WO_3 was only demonstrated using Magnetization M-T [14, 15]. WO_3 crystals were doped with Na on the surface to around 7 % nominal atomic concentration. Scanning tunneling microscopy and magnetization measurements were employed in the study of these crystals. Around 10% of the surface was covered by superconducting islands with the size of 20–150 nm and the rest is insulating revealed by tunneling experiments.

Magnetization measurements show that the superconducting phase formed at the surface has a critical temperature of 91 K. Most of the sodium is concentrated in these islands and therefore they are metallic in nature, above 30 % in atomic concentration. This material is therefore a non-cuprate superconductor with a high critical temperature [15].

Study shows the superconducting Cs-doped WO_3 Crystal Surface has a $T_c \sim 5.9$ K and the property is also limited in the surface area similar to the Na-doped WO_3 in the surface island [14].

1.1.4 From Cuprates to Iron-based Superconductors

For more than 20 years, the high temperature superconductors with T_c higher than the predicted BCS limit 30 K [5] have been mostly cuprates. The recent discovery of the iron-based superconductors has generated enormous interest because these materials are the first non-copper oxide superconductors with T_c exceeding 50 K [16-19]. The first reported iron-based superconductor is LaOFeP, discovered by Hideo Hosono in May 2006 [20]. However, it didn't catch much attention due to its low superconducting transition temperature, $T_c \sim 4$K. Two years later, in February 2008, Hideo Hosono's group reported the discovery of another iron-based superconductor, fluorine-doped LaOFeAs with a high T_c of 26 K [21]. In LaOFeAs electron carriers generated by F-doping into oxygen sites are injected into FeAs metallic layers as a result of the large energy offset between these two layers. The carrier doping layer is separated by the conduction layer. T_c=43K at 4GPa was obtained in this F-doped LaOFeAs [22]. Soon after that, four main types of iron-based superconductors with the tetragonal

structure indicated in Figure 1. 6 have been reported: '1111'-type *Re*FeAsO *(Re* = rare earths) [23], '111'-type *A*FeAs *(A* = alkali metal) [24], 122-type $AeFe_2As_2$ *(Ae* = alkaline earths) [19], and '11'-type Fe*X (X* = chalcogens) [25]. In this thesis we focus on the '11'-type FeX *(X* = chalcogens). In 122-type $AeFe_2As_2$ superconductor, by hole doping potassium (K) in $BaFe_2As_2$ it gets a T_c =38K [19]. In '111'-type LiFeAs becomes superconducting apparently without external doping [26]. The superconducting properties of '11'-type FeSe can be enhanced by covalently doping with Te and S [27] or by applying external pressure [28]. The common feature of the high temperature superconductors is the layered structures. Superconductivity in the cuprates occurs by doping a Mott antiferromagnetic (AFM) insulator, whereas iron-based superconductors become superconducting by doping a parent AFM semi-metal. In both cases superconductivity competes with the AFM states. Compared with conventional superconductors, both iron-based superconductors and the cuprates have high normal-state resistivities, low carrier densities and low Fermi energies. As a result, both iron-based superconductors and the cuprates have small Cooper pairs with $\xi \approx 1–2$ nm compared to classic superconductors such as niobium (where $\xi \approx 40$ nm)and large ratios $\gamma = m_c/m_{ab}$ of the electron masses along the *c* axis (m_c) and the *ab* plane (m_{ab}), with γ ranging from ~1 to ~50 for iron-based superconductors and from ~20 to $>10^4–10^5$ for the cuprates [29].

In Table 1. 1 four main categories of iron-based superconductors are summarized with some examples.

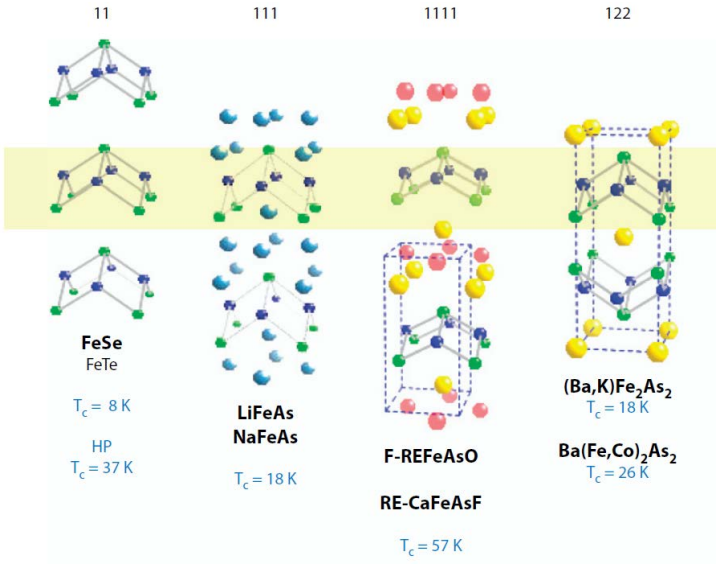

Figure 1. 6 Four different structures of the FeAs-based materials, which contain the FeAs planes (highlighted in yellow). Abbreviation: RE, rare earth.[30]

Table 1. 1 Critical transition temperatures for the iron-based superconductors. (Abbreviations: RE, rare earth; AE, alkaline earth; TM, (3d–5d) transition metals; HP, high pressure.)

Families	Formula	T_c [Reference]
'11'	FeSe	8 K [25]
	FeSe(HP)	36.7 K [31]
'111'	LiFeAs	18 K [32]
	NaFeAs	13 K [26]
'1111'	Electron doping: $REFeAsO_{1-x}F_x$	55–56 K[19]
	Hole doping: $RE_{1-x}AE_xFeAsO$	25 K [33]
'122'	$AE_{1-x}AL_xFe_2As_2$	38 K [19]
	$AE(Fe_{1-x}TM_x)_2As_2$	20–28 K [34]
	$AEFe_2As_{2-x}P_x$	30 K [35]

Before FeSe was reported as a superconductor, FeSe thin film was studied for solar cells in the semiconductor industry [36]. After the discovery of FeSe as

superconductor, its superconducting properties were studied in comparison with the iron pnictide superconductor.

The common feature of newly discovered iron-based superconductor is the layer-by-layer tetragonal structure with a = b < c. In the iron pnictide superconductor by doping the system with electron or hole doping as well as rare earth element intercalation into the layered structure, the superconducting transition temperature can be increased. Although its transition temperature is not as high as that of pnictide, the iron chalcogenide has some advantages. First it has a binary composition, so the stoichiometry control is relatively easy. Second it does not contain the toxic arsenic element. In addition it has a simple structure which makes the study on the similarity and difference to the cuprates easy. It is also easier to study the superconducting mechanism such as modeling and theoretical calculation. The pressure effect was also found in this '11' system, for example, the superconducting transition temperature can be pushed to as high as 37 K under 4 GPa pressure which is very similar to the pnictide system [37]. The study on the structure variation under pressure and the effect on the superconducting properties will be more straightforward. This system can be also doped with covalent doping to generate chemical pressure to enhance the superconducting properties.

In this part the bulk '11'-type iron-based superconductors are reviewed from synthesis method, composition variation study to the pressure effect, and the structure change with doping and under pressure such as the ion height and angle change to find clues to further improve the superconducting properties of this '11' system.

The first iron chalcogenide superconductor FeSe with a transition temperature T_c around 8 K was discovered in July 2008 [25]. The corresponding superconducting properties measurements are shown in Figure 1. 7 including the R-T (resistivity vs. temperature) measurement, M-H (magnetic momentum vs. magnetic field) hysteresis loop and upper critical field (H_{c2}) measurement. Iron chalcogenide are also of great interest for the high-field applications. In general the superconducting transition temperatures of iron chalcogenides are lower than iron pnictides, however they exhibit lower anisotropies and very high upper critical field.

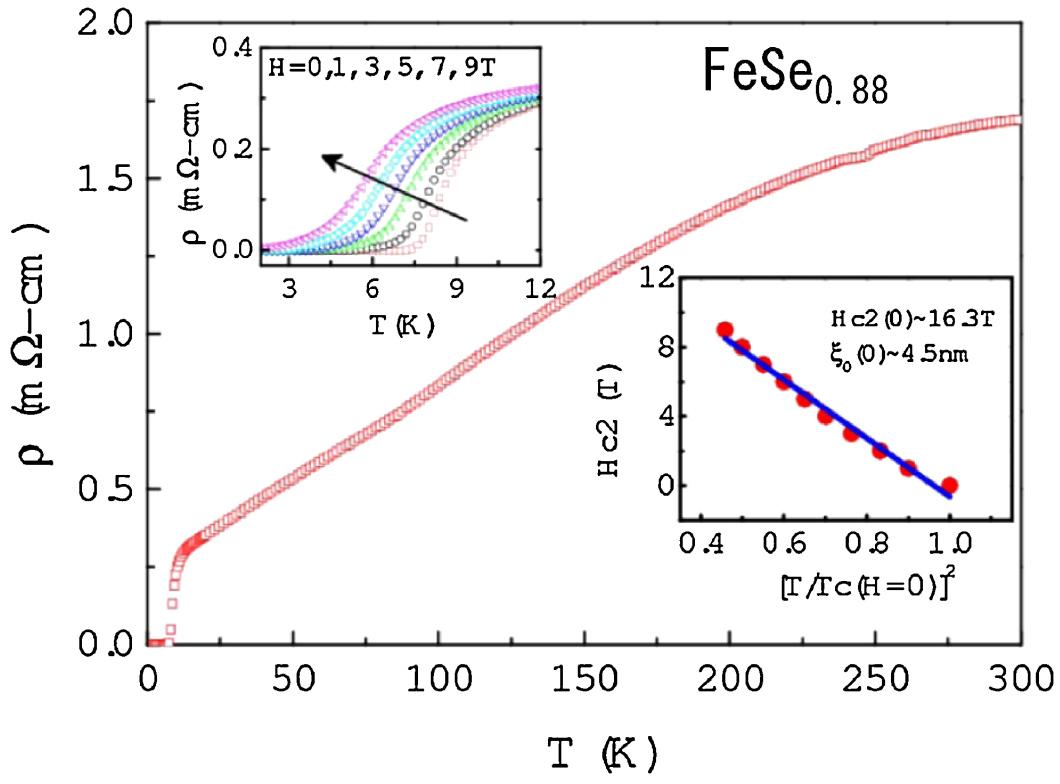

Figure 1. 7 Temperature dependence of resistivity for $FeSe_{0.88}$. The insets display the temperature dependence of resistivity under magnetic fields and the estimation of the H_{c2}.[25]

The superconducting FeSe has a tetragonal PbO structure (P4/nmm space group) containing Fe-Se planar sub-lattice with an interval of 5.518 Å as show in Figure 1. 8. This layered structure is equivalent to the layered FeAs structure in previously found iron pnictide superconductors. These common features to the FeAs-based superconductors have made iron chalcogenide a key system to elucidate the mechanism of superconductivity in iron-based superconductor. FeSe also provides a simple system to study the iron-based superconductors in comparison with cuprates [38]. The material contains identical Fe-Se layers similar to the layered structure in cuprates which is believed to be responsible for the superconductivity [39].

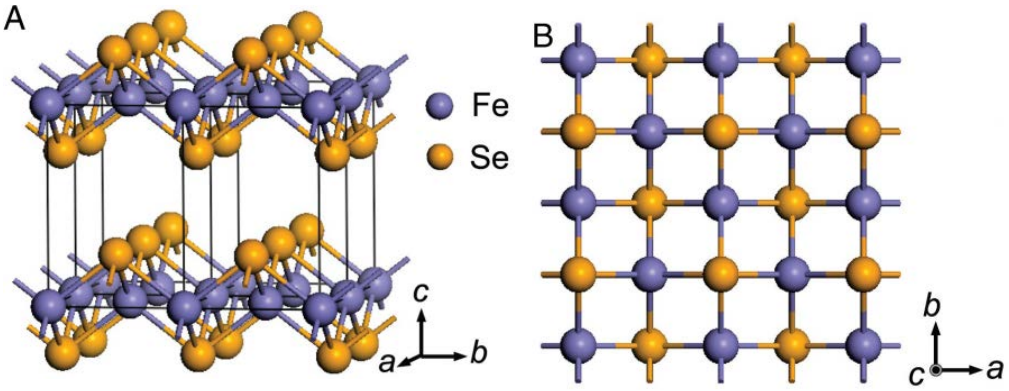

Figure 1. 8 Schematic crystal structure of α-FeSe (Four unit cells).[25]

Since then, the effects of stoichiometry [40-42], structure variation [31, 43, 44], strain and stress [45], pressure [28, 31, 46] and doping [27, 47] on the superconducting properties of FeSe have been explored. Following the similar research approaches of the iron pnictide superconductors, high external pressure [28, 46, 48], the covalent doping of

the other chalcogens [41], the transition metals [49, 50] and the alkali metals [51, 52], were applied to enhance the superconducting properties.

Besides bulk FeSe that has been explored extensively [25, 27, 43, 46, 53], epitaxial FeSe thin films have recently attracted great research interests [45, 54, 55]. Most of the FeSe films reported were deposited by pulsed laser deposition (PLD). Compared with its bulk counterpart, FeSe thin film has a great potential in developing the ordered quasi-2D structure and is suitable for coating technology which has already been applied in $YBa_2Cu_3O_{7-x}$ coated conductors [56]. In previous FeSe thin film work, it was reported that the film thickness and orientation [54], film stoichiometry and deposition temperature are critical factors for the superconducting properties [42, 55, 57] of FeSe thin film. Wang *et al.* reported that the optimum deposition temperature for FeSe films on MgO is 500°C. The T_c^{onset} and T_c^{zero} are 10 K and 4K, respectively for the film with thickness of 140 nm. However the film is not in the *c*-axis orientation [54]. Nie *et al.* reported that the optimum deposition temperature of FeSe films with *c*-axis orientation on different substrates is 380°C. The T_c^{onset} of the films is lower than 10 K on $SrTiO_3$ (STO) (001) and MgO (001). The upper critical field H_{c2} of the film was estimated to be 35 T with linear extrapolation method. It was also reported that the tensile strain in *a*-*b* plane suppresses the superconductivity [45]. Han *et al.* reported single-phased, *c*-axis oriented epitaxial $FeSe_{0.88}$ films on STO (001), (La, Sr)(Al, Ta)O_3 (001) and $LaAlO_3$ (001) with the T_c^{onset} of 11.8 K and the T_c^{zero} of 3.4 K [55].

Although the critical transition temperature (T_c) of the iron-based superconductor is much lower than that of the cuprates, the iron-based superconductor has lower

anisotropy which is good for magnets applications [29]. Besides the superconducting transition temperature, critical current density (J_c) is another important factor for future applications. Although compared to the cuprates or even the iron pnictides, the J_c of the iron chalcogenide superconductor is lower; its slow decrease of the J_c with increasing magnetic field as well as its easy composition control makes the iron chalcogenide a promising candidate for high field applications [58, 59].

In the isovalent-doped FeSe, either tellurium or sulfur was used, which is similar to the effect of external pressure to induce structure distortion to the ground state of the superconductivity [60]. The effect of doping concentration was also studied for achieving optimum stoichiometry in iron chalcogenide systems such as $FeSe_{1-x}Te_x$ and $FeTe_{1-x}S_x$ [41, 61, 62]. T_c up to 21 K in the epitaxial $FeSe_{0.5}Te_{0.5}$ thin films was reported [63]. In bulk form, the critical current density of the single crystal $FeSe_{0.4}Te_{0.6}$ was reported to be around 10^5 A/cm^2 at 2 K [58, 59, 64, 65]. Recently enhancing the critical current of the iron chalcogenide thin films has attracted great research interests [66, 67].

1.2 Iron Chalcogenide in Bulk Form

1.2.1 Synthesis of the Iron Chalcogenide

The iron chalcogenide can be synthesized with multiple methods. The bulk materials have already been synthesized by several groups. The process can also been applied to prepare target for PLD deposition. In this part we will illustrate the solid state reaction with the raw elements of Fe and Se to synthesize the tetragonal phase superconducting FeSe.

Due to the intrinsically Se deficient nature of the superconducting FeSe, the superconductivity in tetragonal FeSe is very sensitive to stoichiometry and disorder. In addition the FeSe is also sensitive to the oxygen and moisture. McQueen *et al.* [40] reported a reproducible thermal process for fabrication of bulk samples. In their method samples were prepared from freshly high purity iron pieces and selenium shots with slightly Fe rich ($Fe_{1.06}Se$), and were sealed in vacuum silica tubes with a piece of cleaned carbon to prevent the oxidation of the FeSe. The tube was sealed by another Si ampoule and placed in the furnace with temperature of 750 °C and then increased to 1075°C for 3 days, followed by a fast cooling down to 420 °C and held for 2 days before quenched in -13 °C brine for reproducible result. The quench was required to keep the high temperature tetragonal phase according to the phase diagram in Figure 1. 9.

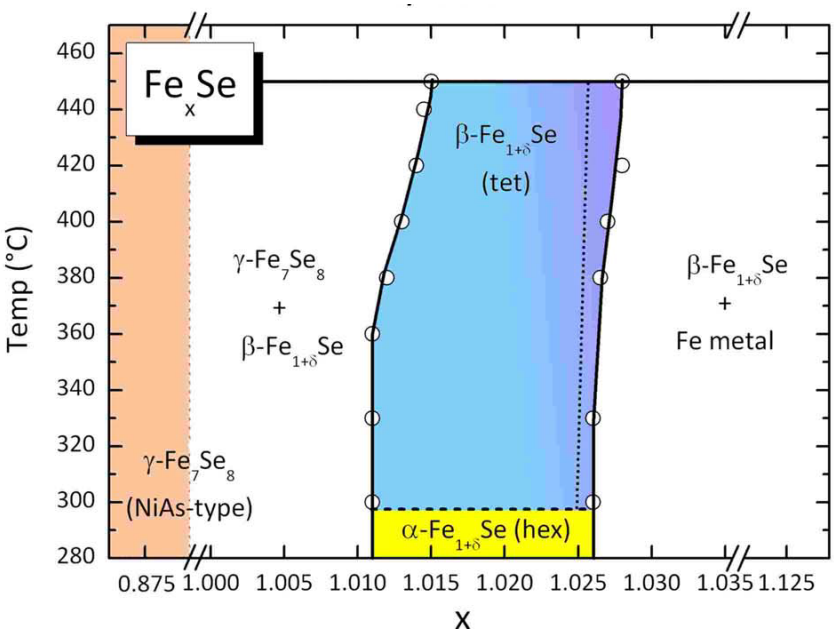

Figure 1. 9 Phase diagram of FeSe. Below 300 °C, tetragonal $Fe_{1+\delta}Se$ slowly converts to hexagonal Fe_xSe with NiAs structure without superconducting properties above 1.8 K.

In addition FeSe can also be synthesized by the diffusion method reported by Gao *et al.*. In this method, proper amounts of Se powder and pure iron wires and tapes (4–6 cm pieces) after cleaning were sealed into an iron tube as raw materials. Then the temperature was raised between 400 and 800 °C for 8 to 12 h for the reaction between these wires and tapes with Se vapor. The final products were wires and tapes covered with FeSe layer from several microns to about 0.1 mm thick, depending on the process and the amount of Se powder. The FeSe layer can be easily peeled off from the wires and tapes.

For the single crystals growth, a technique of convective solution transport using KCl as solvent at 840-790 °C is developed using a vertical tubular wire wound furnace with high temperature bottom zone and a gradually reducing upward gradient [68]. This furnace helps the dissolution of FeSe in KCl at the bottom portion of the crucible and the FeSe can be transported upward by convection and crystallized in the top portion of the solution at low temperature. By controlling the temperature and cooling process, big crystals can be obtained in a relatively short period.

The covalent doped iron chalcogenide can also be made by solid state reaction. Sales *et al.* reported the Bridgeman method to prepare $Fe_{1+y}Te_xSe_{1+x}$ [69]. In this method stoichiometry mixture of Fe pieces (99.99 wt. %), Te shot (99.9999 wt. %), and Se shot (99.9999 wt. %) were sealed in vacuum silica Bridgeman ampoule. The elements were kept melt together at 1070 °C for 36 h and then cooled down to 350–750 °C at rate from 3 to 6 °C/h, followed by furnace cooling. Typically over half of the resulting boule was single crystal which could be easily cleaved perpendicular to the *c* axis.

1.2.2 Doping Effect

Depending on the elemental composition, synthesis process including temperature and pressure iron chalcogenides can form several types of crystal structures. Up to now, three PbO-type binary chalcogenide compounds, FeS, FeSe, and FeTe [25, 55, 70] have been reported. FeTe is the most stable phase among them, and the single phase can be synthesized by a solid-state reaction method [71]. With decreasing radius of chalcogens ions, the tetragonal structure tends to be unstable.

The binary iron chalcogenide can also be doped with the other chalcogens. The highest T_c appears in $FeTe_{1-x}Se_x$ with x close to 0.5, which has the tetragonal structure without structure transition from tetragonal structure to the orthorhombic at low temperatures compared to the Se-rich phase ($0.5 \leq x \leq 1$). However, pure FeTe with transition from tetragonal structure to monoclinic structure along with the appearance of long-range antiferromagnetic (AFM) ordering at low temperature, does not show superconductivity. However a theoretical calculation suggested the higher stability of magnetism and a higher T_c for tetragonal FeTe than that of FeSe and FeS [60].

$Fe_{1-\delta}Te_{1-x}Se_x$

The end members FeSe and FeTe have quite different physical properties. Figure 1. 10 shows the resistivity vs. temperature measurement of FeSe and FeTe. FeSe shows monotonic decreasing of resistivity and undergoes a superconducting transition at T_c^{onset} around 13 K. In contrast, FeTe shows AFM ordering around 70K where the resistivity anomaly appears and with superconducting transition. [27, 72, 73]

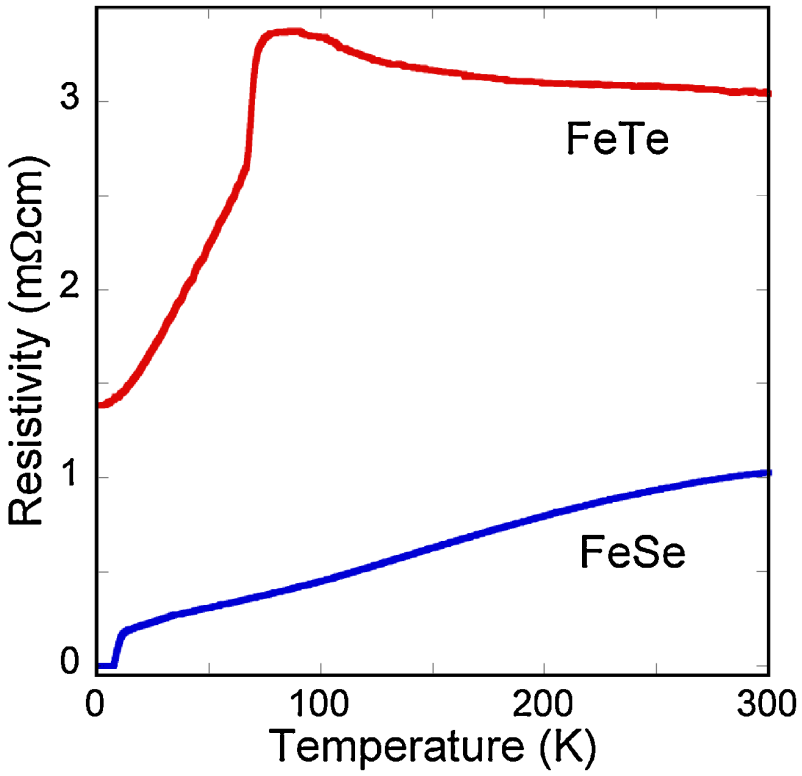

Figure 1. 10 Temperature dependence of resistivity of FeSe and FeTe. FeSe shows metallic behavior with superconducting transition at low temperature. In contrast, FeTe exhibits AFM ordering around 70K without superconductivity.

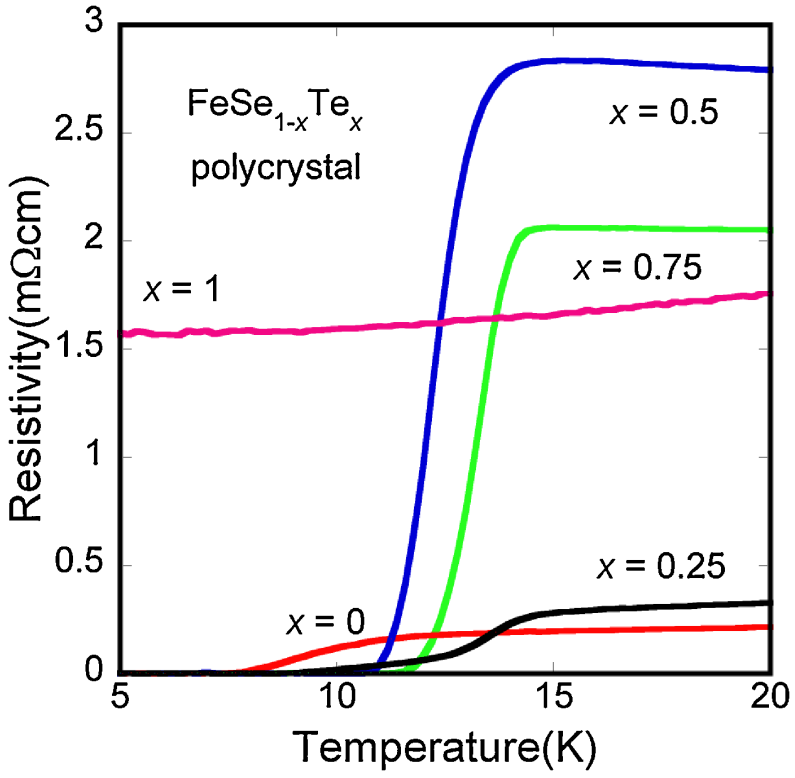

Figure 1. 11 Temperature dependence of resistivity for $FeTe_{1-x}Se_x$ as a function of composition.

Different compositions were tested for the $Fe_{1-\delta}Te_{1-x}Se_x$ system to establish a phase diagram. Figure 1. 11 shows the temperature dependence of resistivity for $FeTe_{1-x}Se_x$. [27] The broad superconducting transitions imply the coexistence of FeSe and FeTe corresponding to the mixed region (A+B) in the composition dependence of lattice constants of a and c plotted at around x = 0.7-0.95 in Figure 1. 12 [27, 72, 73]. The FeSe undergoes a structure transition from tetragonal to orthorhombic structure, and the structural transition is suppressed when doped with Te. Close to x = 0.5 in the $FeTe_{1-x}Se_x$ system, the structure transition disappears. With further Te doping, the system exhibits AFM order from short range to long range [74].

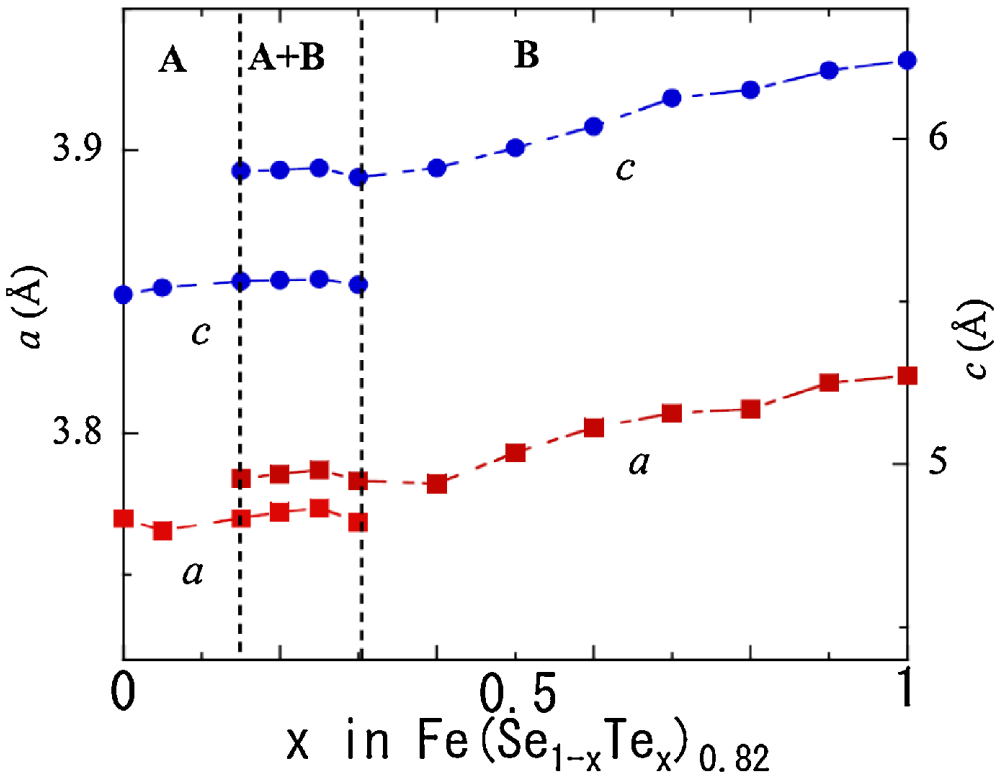

Figure 1. 12 Composition dependence of lattice constants a and c. The miscible region exists with x = 0.05 - 0.3 in $Fe(Se_{1-x}Te_x)_{0.82}$. [72]

According to the magnetization of zero-field cooling (ZFC) and field cooling (FC) for the single crystals $Fe_{1+\delta}Te_{1-x}Se_x$, the phase diagram of $Fe_{1+\delta}Te_{1-x}Se_x$ was established as shown in Figure 1. 13. The tetragonal to orthorhombic structure transition observed in FeSe is suppressed with by Te doping. The highest T_c appears at the tetragonal phase close to x = 0.5. With further increase of Te concentration, the T_c decreases along with the AFM ordering as well as the tetragonal to monoclinic structure transition, and the superconductivity disappears.

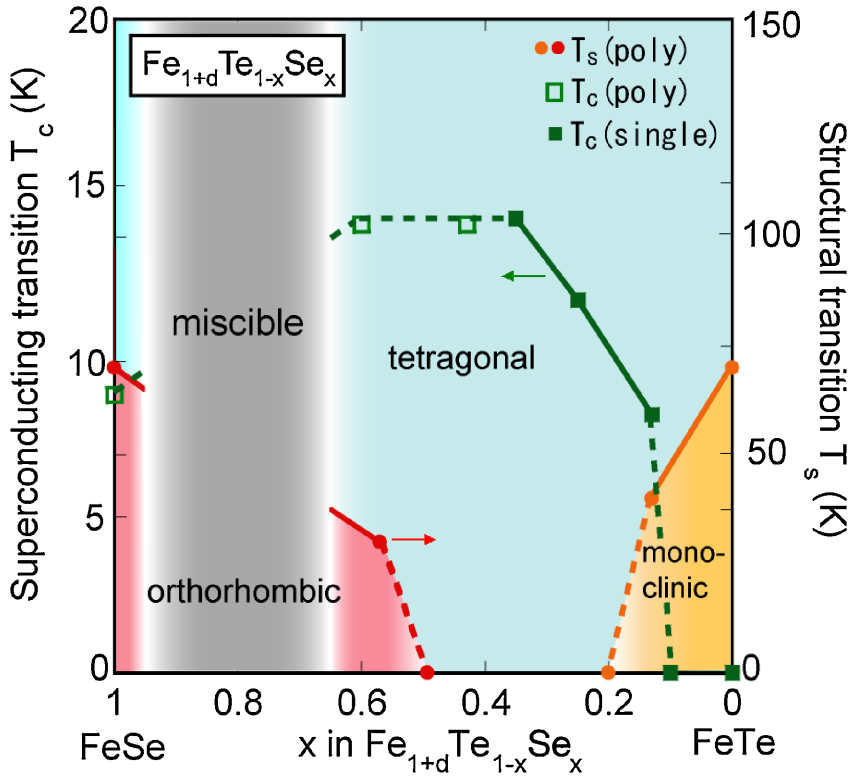

Figure 1. 13 Phase diagram of $Fe_{1-\delta}Te_{1-x}Se_x$.

Besides T_c, the critical current density is another important parameter to evaluate the superconductor for practical applications. Yadav *et al.* reported transport and magnetic studies on high-quality $FeTe_{0.60}Se_{0.40}$ single crystals to determine the critical current density (J_c) as shown in Figure 1. 14. They calculated J_c from the magnetic hysteresis loop up to 12 T at various temperatures using the Bean model and the magnetic hysteresis loop shows a fishtail shape which indicates the weak or non-superconducting phases. Low anisotropic in the '*ab*' and '*c*' directions and very high upper critical field were found in this system. [59]

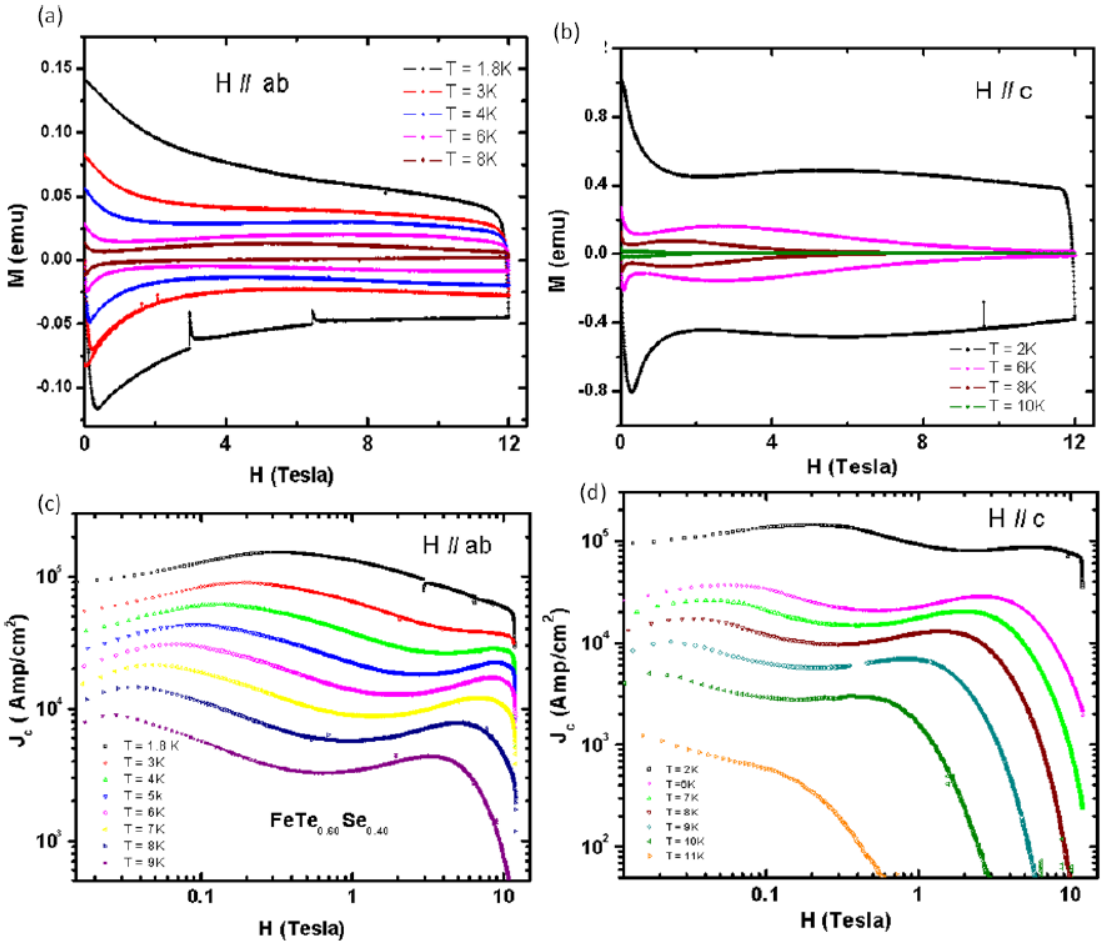

Figure 1. 14 The magnetic hysteresis loop measured up to the 12 T field for (a) the $H \parallel ab$ plane and (b) the $H \parallel c$-axis. The field dependence of the critical current density J_c at different temperatures is plotted on the log-log scale for (c) the $H \parallel ab$-plane and (d) the $H \parallel c$-axis. [59]

$FeTe_{1-x}S_x$

S-substitution for Te suppresses AFM ordering and induces superconductivity in FeTe. [61] The resistivity vs. temperature (R-T) measurement and magnetic susceptibility measurement for nominal $Fe_{1.08}Te$, $FeTe_{0.9}S_{0.1}$, $FeTe_{0.8}S_{0.2}$ indicate superconductivity at $T_c^{onset} \sim 10$ K and the phase diagram of $FeTe_{1-x}S_x$ was built accordingly. In $FeTe_{1-x}Se_x$ the S substitution for Te suppresses AFM ordering in FeTe

and induces superconductivity. Although zero resistivity was observed in the solid-state reacted $FeTe_{1-x}S_x$ samples, the superconducting volume fraction was less than 20% estimated from the susceptibility measurement of $FeTe_{0.8}S_{0.2}$, which indicates the inhomogeneity of the sample or the S was not doped sufficiently. Solid reaction method allows the synthesis of an almost pure iron chalcogenide single phase, however, solid-state reacted $FeTe_{1-x}S_x$ shows only filamentary superconductivity due to the solubility limit of S into the Te site because of the ionic radius difference between S and Te [75].

Moisture can also induce superconductivity in $FeTe_{1-x}S_x$ with a broad onset of the superconducting transition soon after synthesis. In addition, the T_c^{onset} and superconducting volume were dramatically improved by exposing to the air. [76] The T_c^{zero} of $FeTe_{0.8}S_{0.2}$ appeared a few days after and reached 7.2K 110 days later along with enhancement of the superconducting volume fraction to 48.5% according to the susceptibility measurement. Recently, the oxygen annealing at 200 °C was reported to induce superconductivity in $FeTe_{0.8}S_{0.2}$ [77] In addition, the oxygen-annealed $FeTe_{0.8}S_{0.2}$ shows a sharp superconducting transition with high superconducting volume fraction close to 100% and a broad hump was observed around 60K in the R-T plot after oxygen annealing, in $FeTe_{1-x}S_x$.

$FeSe_{1-x}S_x$

The S or Se substitution for Te suppresses the AFM ordering in FeTe and induces superconductivity. However the effect of the S substitution in FeSe was not so obvious. The T_c slightly increases which may be because of the suppression of the

structure transition from tetragonal to orthorhombic in FeSe. [27] However, the T_c is suppressed above x = 0.2, and zero-resistivity state is not achieved in $FeSe_{0.6}S_{0.4}$.

$Fe_{1-x}M_xSe$

Besides the covalent doping, the iron chalcogenides can also be doped with different metals into the iron site with a significant effect on the superconducting properties. Wu *et al.* [78] reported the substitution effect of metals including Al, Ti, V, Cr, Mn, Co, Ni, Cu, Ga, In, Ba and Sm in superconducting tetragonal $FeSe_{1-x}$ with a doping level below 10 at.%. It was reported that iron can be doped by Co up to 50 at.%, and superconductivity disappears for tetragonal $FeSe_{1-x}$ with doping level above 2.5 at.% [79]. However, Mizuguchi *et al.* reported for T_c^{onset} of 10 and 5 K in $Fe_{1-z}Co_zSe_{1-x}$ with *z* equal to 0.05 and 0.1, respectively [27]. Zhang *et al.* [53] reported the lack of superconducting transition down to 2K in $Fe_{0.96}Ni_{0.04}Se_{1-x}$. In contrast, Mizuguchi *et al.* [27] reported T_c^{onset} at 10K in $Fe_{0.95}Ni_{0.05}Se_{1-x}$ without zero resistance showing up. Although the solubility of Cu in the $FeSe_{1-x}$ is up to 20–30 at.%, only $Fe_{1-x}Cu_xSe_{1-x}$ with doping level $x < 0.02$ exhibits superconductivity while those with $x > 0.03$ show semiconductor like properties [49, 78, 80]. Based on the above studies, it is concluded that metal substitution such as Co, Ni and Cu strongly suppresses the superconducting properties of tetragonal $FeSe_{1-x}$. There is only one exception, e.g., Mn substitution increases the T_c at a low doping level of 2 at.% [81] and only slightly changed the T_c value at 30 at.% [49].

$K_xFe_2Se_2$

The anion height which is the distance between the *chalcogens* atoms and the Fe plane in each iron layer is an important parameter affecting the T_c [82]. It can be changed by altering the ratio of Se to Te or by external pressure. T_c^{onset} of FeSe increases to 37K under 4.5 GPa pressure. In addition intercalation of alkaline metal ions, such as K^+ [52], Rb^+ [83] and Cs^+ [84] between the Fe_2Se_2 layer was reported to enhance the T_c above 30 K which is the highest record among the iron chalcogenides under ambient pressure up to now. However this enhancement is associated with a structural change from '11'-type (*P*4/*nmm*) to 122-type (*I*4/*mmm*). Figure 1. 15 shows the crystal structure of $K_xFe_2Se_2$. The c axis parameter is 7.0184Å in comparison with 5.518Å in tetragonal $FeSe_{1-x}$. The Fe–Se bond length also increases by 2.15%.

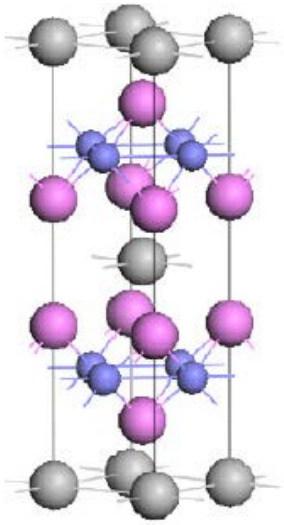

Figure 1. 15 Crystal structure of $K_xFe_2Se_2$ where Fe, Se and K atoms are shown in blue, purple and gray, respectively.

The anion height and Se–Fe–Se bond angles for $K_xFe_2Se_2$ seem to be closer to the optimum values (1.38Å and 109.47°) for iron-based superconductors [82]. The other possible reason for the superconductivity in $K_xFe_2Se_2$ is alkaline ions deficiency which corresponding to the hole doping effect.

1.2.3 Pressure Effects

FeSe

The iron chalcogenide will response to the high ambient pressure, among them FeSe shows the most significant pressure effect. The T_c^{onset} and T_c^{zero} of FeSe bulk at ambient pressure are 13 and 8.5 K, respectively. The T_c^{onset} dramatically increases from 13 K at atmospheric pressure to 27 K at 1.48 GPa as shown in Figure 1. 16. [28]. At the beginning of the pressure effect study piston–cylinder cell was first to be used to apply a hydrostatic pressure up 1.48 GPa. The transition becomes sharper at 0.42 GPa and then get broaden although the T_c^{onset} and T_c^{zero} are both pushed higher. The external pressure can be further increased using a diamond-anvil cell, the T_c^{onset} reaches maximum of 37 K when gradually increase the pressure to 6.6 GPa [31, 37]. Somehow the T_c^{zero} can not be achieved under the high pressure. The T_c of 37 K is only lower than 39 K of MgB_2 and 38 K of Cs_3C_{60} under high pressure among the binary superconductors. [85, 86] An indenter cell was used to precisely measure the pressure dependence of resistive transition to get both T_c^{onset} and T_c^{zero}. The T_c^{onset} and T_c^{zero} change along with the increasing applied pressure are plotted in Figure 1. 17. [87] In this measurement, the transition becomes sharper around 0.5 – 1 GPa indicated by the narrower distance between T_c^{onset} and T_c^{zero} in Figure 1. 16. The T_c increases up to 37 K above 4.15 GPa.

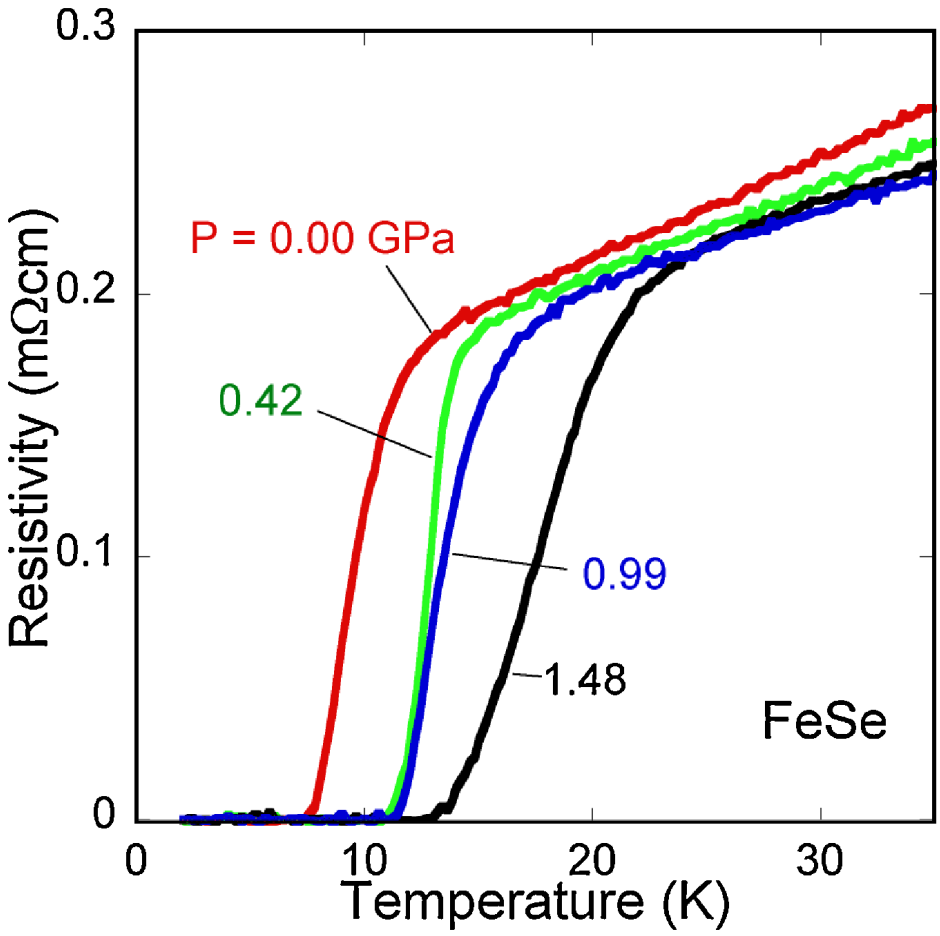

Figure 1. 16 Temperature dependence of resistivity for FeSe under pressure up to 1.48 GPa.

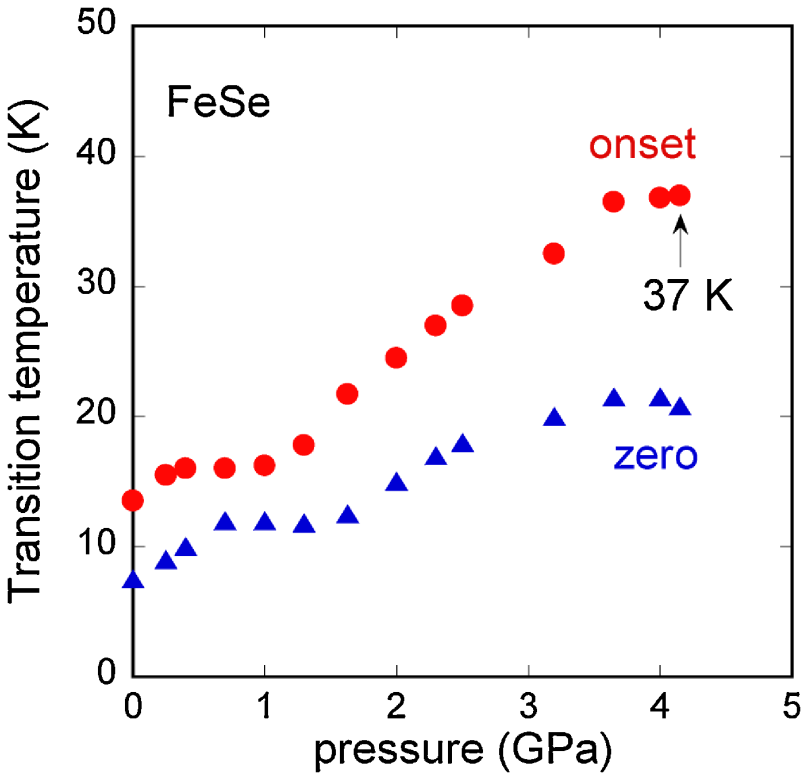

Figure 1. 17 Pressure dependence of T_c^{onset} and T_c^{zero} for FeSe.

High pressure crystal structural analysis of FeSe was performed using synchrotron x-ray diffraction. [31, 37] Change of structure parameters pressure is summarized in Figure 1. 18. The lattice parameters a, b and c and the Fe–Se bonding distance shrink monotonously with increasing pressure. The Se–Fe–Se angle (α angle) decreased from 104.53° to 103.2° with increasing pressure from 0.25 GPa to 9.0 GPa. The highest T_c value does not appear near α ~ 109.47° in regular tetrahedron, which is deviated from what had been predicted for LaFeAsO system [88].

The Se height decreased sharply around 1 GPa, and got the minimum value of ~1.42Å around 4 – 6 GPa associated with significantly increases of T_c as illustrated in the pressure dependence of the Se height and T_c in Figure 1. 21. As shown in the inset of

Figure 1. 18 (e), external pressure above 6 GPa induces the structure transition from orthorhombic to hexagonal transition, which decrease the T_c.

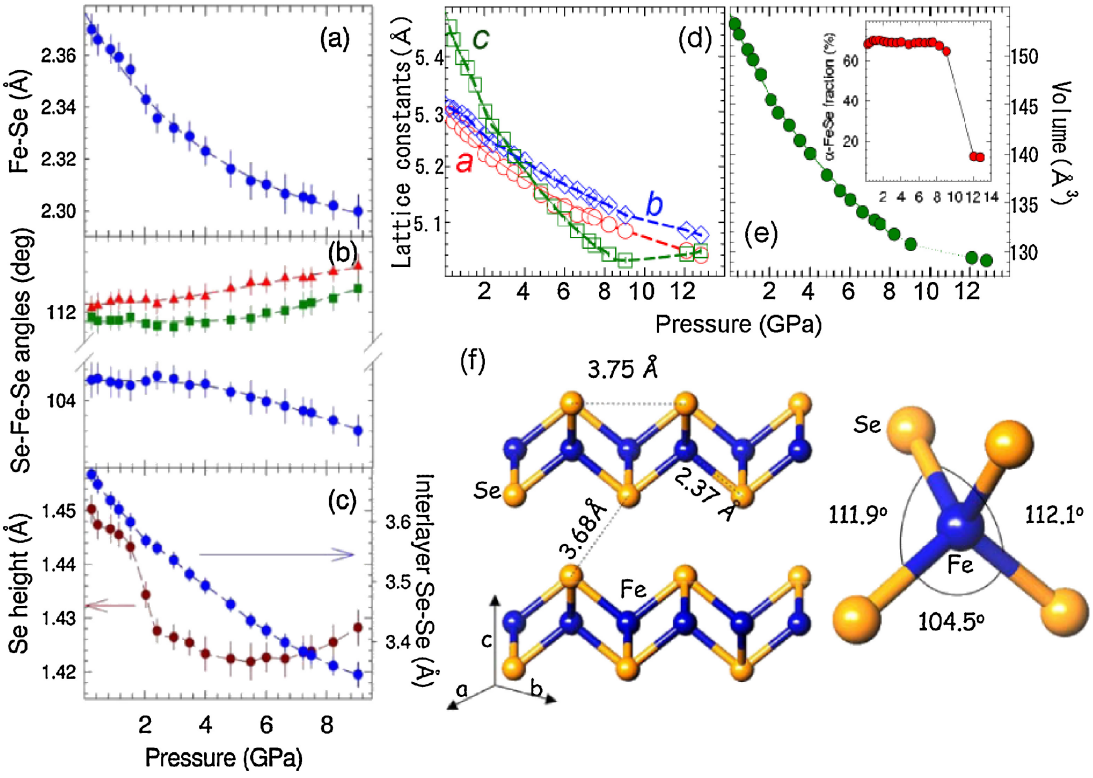

Figure 1. 18 Crystal structural parameters of FeSe under high pressure: (a) Fe–Se distance, (b) Se–Fe–Se angle, (c) Se height from Fe layer, (d) lattice constants a, b, and c, (e) volume, (f) crystal structure of FeSe. The inset in (e) shows the pressure dependence of orthorhombic FeSe fraction. [37]

$FeTe_{1-x}Se_x$

$FeTe_{1-x}Se_x$ has the highest T_c among the Fe chalcogenide superconductors at ambient pressure. $FeTe_{1-x}Se_x$ also shows positive pressure effect as FeSe. [89-91] Figure 1. 19 (a) shows the plot of resistivity versus temperature for $Fe_{1.03}Te_{0.43}Se_{0.57}$ under external pressure up to 11.9 GPa. Figure 1. 19 (b) presents a pressure versus temperature phase diagram for $Fe_{1.03}Te_{0.43}Se_{0.57}$. The T_c decreases in the pressure region around 2 – 3

GPa due to orthorhombic-monoclinic transition. Furthermore in the composition close to the AFM ordered, the $FeTe_{0.75}Se_{0.25}$ shows a positive pressure effect. Superconducting volume fraction as well as the T_c was enhanced with increasing pressure. [75]

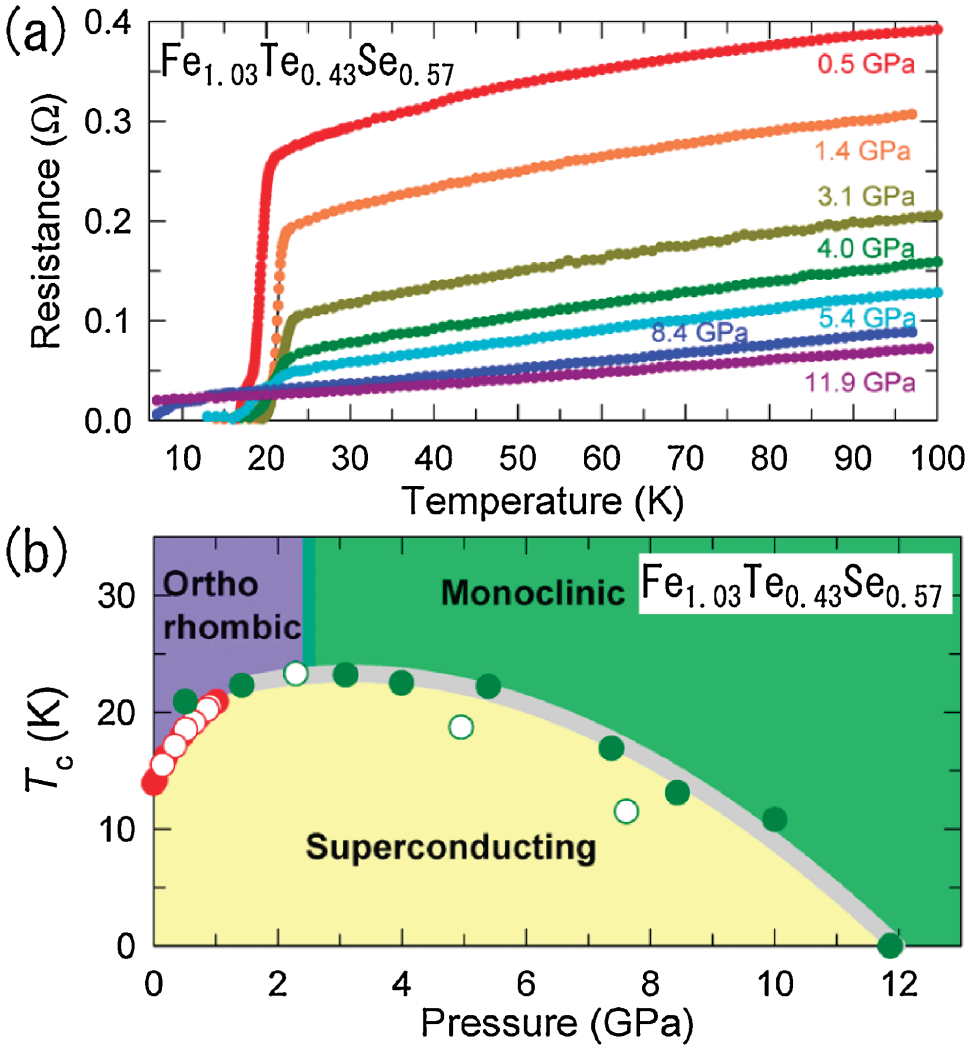

Figure 1. 19 (a) Temperature dependence of resistivity for $Fe_{1.03}Te_{0.43}Se_{0.57}$ under high pressure up to 11.9 GPa. (b) Pressure vs. temperature phase diagram of $Fe_{1.03}Te_{0.43}Se_{0.57}$. [89]

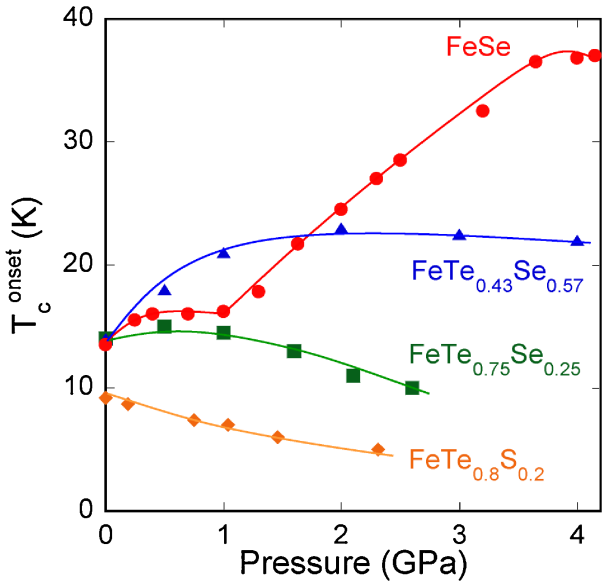

Figure 1. 20 Pressure dependence of T_c^{onset} for the Fe-chalcogenide superconductors.

1.2.4 Anion Height Dependence of T_c

Various pressure effects of the Fe-chalcogenide superconductor with different composition are summarized in Figure 1. 20. The pressure dependence of superconductivity can be correlated with the local structure. The anion (Se or Te) height from the Fe layer is strongly coupled with the T_c of iron-based superconductors. Theoretical study suggests the nodeless high T_c and nodal low T_c pairings are controlled by the anion height [92]. Figure 1. 22 (a) presents the anion height dependence of T_c for the iron-based superconductors. Figure 1. 22 (b) shows a schematic diagram of anion height in the Fe layer. The data points are for the highest T_c in the corresponding system with the valence of Fe close to 2^+ [82]. The anion height dependence of T_c shows a peak around 1.38 Å in the symmetric hand-fitting curve.

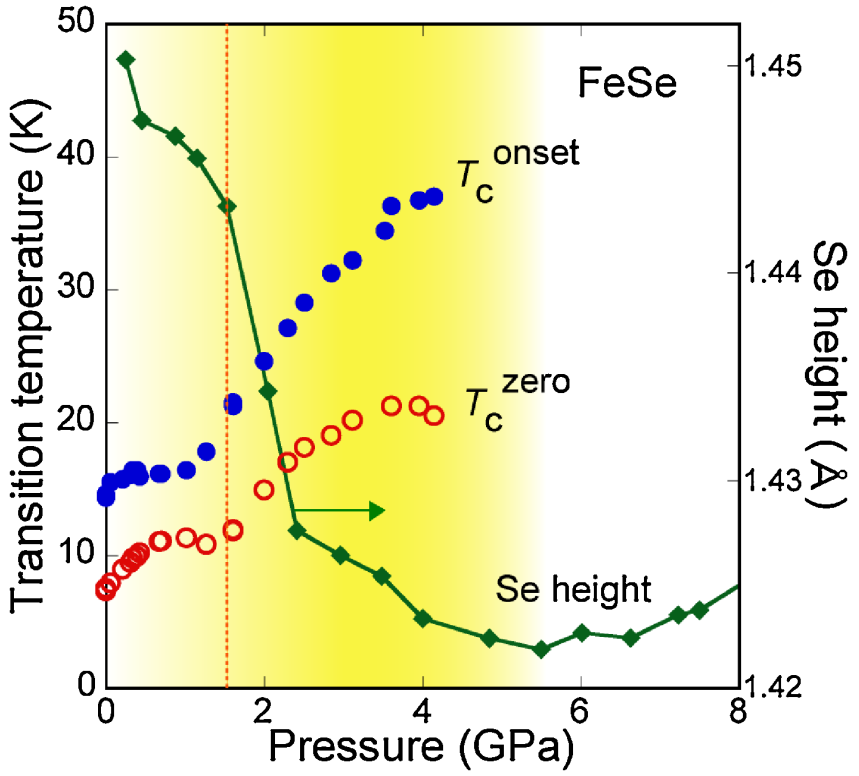

Figure 1. 21 Pressure dependence of T_c and Se height from the Fe layer.

Interestingly, FeSe under high pressure above 2 GPa agrees with the curve which indicates an intrinsic superconductivity under high pressures.

According to the curve, the data point of $FeTe_{0.43}Se_{0.57}$ with optimal T_c around 23 K at ambient pressure should have anion (Se/Te) height of 1.45 Å. In fact, the anion height is much higher at the optimal pressure with a value of 1.598 Å. The anion site disorder exists in $FeTe_{1-x}Se_x$ which is verified by high-resolution x-ray diffraction for $FeTe_{0.56}Se_{0.44}$ that the anion heights of Te and Se are quite different with a $\Delta h_{Te-Se} = 0.24$ Å. [93] Thus, a greater understanding of anion height dependence of the superconductivity in iron-based superconductors requires a more detailed microscopic analysis.

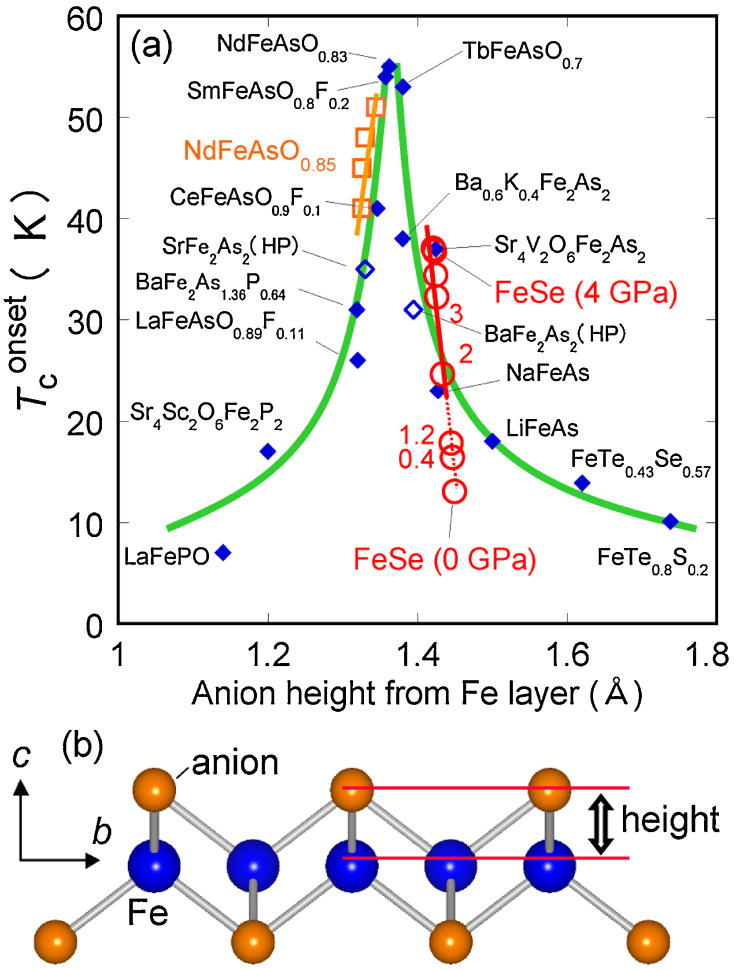

Figure 1. 22 (a) Anion height dependence of T_c of the typical iron-based superconductors. Filled and open marks indicate the data points at ambient pressure and under pressure, respectively. (b) Schematic image of the anion height from the Fe layer.

1.3 Iron Chalcogenide Thin Films

1.3.1 Properties Comparison to Bulk

For the iron-based superconductor with layered structure, compared with its bulk counterpart, superconductor thin film has a great potential in developing the ordered quasi-2D structure and is suitable for coating technology which has already been applied

in $YBa_2Cu_3O_{7-x}$ coated conductors [56]. In addition, the high quality epitaxial thin film is an ideal template to do comparison study with the theoretical calculation.

After the discovery of iron-based superconductors, because of higher T_c of iron pnictides, a lot thin film researches have been carried out for the pnictides system such as the '122' iron based superconductors [94-96]. The T_c of the FeSe or $FeTe_{1-x}Se_x$ thin films was not as good as the single crystals due to the epitaxial quality of the thin films [45, 55, 97-100]. Only recently, higher T_c has been achieved in thin films than in bulk [47, 63, 101, 102]. Even for the bulk FeTe considered to be non-superconducting the epitaxial FeTe superconducting thin films have been demonstrated by strain effect [103] and oxygen incorporation [104, 105].

1.3.2 Control of the Thin Film Growth

The growth condition is found to be critical for the superconducting properties of the thin film. FeSe, FeTe, $FeTe_{1-x}Se_x$ and $FeTe_{1-x}S_x$ superconducting thin films have been successfully deposited by PLD, and the superconducting properties are very sensitive to the film composition.

FeSe thin films

Nie *et al.* reported tetragonal phase FeSe films with different thickness deposited on MgO, $SrTiO_3$ and $LaAlO_3$ substrates by PLD [45]. They found better superconducting properties with $T_c^{onset} \sim 8K$ in the thin film on LAO substrate with lattice mismatch of 0.64% and thick films on MgO And STO substrates in tensile strain state with lattice mismatch of 3.7% and 12%. They claim in the latter case the strain and stress on MgO and STO substrates was relaxed above a critical thickness of ~50 nm, so

they concluded that the superconductivity of the FeSe films was suppressed by the tensile strain. However, in this study only T_c^{onset} shows up without the T_c^{zero} down to 4K, which indicated that film growth was not optimized.

Han *et al.* have reported epitaxial $FeSe_x$ films with x = 0.80, 0.84, 0.88 and 0.92 on LAO substrates deposited by PLD. higher T_c^{onset} ~12 K was found for x = 0.88 and 0.92 although T_c^{zero}s are below 4 K [55].

Wang *et al.* have demonstrated FeSe films with T_c^{zero} around 4 K on MgO substrates [54]. FeSe thin films with various thicknesses and two deposition temperatures 320 °C as LT-FeSe and 500 °C as HT-FeSe have been deposited on MgO substrate. XRD shows with higher deposition temperature the dominant peak that change from (001) peak in LT-FeSe to the (101) peak in HT-FeSe as shown in Figure 1. 23 (*a*) and also the film orientation is confirmed by the high resolution transmission electron microscopy (HRTEM) image. The R-T plots for the films deposited at different temperatures are shown in Figure 1. 23 (*b*). Although the preferred orientation in favor of superconducting properties is the growth along the c axis, T_c^{zero} of (101) oriented HT-FeSe films is about 4K, while (100) oriented LT-FeSe films only have T_c^{onset} at 2K without zero resistance shown. Thickness dependence of the T_c reveals only thick LT-FeSe films are superconducting. Low-temperature XRD measurements at 80K indicate low-temperature structural distortion in the HT-FeSe and thicker LT-FeSe which is strongly correlated with the existence of superconductivity in the FeSe system. In the thinner LT-FeSe films most likely the structural distortion is suppressed by this strain effect while the effect is relaxed above the critical thickness in the thicker film.

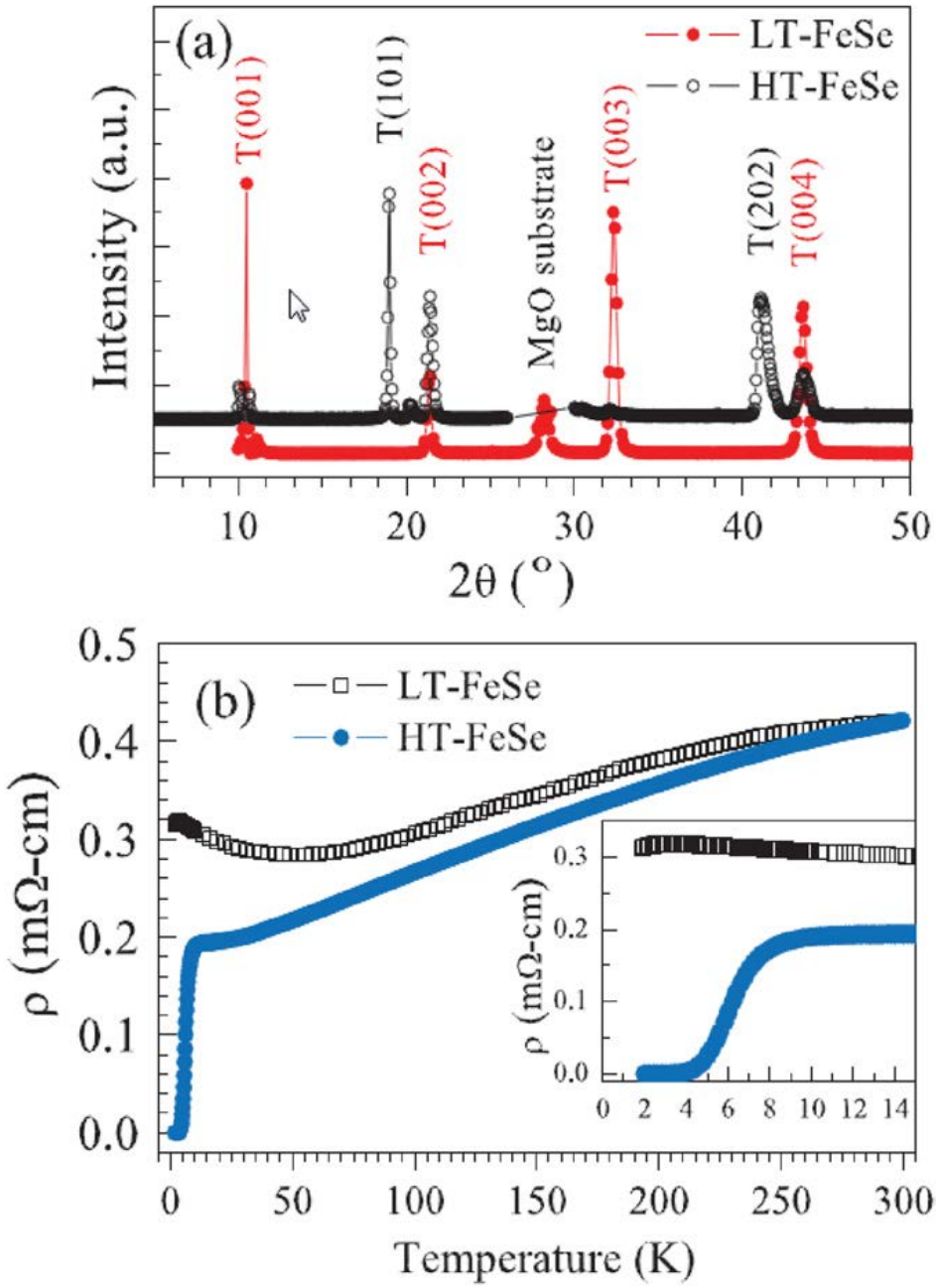

Figure 1. 23 (*a*) XRD plots and (*b*) R-T plots for both LT- and HT-FeSe films [54]

Chen *et al.* have reported FeSe thin films deposited on LAO, STO, MgO, Si(100) and amorphous SiO_x substrates at 320 °C by PLD [97]. The T_c^{zero} is only shown on LAO,

STO and MgO and not presented for the Si(100) and amorphous SiO_x substrates down to 2 K although from the XRD the tetragonal phase is confirmed [97].

Recently, Jourdan *et al.* reported higher T_c^{zero}s (~6.5 K), in FeSe superconducting thin films made by MBE deposition on $YAlO_3$(110) with a mismatch of 2.5 % and 1.8 %. [101].

Chen *et al.* have reported tetragonal phase FeSe thin films grown on STO (001) and MgO (001) at various substrate temperatures with post annealing by PLD. The critical transition temperature of the thin films ranges from 2 K to 11.5 K depending on the deposition temperature and annealing condition. The samples with higher critical transition temperatures show self-assembled Fe_3O_4 nanoparticles in the films according to both XRD and TEM analysis. The formation of Fe_3O_4 nanoparticles could assist the formation of the tetragonal FeSe phase by consume the extra Fe due to the loss of the Se element during the PLD and thus lead to the enhanced superconducting properties [100].

Jung *et al.* reported films with thickness over 1μm grown on Al_2O_3 (0001), $SrTiO_3$ (100), MgO (100) and $LaAlO_3$ (100) substrates by PLD at temperature as high as 610 °C with T_c^{zero} of 8.2 K. The film orientation is along the (101) direction as the HT-FeSe on MgO substrate, which is responsible for the high T_c comparable to the bulk and much higher than the previous FeSe films [106]. One interesting phenomenon is the low resistivity for the film on the STO substrate, which may be originated from the oxygen vacancy in STO due to oxygen reaction with Fe elements. Jung *et al.* also estimated upper critical field $H_{c2}(0)$s to be 58 T, 56 T, 50 T and 57 T for films deposited on Al_2O_3

(0001), $SrTiO_3$ (100), MgO (100) and $LaAlO_3$ (100) substrates, respectively, using a T_c^{onset} and a linear extrapolation [106].

With the sophisticated control of the thin film growth, very recently Wang *et al.* reported high T_c in one or several unit-cell (UC) thick FeSe films grown on STO (001) substrate by MBE. The transport measurement shows that T_c^{onset} is above 50 K as shown in Figure 1. 24 and perhaps as high as 77 K. [107]

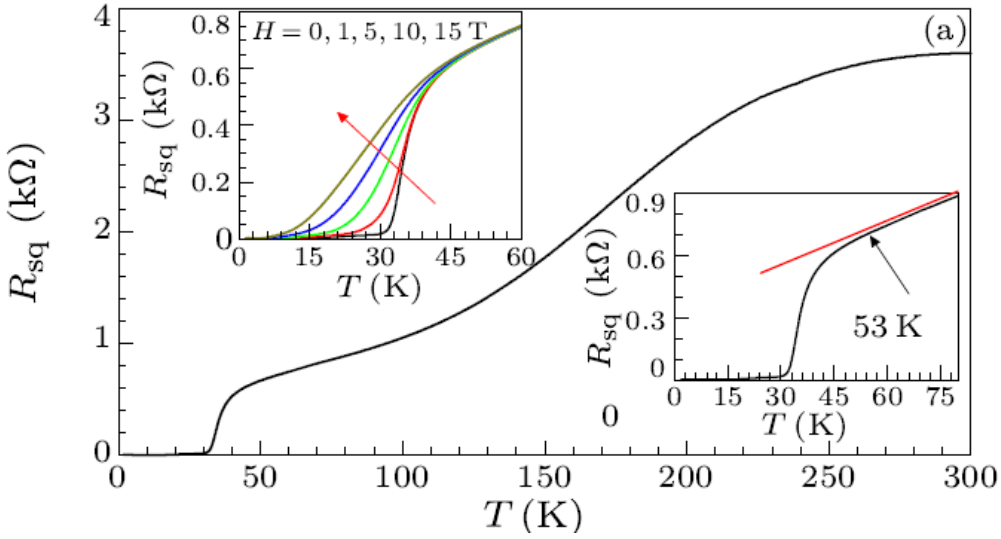

Figure 1. 24 (a) Temperature dependence of square resistivity (R_{sq}) of a 5-UC-thick FeSe film on insulating STO(001) surface from 0 to 300 K. Upper inset: R_{sq} - T curves under magnetic field up to 15 T along the c-axis. Lower inset: the R_{sq} - T curve from 0 to 80 K.

$FeSe_{0.5}Te_{0.5}$ thin films

Since $FeSe_{0.5}Te_{0.5}$ has been considered the optimum composition with the highest T_c, many groups carried out research on the $FeSe_{0.5}Te_{0.5}$ thin films.

Si *et al.* grown high quality superconducting $FeSe_{0.5}Te_{0.5}$ thin films by PLD with T_c significantly higher than bulk [102]. Figure 1. 25 (*a*) shows a θ–2θ scan of the film on

STO (100) substrate. As shown in the Figure 1. 25 (b) and (c), the preferred out-of-plane orientation of the film is $FeSe_{0.5}Te_{0.5}$ (001) direction which is also confirmed by the cross-sectional HRTEM image. The φ-scan of the (112) peaks for the film and the substrate in Figure 1. 25 (*b*) and (*c*) indicate a four-fold symmetry which indicates the film is well aligned on the STO substrate. The film a lattice parameter is around 0.3806 nm comparable to the bulk value, but *c* varies from 0.584 to 0.594 nm which is shorter than the bulk value. Transport properties were measured for the 100 nm $FeSe_{0.5}Te_{0.5}$ films, some of the films have T_c around 17 K much higher than those of the bulk.

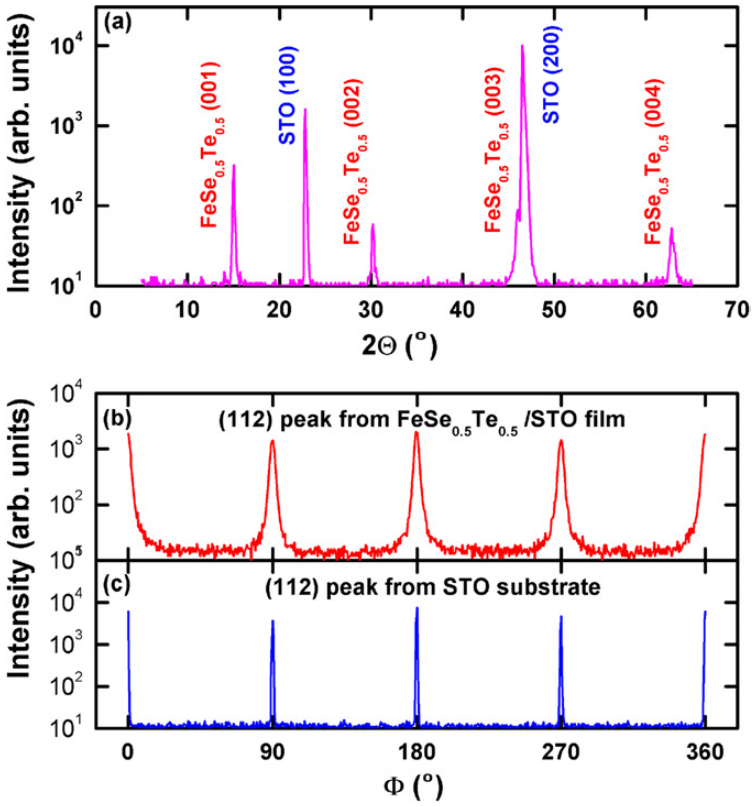

Figure 1. 25 (*a*) θ–2θ and (*b*) φ-scan of the (112) peak for $FeSe_{0.5}Te_{0.5}$ thin film on STO substrate, (*c*) φ-scan of the $FeSe_{0.5}Te_{0.5}$ (112) peak [102].

Si *et al.* reported higher T_c^{onset} up to 20K and T_c^{zero} up to 17 K in $FeSe_{0.5}Te_{0.5}$ films on LAO and STO substrates. The unit cell volume of the film shrinks 2% compared with the bulk, which is similar to the pressure effects to enhance the T_c [31]. Most commonly, both *a* and *c* parameters of the tetragonal structure decrease under hydrostatic pressure. However in some case such as seen in $CaFe_2As_2$ [108] the *c* decreases and at the same time *a* increases a little bit. The $FeSe_{0.5}Te_{0.5}$ film is similar to the $CaFe_2As_2$ under pressure, in which the c axis parameter shrinks and the *ab* lattice parameters remain nearly unchanged. They attributed the shrinkage of *c* to some vacancy due to the oxygen residue in the chamber.

Bellingeri *et al.* have reported T_c^{onset} up to 21 K in the 200 nm epitaxial $FeSe_{0.5}Te_{0.5}$ thin films on various substrates and they attributed the enhancement to the compressive strain state induced by the growth mode [47, 63]. They found that the *c*-axis lattice constant for the film is always smaller than the bulk value and the *a*-axis parameter which is also smaller than the bulk value strongly depend on the film thickness and can be correlated with the T_c change as shown in Figure 1. 26 (*a*) and (*b*). Smaller in-plane lattice parameter in the film indicates the film is under compressive strain regardless of the film substrate matching relationship. The growth model is studied by atomic force microscopy measurements that is the isolated islands form during the initial stage of $FeSe_{0.5}Te_{0.5}$ film growth and in the post coalescence stage it will generate compressive strain. Figure 1. 27 (*a*) shows the T_c dependence on the compressive strain in the $FeSe_{0.5}Te_{0.5}$thin films. From the *a*, *c* and *z* values, the length *d* and the angle α of the Fe–(Se, Te) bond were calculated. In Figure 1. 27, higher T_c shows in the samples

with the structure close to a regular tetrahedron with bond angle of 109.47°, and the bond length is ~ 2.40 Å.

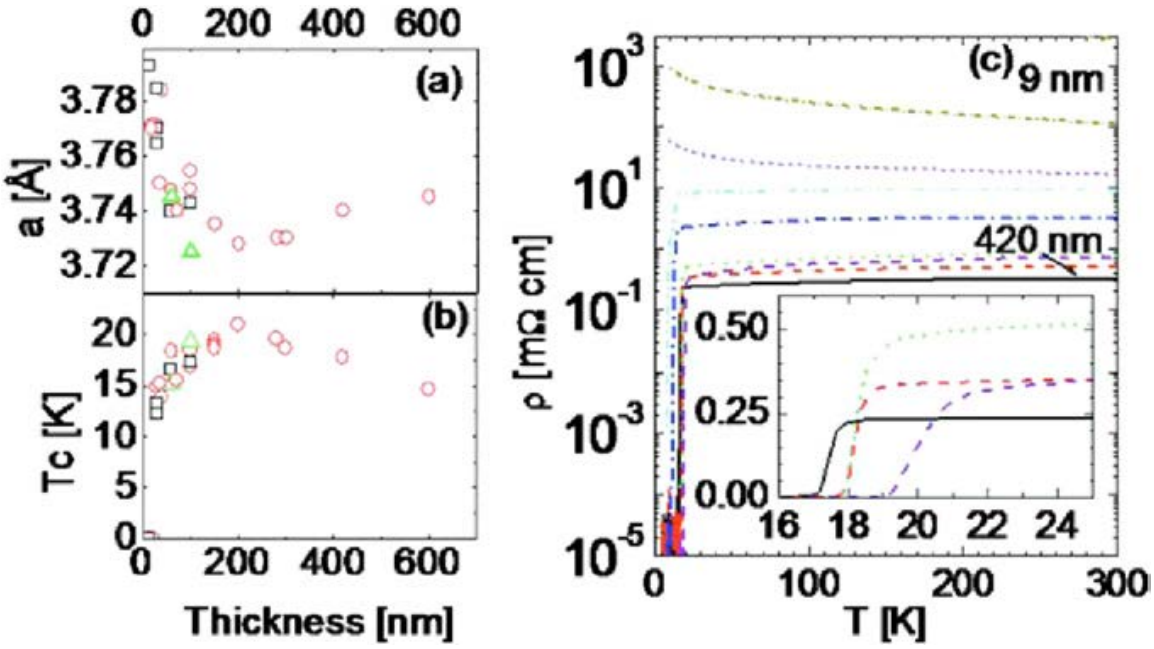

Figure 1. 26 The thickness dependence of (a) a-axis lattice constant and (b) T_c values for the $FeSe_{0.5}Te_{0.5}$ films. (c) R-T plots of $FeSe_{0.5}Te_{0.5}$ films with various thicknesses on LAO substrates [63].

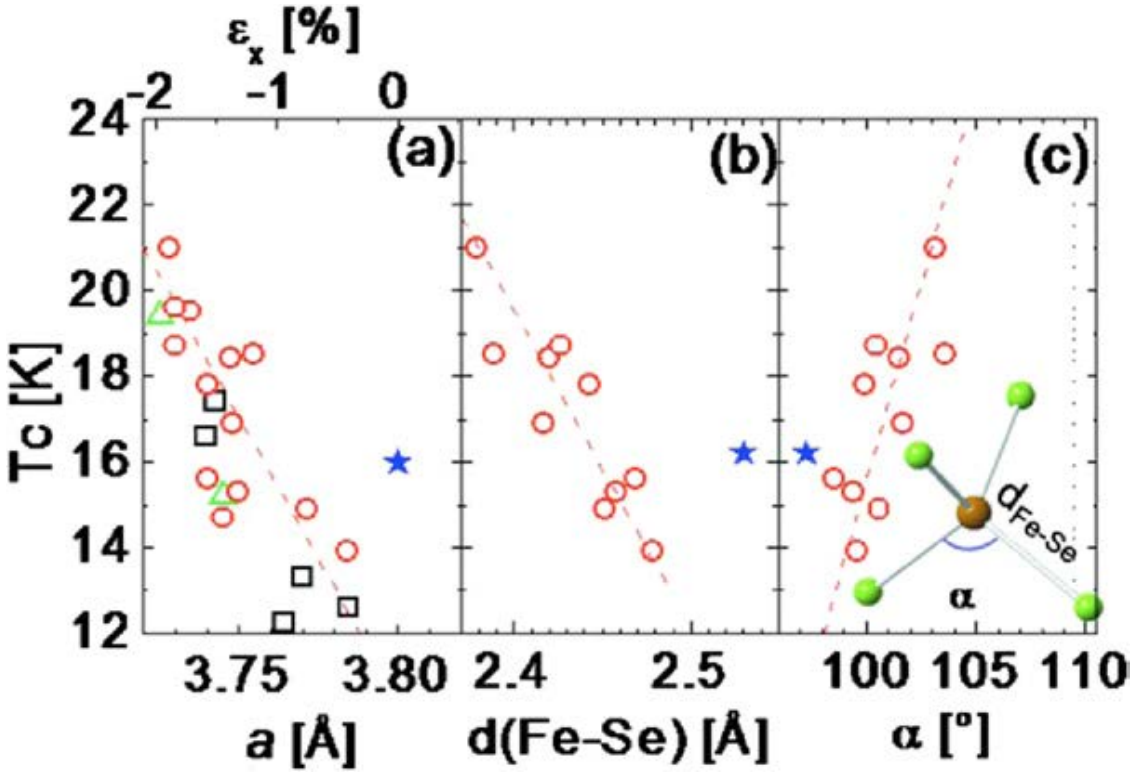

Figure 1. 27 T_c dependence on (a) the in-plane lattice constant a, (b) the Fe–(Se, Te) bond length and (c) (Se, Te)–Fe–(Se, Te) bond angle. The stars represent the bulk values [63].

Since in most studies the oxide substrates were used, Tsukada *et al.* also argued that the oxygen contamination during film growth is very important to the thin film lattice parameters [109]. With CaF_2 (100) substrates the $FeSe_{0.5}Te_{0.5}$ thin films have T_c higher than 15K, however the *c*-axis lengths are longer (>5.94 Å) and the *a*-axis lengths are shorter (~3.78 Å) [63]. The J_c at 10 K was one order of magnitude higher than that of $FeSe_{0.5}Te_{0.5}$ crystal and the J_c decreases very slowly under magnetic field [109].

FeTe thin films

According to a density functional calculation, FeTe as the parent compound of the '11' system is supposed to have the highest T_c among '11' family [60], however the

bulk FeTe is not superconducting instead it experiences an AFM transition at about 70K along with a structure transition from tetragonal to monoclinic.

However for the thin film Han *et al.* have observed superconducting FeTe films with T_c of 13K under tensile epitaxial strain [103]. The target used in this study has with nominal composition of $FeTe_{1.4}$ and the thin films were deposited 2×10^{-4} Pa on LAO, MgO, STO and LSAT substrates at 500–580 °C. Resistivity versus temperature plots for both the bulk FeTe and the FeTe thin film on MgO substrate were presented in Figure 1. 28. The anomaly corresponding to the AFM transition is suppressed and superconductivity appears with T_c^{onset} of 13 K in the thin film on MgO and they attribute it to the tensile strain and stress from the substrate/film mismatch.

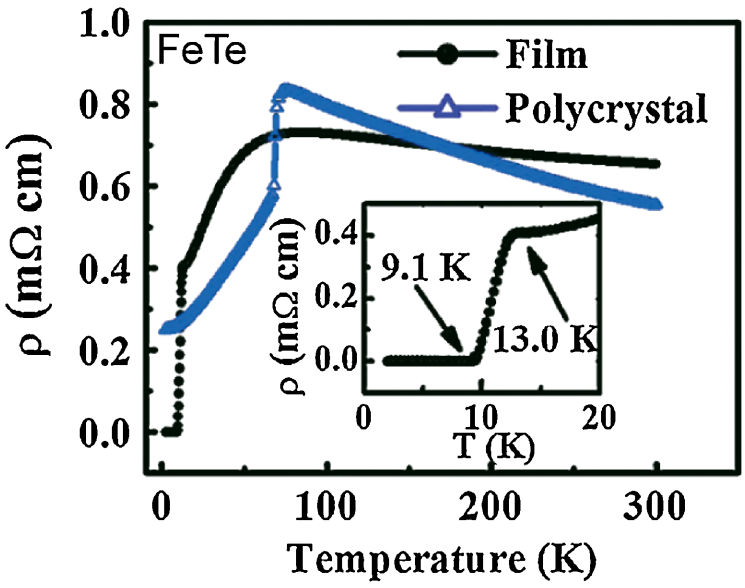

Figure 1. 28 Temperature dependence of resistivity of FeTe for the polycrystal and thin film on MgO.

Si *et al.* also reported superconducting FeTe thin films induced by PLD deposition in a controlled oxygen atmosphere [104]. The deposition temperature was ~

400 °C. They found the T_c^{onset} around 10 K in the FeTe thin films deposited with base pressure of 2×10^{-7} Torr which did not exclude the possibility of oxygen incorporation into the films due to the oxygen residual in the chamber. Later on they intentionally deposited the thin film with oxygen pressure of 10^{-4} Torr and T_c^{onset} of ~ 12.5K and T_c^{zero} of ~7.5 K was observed in the deposited thin film. These films may contain oxygen and the superconductivity may be induced by the oxygen substitution of Te and it is also possible the oxygen goes to the interstitial site to reduce the excess Fe that creates localized magnetic moments. One possibility is that a phase separation at low temperatures, which is supported by the simultaneous observation of the AFM transition and superconductivity similar to the observation in $SmFeAsO_{1-x}F_x$ [110] and $Ba_{1-x}K_xFe_2As_2$ [111]. Figure 1. 29 shows the R-T plot for the $Fe_{1.08}Te : O_x$ thin film. The film has a bump at 60 K in the R-T plot corresponding to the structure and AFM phase transitions which was observed in bulk at 70 K.

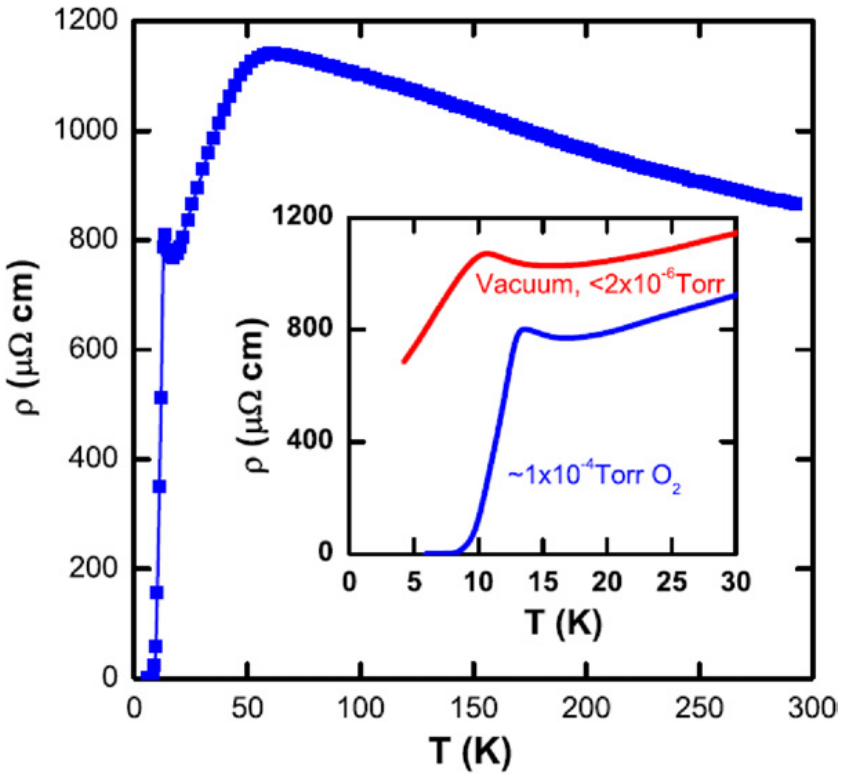

Figure 1. 29 R-T plot of the FeTe:O_x film on STO substrate. The inset shows the comparison of the FeTe films deposited in oxygen and under vacuum [104].

Si *et al.* also took the resistance vs. temperature measurements under magnetic field up to 9 T along the *c*-axis of the FeTe. The irreversibility line $H_{irr}(T)$ and the upper critical field $H_{c2}(T)$ were estimated to be ~200 T from the T_c^{onset} [104].

Nie *et al.* have also reported that superconducting FeTe films induced by oxygen incorporation in a reversible manner [105]. The deposition was done at 380 °C with base pressure of 2×10^{-7} Torr. The nonsuperconducting as-deposited films show superconductivity after being exposed to the air. Later, the as-deposited films were annealed under multiple conditions: 100 °C in 100 mTorr oxygen, carbon dioxide, nitrogen, in 40 °C water and 2×10^{-7} Torr vacuum. The superconductivity in FeTe films

can be only induced in oxygen annealing, as shown in Figure 1. 30 (*a*) – (*f*). Furthermore, the superconductivity can be removed or induced by vacuum or oxygen annealing in a reversible manner as shown in Figure 1. 30 (*g*).

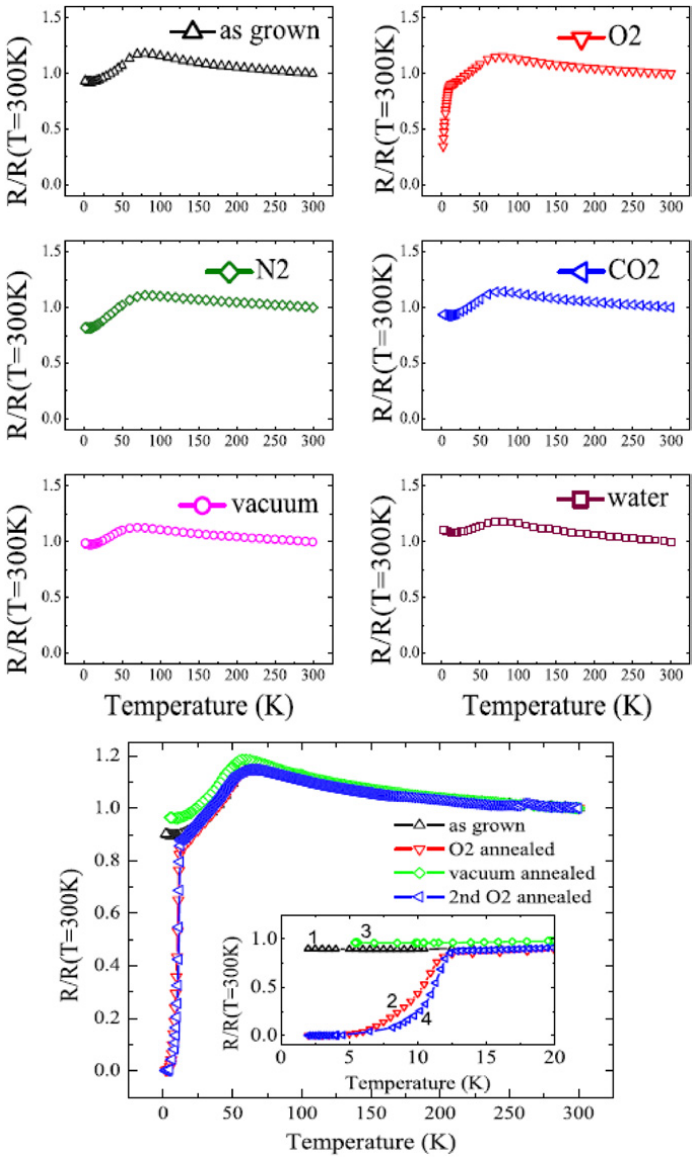

Figure 1. 30 R-T plots for (*a*) as- deposited FeTe films, and films annealed in (*b*) O_2, (*c*) N_2, (*d*) CO_2, (*e*) vacuum and (*f*) water. (*g*) Reversible superconductivity after oxygen and vacuum annealing cycle [105].

1.3.3 Iron Chalcogenide in Coated Conductor

Towards the practical high-field application, coated conductor technology was applied in the iron chalcogenides with high J_c under magnetic fields up to 25 T and even the simplification of coated conductor technology on amorphous substrate was demonstrated as shown in Chapter V and VI [67, 112-114].

Currently low temperature superconductor Nb_3Sn is still the dominant superconductor material used for high-field applications up to 20 T at 4.2 K [115]. High temperature superconducting (HTS) wires have gone through a revolution in the past two decades. The "first generation" (1G) powder-in-tube (PIT) HTS wires are based on the traditional wire drawing of the $Bi_2Sr_2Ca_2Cu_3O_{10+x}$ (BSCCO) (T_c = 112 K). However the grains in the wire are not well aligned which results in low J_c and also the cost is relatively high due to the use of silver in these superconducting wires. [116] The "second generation" (2G) HTS coated conductor wires are based on the high quality epitaxial growth of $YBa_2Cu_3O_{7-\delta}$ (YBCO) films on either rolled textured metal substrates (RABiTS) [117] or the ion-beam-assisted deposition of highly textured template (IBAD) on metal substrates [118-120].

Generally YBCO and other HTSs still have higher J_c than the iron chalcogenides, but their applications are hindered by high processing costs. In the above two generations of HTS wires, either highly epitaxial template for the growth of YBCO film at around 800 °C with the oxygen annealing afterwards, or rolling and post-heat treatment for the case of highly textured BSCCO wires is required. In contrast lower manufacturing cost was expect the for the iron chalcogenide coated conductors; the

processing temperature is as low as ~ 400°C without oxygen annealing which can also prevent the oxidation of the metal substrate.

In addition to the high cost to process the HTS such as $YBa_2Cu_3O_7$ (YBCO), other problems which limited its applications include high anisotropy and brittle texture. In comparison, the extremely high H_{c2} and moderate anisotropies with H_{c2}^{ab}/H_{c2}^{c} ~ (1 – 8) in the iron chalcogenide makes it suitable for high-field applications.

Another challenge for the HTSs is the sharp drop of J_c across the misaligned grains. It was reported the high angle grain boundaries significantly reduced J_c in $Ba(Fe_{1-x}Co_x)_2As_2$ [121]. This may not be as severe as that in $FeSe_{0.5}Te_{0.5}$ suggested by the superconducting properties of the $FeSe_{0.5}Te_{0.5}$ growth on amorphous substrate with highly out of plan texture while without long order in plane texture [112].

Towards the practical application the Fe(SeTe) wires were made by the power-in-tube method [122, 123], however the critical current density is still not high enough for the practical application. Very recently, IBAD epitaxial MgO coated Hastelloy substrates were used to grow high quality $FeSe_{0.5}Te_{0.5}$ tapes with excellent in-field performance with nearly isotropic J_c at 4.2 K [67]. The films demonstrated on IBAD substrate involve multiple steps of seed layer and buffer layer deposition to establish the epitaxial growth template for the following iron chalcogenide growth. First, Y_2O_3 layer was coated on Hastelloy to reduce the surface roughness, then IBAD MgO layer was deposited to create the cubic template [118-120].0 Although the T_c^{onset} is almost the same, the IBAD film has a lower T_c^{zero} of ~11 K than the bulk of ~14 K, which could be

related to the defects caused by mismatch between the MgO substrate and the $FeSe_{0.5}Te_{0.5}$ film [67].

Figure 1. 31 shows the J_c dependence on magnetic field for the films on LAO and IBAD substrates at different temperatures. In both films, J_c is nearly isotropic at 4 K, indicated by the solid (H||c) and void (H||ab) data point. The $J_c^{self\text{-}field}$ of films on LAO at 4 K is ~5×10^5 Acm^{-2} and still above 1×10^4 Acm^{-2} up to 35 T. The J_c decreases slowly under magnetic field. The self-field J_c of films on IBAD is 2×10^5 Acm^{-2} at 4K, the J_c which is slightly lower than film on LAO and J_c decreases quickly above 20 T with a J_c of 1×10^4 Acm^{-2} at 25 T.

Since MgO has a cubic lattice constant of 4.11 Å much larger than the *ab* lattice constant of $FeSe_{0.5}Te_{0.5}$ of 3.81 Å, later on CeO_2 with much closer lattice matching constant (cubic, a=5.41/ $\sqrt{2}$ ~3.82 Å) with $FeSe_{0.5}Te_{0.5}$ has been used as buffer. Recent study indicates CeO_2 buffer can significantly improve the T_c and J_c of epitaxial $FeSe_{0.5}Te_{0.5}$ films. The highest T_c for the film with a CeO_2 buffer layer is ~20 K for T_c^{onset} and ~18 K *for* T_c^{zero}. The nearly isotropic J_c is as high as $1MAcm^{-2}$ for self-field and remains as high as $10^5 Acm^{-2}$ up to 30 T at 4.2 K. These properties show that $FeSe_{0.5}Te_{0.5}$ thin film is promising for high-field magnets at liquid helium temperatures.[114]

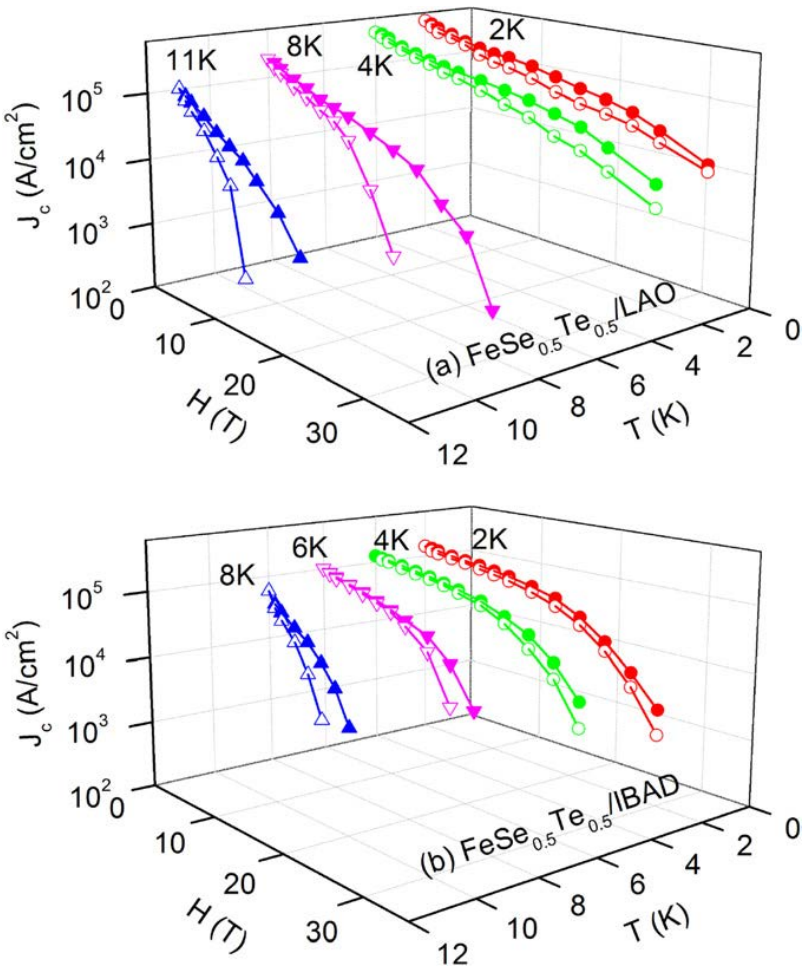

Figure 1. 31 J_c of $FeSe_{0.5}Te_{0.5}$ films on (*a*) LAO substrate and (*b*) IBAD coated conductor at various temperatures with magnetic field parallel (open) and perpendicular (solid) to the *c*-axis (tape surface) [67].

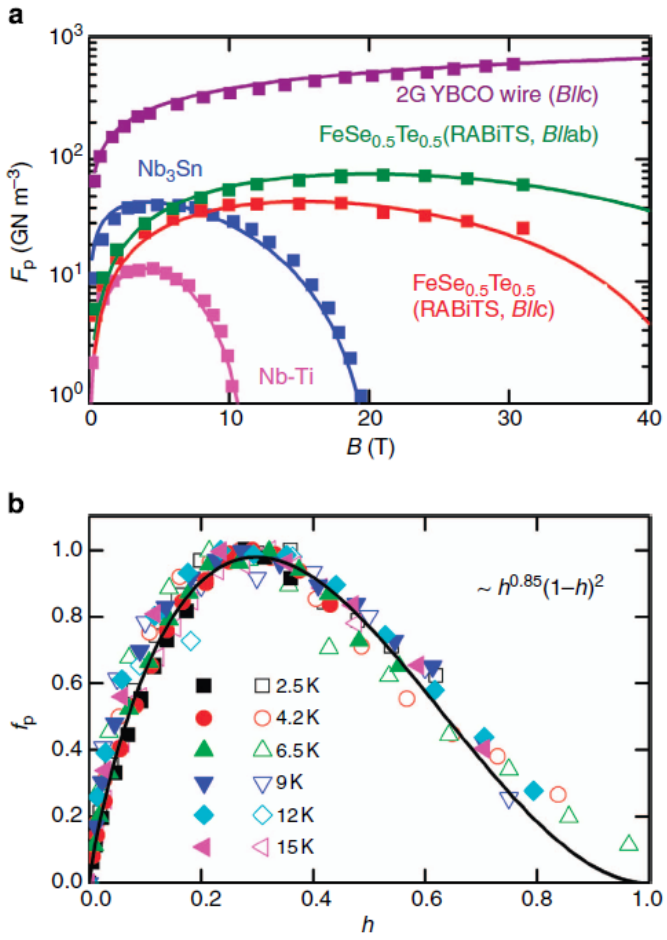

Figure 1. 32 Pinning force analysis for a $FeSe_{0.5}Te_{0.5}$ film grown on RABiTS. (a) F_p at 4.2 K of a $FeSe_{0.5}Te_{0.5}$ film grown on a RABiTS substrate, compared with the literature 2G YBCO wire, Nb-Ti and Nb_3Sn. Solid lines are Kramer's scaling approximations. (b) Kramer's scaling approximations for a $FeSe_{0.5}Te_{0.5}$ film grown on a RABiTS substrate at various temperatures with field perpendicular (solid symbols) and parallel (open symbols) to *c*-axis. [114]

$FeSe_{0.5}Te_{0.5}$ film on RABiTS substrate presents superior high-field performance above 20 T compared to the YBCO wire [124], thermo-mechanically processed Nb47Ti alloy [125, 126] and small grain Nb_3Sn wire [127, 128], as shown in the field dependence of the volume pinning force F_p in Figure 1. 32.

In Figure 1. 32, the Kramer's scaling law approximation $f_p \sim h^p(1-h)^q$ is shown for a $FeSe_{0.5}Te_{0.5}$ film grown on a RABiTS substrate at various temperatures with the $H||c$ and $H||ab$, where $f_p = F_p / F_p^{max}$ is the normalized pinning force and $h = H/H_{c2}$ is the reduced field. For all temperatures and both field directions the data points all fall approximately on the Kramer's scaling law approximation. The high field term q which describes the reduction of the superconducting order parameter is found to be equal to 2 [129]. The low-field term p was found to be ~ 0.5 in Nb_3Sn and YBCO and the F_p^{max} can not be enhanced by the pinning center density anymore because flux swiping by shearing the vortex lattice instead of de-pinning [130]. In contrast p is found to be ~ 0.85 ($h^{0.85}$) in $FeSe_{0.5}Te_{0.5}$ which indicates point-defect core pinning mechanism [129]. The F_p is the product of the individual F_p times the pinning center density for the point defects pinning. This suggests there is still room to enhance the in-field performance of $FeSe_{0.5}Te_{0.5}$ by adding more point defects as pinning centers. The ideal pinning points' density in $FeSe_{0.5}Te_{0.5}$ is pretty high according to the short coherence length of 1–3 nm.

The mechanism for the high J_c values in the film with the CeO_2 buffer layer is still under investigation. The enhanced critical current density was also observed with CeO_2 interlayer. This study suggested the CeO_2 inter layer introduced more defects at the interface which can be effective flux pinning centers to enhance the in-field performance similar to cuprates [131]. Detailed study of the structure-properties relationship is needed to understand the enhanced J_c in the film with the CeO_2 buffer or interlayer. In our research we also focus on correlation of the interface structure to the performance.

1.3.4 Compositional Variation in Iron Chalcogenide

The iron chalcogenide demonstrates the interplay of structure, magnetism and superconductivity; the end-member FeSe and FeTe have quite different physical properties although with a similar crystal structure. FeSe exhibits metallic behavior in the normal state and has a T_c^{onset} of 13 K [27]. The phase diagrams were obtained from the bulk iron chalcogenides with different composition. For the bulk materials the optimum composition seems to be the composition close to $FeSe_{0.5}Te_{0.5}$. For the $FeSe_{0.5}Te_{0.5}$ thin film, the spatial relationship of the intrinsic chemical inhomogeneity of Te, Se, and the interstitial iron has been studied by aberration corrected scanning transmission electron microscopy (Cs-corrected STEM), which indicates near-randomly distributed Se/Te and localized interstitial Fe as shown in the Figure 1. 33 [132].

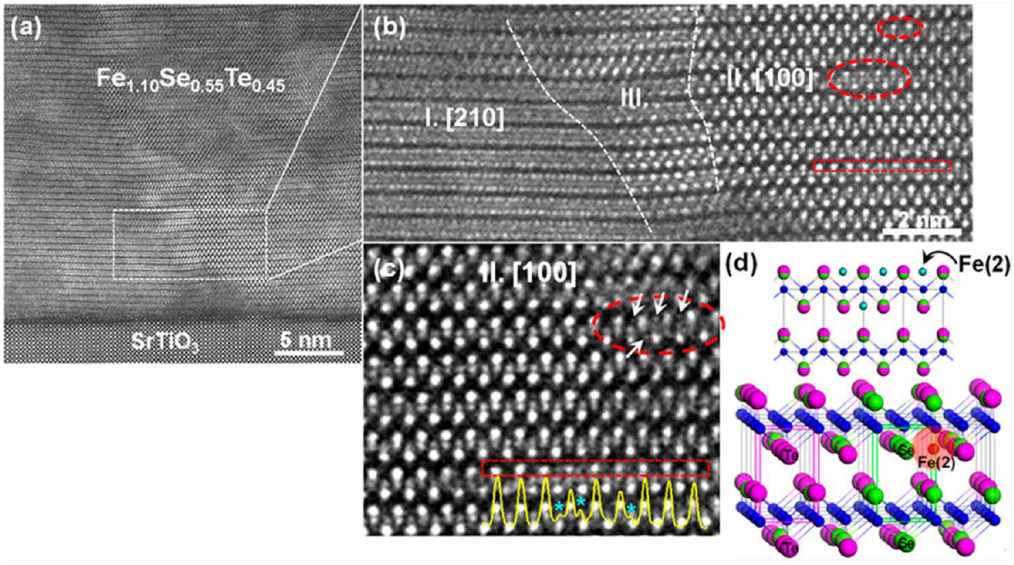

Figure 1. 33 (a) STEM overview of the $Fe_{1.10}Se_{0.55}Te_{0.45}$ film. (b) Enlarged intersection region with three regions with orientations of [210], [100] and the transition region. (c) Enlarged atomic STEM image of the [100] with nanoscale interstitial-iron. Intensity line profile shown along the marked chalcogen plane. Interstitial iron peaks are noted by stars. (d) Schematic illustration of the spatial relationship of Te, Se, and Fe(2) in the parent FST lattice [132].

The effect of the structure in $FeSe_xTe_{1-x}$ films on the T_c enhancement is intensively studied since the discovery of the iron chalcogenide superconductor. Nuclear magnetic resonance (NMR) measurements suggest possible explanation for higher T_c of the bulk FeSe under pressure is enhanced spin fluctuations [46]. Neutron scattering measurements [108] and first principles calculations [60, 133] indicate decrease of the magnetic moment originated from the Fe atoms as the anion height decrease which can be related to the higher T_c in the sample with shorter *c*-axis lattice parameter. Another possibility is that a shorter *c* could suppress the superconducting phase fluctuations by enhancing the interlayer coupling of the Cooper pairs such as observed in the high pressure experiment iron chalcogenide and several unit cell thick FeSe thin film [107, 134]. The high quality epitaxial thin film is an ideal template to do comparison study with the theoretical calculation as well as the bulk results.

In this dissertation, the Te rich iron chalcogenide thin film with composition close to the AFM ordering has been demonstrated. Compared to the optimum composition $FeSe_{0.5}Te_{0.5}$ from the literature report, the $FeSe_{0.1}Te_{0.9}$ is even more promising for the high field application.

Upon small amount of Se doping into the FeTe, high J_c comparable to the optimized composition $FeSe_{0.5}Te_{0.5}$ and extremely high H_{c2} comparable to the $FeTe:O_x$ [104] were achieved. The $FeSe_{0.1}Te_{0.9}$ thin film can be also grown on amorphous substrate such as glass substrate a in a highly textured layer by layer fashion with high performance. In addition the FeTe used to be considered as non-superconducting phase

in bulk form is grown into thin film on various substrates including the glass substrate to show superconducting properties.

CHAPTER II

RESEARCH METHODOLOGY

2.1 Pulsed Laser Deposition (PLD)

In our experiment setup pulsed laser deposition (PLD) with a KrF excimer laser (Lambda Physik Compex Pro 205, λ = 248 nm) will be used for thin film deposition. The pulsed laser deposition system contains the laser system and the vacuum chamber. The term laser stands for Light Amplification by Stimulated Emission of Radiation. The pulsed laser alternates the on and off state periodically. In the past 30 years the PLD has developed significantly and became a widely used technique for thin film growth of a wide range of materials [135].

Physical vapor deposition (PVD) refers to thin film deposition methods with the vaporized materials containing many species such as electrons, ions, atoms, molecules, clusters and particulates from the target condensing onto various substrates in a vacuum chamber. PLD with very simple system setup is categorized into PVD techniques. A PLD system is shown in Figure 2. 1. It consists rotatable target holder oriented at an angle of 45º to the incident laser beam facing a substrate holder in a vacuum chamber maintained by two-stage vacuum system with roughing pump and turbomolecular pump [136]. The base pressure for all the depositions was ~ 10^{-6} Torr. A high power pulsed laser shots onto the target surface to vaporize and transport the material onto the substrate surface. The laser power density was varied from 3 J/cm^2 to 5 J/cm^2 by adjusting the laser output energy. The distance between the target and substrate is usually maintained at approximately 3 - 5 cm in our experimental setup. The substrate

holder can be varied from room temperature to 800 ℃ and a precisely temperature control and sequential ramping can be achieved with computer controlled feedback loops of thermal couple and heater. The film quality depends on a variety of parameters including laser density, substrate temperature, pulse repetition rate, proper working gas, base pressure in the chamber and target to substrate distance.

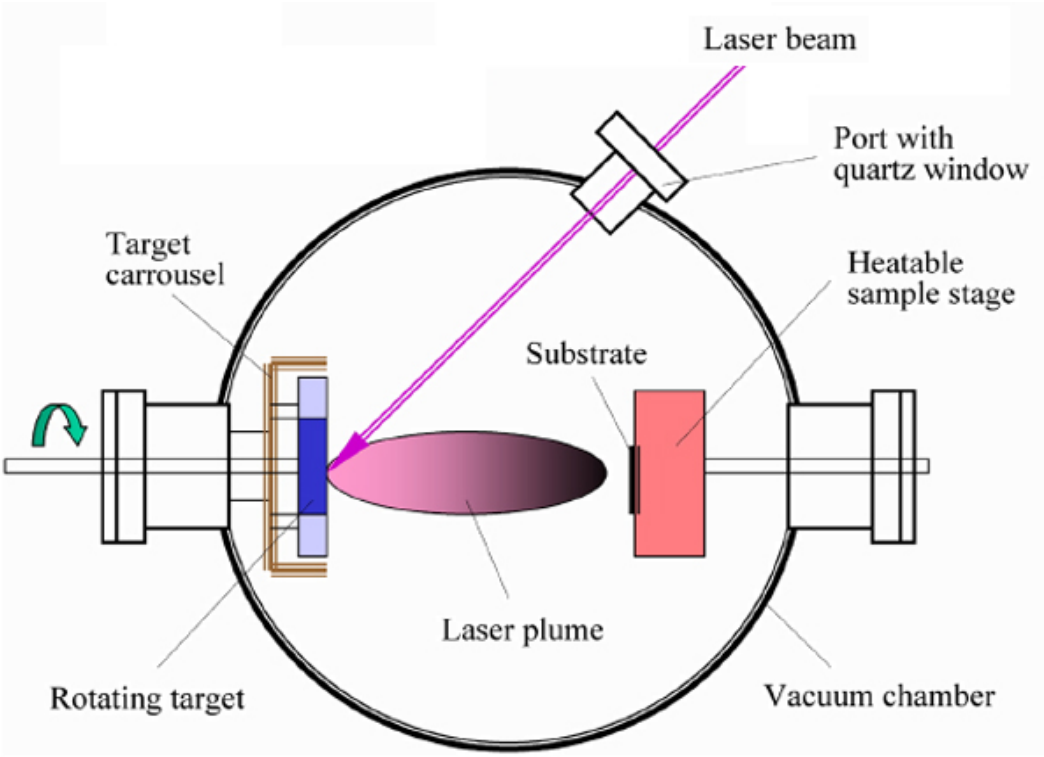

Figure 2. 1 Schematic diagram of the PLD system. [9]

In general, the laser used in PLD for thin film growth has wavelength ranging between 200nm and 400nm. Most of PLD systems use excimer gas to generate laser beam. In this study we will use the KrF laser with wavelength 248 nm which is one of the highest gain systems for electrically discharged excimer laser. Optical components including apertures, mirrors and lenses are placed between the laser and the vacuum

chamber to change the direction and focus the laser beam. The reflective mirror can direct the beam to the designated deposition chamber which enables multiple chambers to share one laser source.

The target is the material to grow into film on the substrate. The incidence laser creates a plume towards the substrate holder of target material containing many species including atoms, molecules, electrons, ions, clusters, particulates and molten globules by means of photon interaction. That is, energy first converted to electronic excitation and then into thermal when the laser pulse is absorbed by the target. Hereafter, chemical and mechanical energy result in evaporation, ablation, plasma formation and even exfoliation. The plume is then collected on a substrate a short distance from the source and high energy molecules ejected from the target will later deposited on the substrate as adatoms and later it will go through the solidification process to make thin film. During the deposition, high deposition temperature is required to provide adatoms enough energy for surface diffusion to move to preferred lattice sites.

In 1990, R. K. Singh and J. Narayan systematically descripted the basic PLD physical principles [137]. The PLD process includes three regimes the laser-target interaction, the interaction of laser beam with evaporated material and adiabatic plasma expansion. The first two regimes happen at the very start of laser radiation and through the laser pulse duration (about 25 ns duration), and the last adiabatic expansion happens right after the laser pulse stops. Figure 2. 2 shows the laser-target interaction during the pulsed laser period [137].

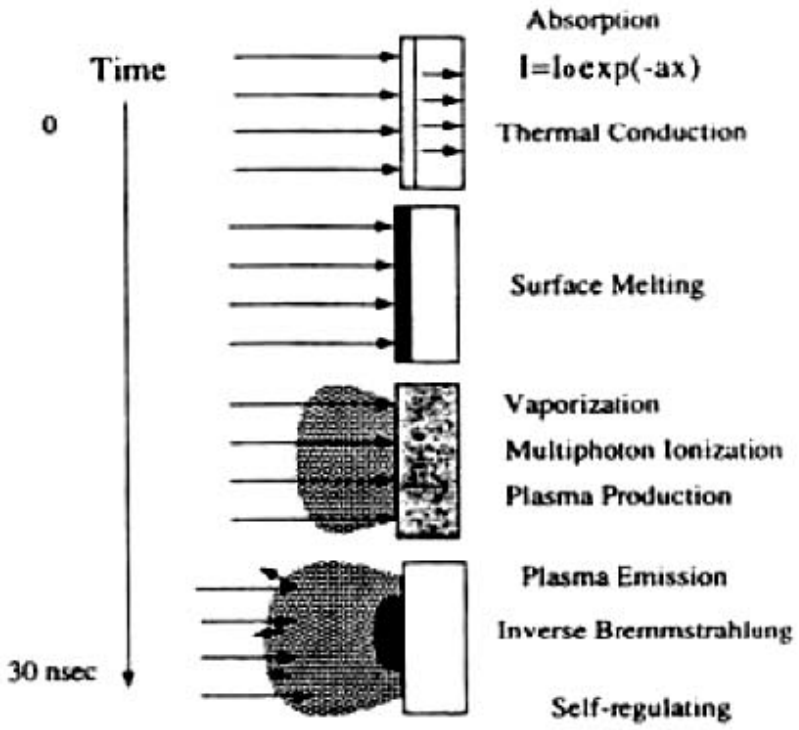

Figure 2. 2. Representation of the laser target interaction stages during the short pulsed laser period.

The interaction between high power laser pulses and the target results in the melting and evaporation of the surface layers. Considering a one dimensional heat flow, the equation is given by:

$$\boldsymbol{\rho_{i(T)}C_{p(T)}}\frac{\partial T(x,t)}{\partial t} = \frac{\partial}{\partial t}\left[\boldsymbol{K_i(T)}\frac{\partial T(x,t)}{\partial x}\right] + \boldsymbol{I_0(t)[1-R(T)]e^{-a(T)x}} \quad \text{(Equation 2. 1)}$$

where x is the distance normal to the surface of the sample and t is the time. $\rho_i(T)$ is density, $C_p(T)$ is thermal heat capacity, $R(t)$ is the reflectivity, $a(T)$ is the absorption coefficient, $I_0(t)$ is the time dependent incident laser intensity and $K_i(T)$ is for the thermal conductivity. The subscript i indicates the phase where $i = 1$ for solid and $i = 2$ for liquid.

The high-power pulsed laser beam irradiation on target surface will cause a temperature high than 2000 K leading to an emission of the positive ions and electrons out of the surface. The thermal emission of ions is calculated from the Langmuir-Saha equation:

$$\frac{i_+}{i_0} = \frac{g_+}{g_0} e^{[(\phi - I)KT]} \quad \text{(Equation 2. 2)}$$

where i_+ and i_0 are the positive and neutral ion fluxes respectively, g_+ and g_0 are the statistical weight of the positive ionic and neutral states respectively, ϕ is the electron work function, and I is the ionization potential of the evaporated material.

The target surface will continually absorb energy from laser radiation since the outer edge of the plasma regime is transparent to the laser beam. A schematic diagram in Figure 2. 3 shows four different regions during the incidence of the laser as 1) the unaffected bulk target, 2) the evaporating target surface, 3) the area near the surface absorbing laser beam energy and 4) the rapidly expanding outer edge which is transparent to the laser beam. [137]

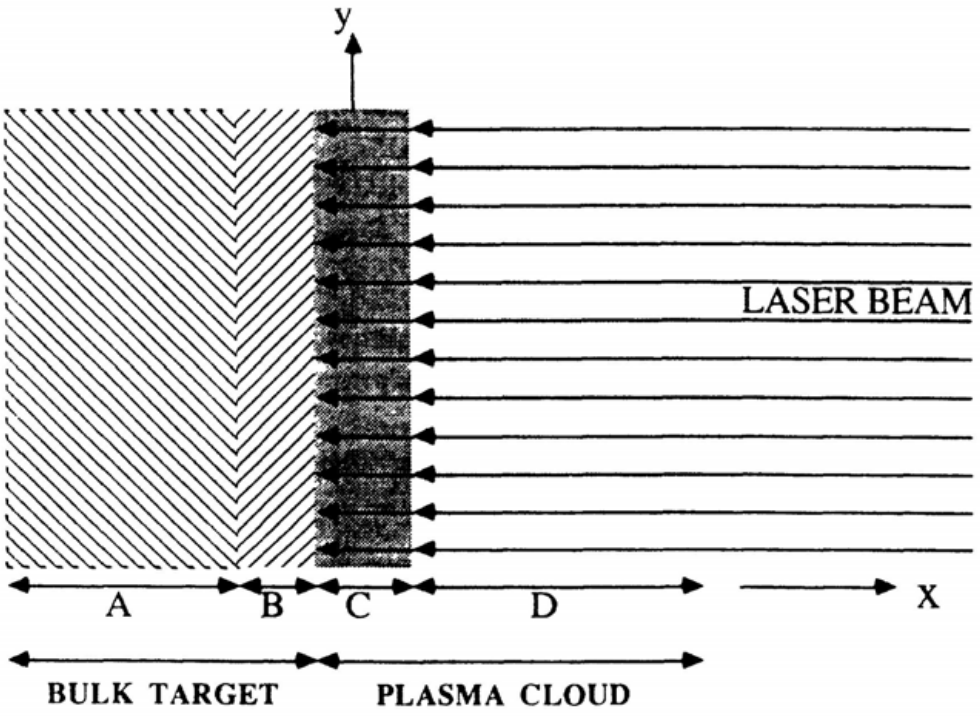

Figure 2. 3 Schematic diagram shows the different phases presented during the laser target interaction.

After the plasma formation and isothermal expansion, the adiabatic expansion of the plasma in vacuum chamber gives rise to the laser deposition process. In this regime, the thermal energy is converted to kinetic energy to increase the velocity of the plasma. The last stage of PLD is the deposition of ablated materials onto the substrate. The ejected species by laser-target interaction always have high energy and may cause sputtering of the substrate surface atoms and collision between the incident flux flow and the sputtered atoms. When the condensation rate is higher than that of the flux, a thermal equilibrium condition can be reached for the film growth on the substrate. [138]

For multi-element materials PLD has an obvious advantage for easily obtaining the desired film stoichiometry. So in these series of complex composition material film growth PLD was used as deposition method. Pulsed-laser deposition (PLD) has drawn much attention in the past few decades for its ease of use and success in depositing materials of complex stoichiometry. Iron chalcogenide superconductor thin film was first successfully deposited by PLD.

In this series of research, high purity commercial powders of Fe, Se and Te (99.99%) from Alfa Aesar (Ward hill, MA, USA) were used for target synthesis. The $FeSe_xTe_{1-x}$ targets were prepared by a standard solid-state reaction method with appropriate stoichiometric mixture of the Fe, Se and Te powders. Target powders mixed according to the molar ratio were grounded, well mixed by ball milling machine and pressed into pellets. The pressed pellets were sealed in glass ampule with argon gas and sintered various temperatures in vacuum furnace to form dense targets. All samples were deposited on $SrTiO_3$ (STO) (001), MgO (001) single crystal substrates and amorphous glass substrate (Microscope Slide, Thermofisher).

The thickness of iron chalcogenide thin film was controlled for each project. The interlayer was inserted into the thin film by alternative laser ablation of the corresponding targets. In this research the epitaxial film on the single crystal substrate with out of plane and in plane alignment is the ultimate goal.

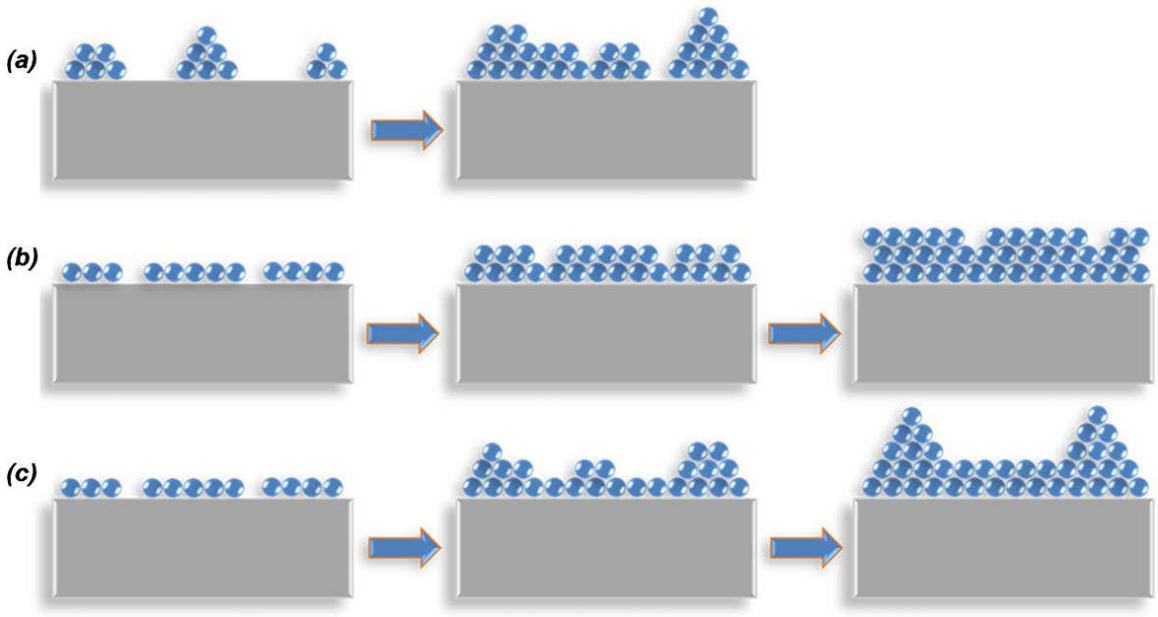

Figure 2. 4 Illustration of three heteroepitaxial growth modes including Volmer-Weber Island growth, Frank-Van Merwe layer-by-layer and Stranski-Krastanov layer + island growth. [139]

Depend on the growth parameter and the intrinsic properties of the substrate and the thin film, three major thin films growth modes (1) Volmer-Weber island growth, (2) Frank-Van der Merwe or layer-by-layer growth, and (3) Stranski-Krastanov layer + island growth are illustrated in Figure 2. 4. In the first island growth mode, adatoms and molecules nucleate on substrate to form clusters to grow into 3-D islands because of stronger bonding between deposited atoms compared with the bonding between adatom and the substrate. In the second layer-by-layer growth mode, adatoms tend to form small nuclear site to grow into 2-D planar structure because they are more strongly bonded to the substrate than to each other. In the Stranski-Krastanov growth mode, it is a combination of both the layer-by-layer and island growth. [140] In this mode, Volmer-Weber island growth will begin after forming one or several atomic monolayers in a

layer-by-layer growth due to the energetically instability during the film growth. From macroscopic aspect the bonding energy difference can also be illustrated by the surface energy. So the growth modes of single phase epitaxial thin films can be also described by the thermodynamic models for nucleation process. Figure 2. 5 illustrates a model that describes the surface nucleation process. [139] The equilibrium among the horizontal components of the interfacial tensions between substrate, film and vapor phases yields the following equation:

$$r_{sv} = r_{fs} + r_{fv}\, cos\theta \quad \text{(Equation 2. 3)}$$

where r is the interfacial energy and θ is the wetting angle. The subscripts *s*, *f*, and *v* represent substrate, film and vapor respectively.

Three growth modes can be identified by this equation according to the wetting angle. In the 3D growth case, $\theta > 0$ when the surface tension is higher than that of the substrate. In layer-by-layer growth, the surface energy of film and substrate are similar and the film wets the substrate with $\theta \sim 0$. However it is an ideal model, in practice there are different kinds of nucleation sites including step edges, defects etc. during the thin film growth and the growth of nucleus can also be disrupted after the critical nucleus size be reached. In the PLD process, the thin film growth is also controlled by the growth dynamic which is influenced by the growth parameter such as the growth temperature, laser energy and repetition rate of the laser. That is also the principle how we optimize the thin film growth.

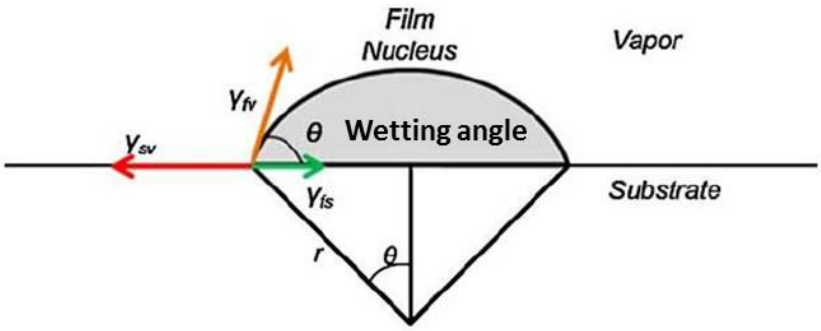

Figure 2. 5 Schematic diagram of the atomistic nucleation process during a vapor deposition process. [139]

2.2 Thin film microstructure and crystalline characterizations

After the deposition, many film characterizations need to be done for the property analysis. XRD can help detect the crystal structure quickly. Using SEM we can scan the surface morphology. With TEM and STEM we can analysis the thin film phase, composition, microstructure of the interface and the secondary phase as well as crystallinity. EDX is always combined with SEM or TEM, it can do phase and composition analysis also.

2.2.1 X-ray Diffraction (XRD)

X-ray diffraction (XRD) is widely used to explore the composition and crystal structure and measure the size, shape and internal stress of crystalline materials. The incident X-ray beam to a crystal structure will be diffracted into specific directions. According to the angles and the intensities, a three dimensional crystal structure can be mapped. Bragg's Law is the fundamental equation to govern the X-ray diffraction:

$$n\lambda = 2d \sin\theta \quad \text{(Equation 2. 4)}$$

where λ is the wavelength of X-rays, d is the lattice plane spacing, θ is the diffraction angle as shown in Figure 2. 6 [141].

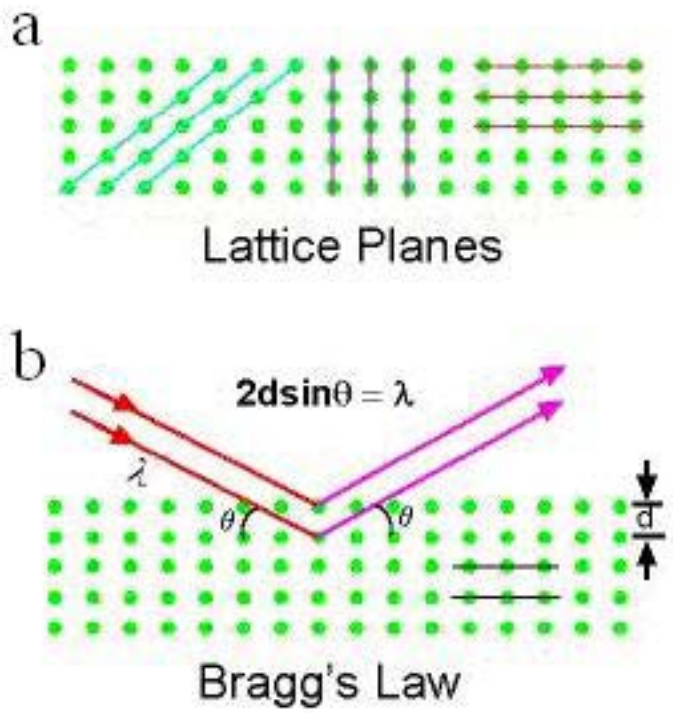

Figure 2. 6 (a) A two dimensional periodic array of atoms that forms different planes in the crystal, (b) diffraction for a set of planes with inter-plane distance d which is conditioned to Bragg's Law.

Only for the combination of certain θ angles theta and d-spacings, the Bragg's Law conditions can be satisfied. Plotting the 2θ and intensities of the resultant diffracted peaks of radiation produces a plot, which is characteristic θ-2θ scan. Besides the θ angles, there are other setup with different measurement configuration for the thin film diffraction as show in the following Figure 2. 7.

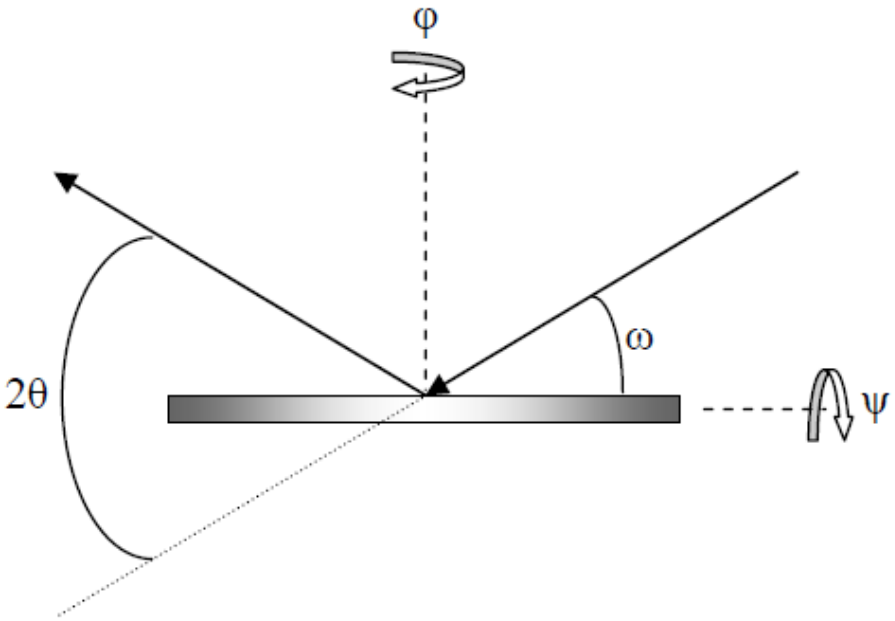

Figure 2. 7 Configuration of the sample stage for the XRD measurement.
ω – angle between incident x-rays and sample surface
2θ – angle between incident x-rays and detector
ψ – sample tilt
φ – in-plane sample rotation
x,y – in-plane displacement of sample
z – vertical displacement of sample

The θ-2θ scan is the characteristic XRD pattern for each material with ω and θ changing simultaneously to record the intensity information corresponding to the θ or 2θ.

The rocking curve is usually used to determine the *c*-axis lattice constant spread. Here the ω is fixed and the reflected angle is varied and the intensity of the corresponding reflected angle is recorded. The Full width at half maximum (FWHM) of the main peak indicates the degree of preferred orientation for thin films.

The φ scan can be performed to study the in-plane texture of the films. Usually the strongest peaks other than the (*00l*) peaks are selected to set up the ψ and ω, and the thin film sample rotates in plane to get the intensities for the corresponding φ. The FWHM of the peaks suggest the in plane alignment of the crystal structure for the thin films. The pole figure is combination of the φ scans at different ψ angles in Polar coordinate.

2.2.2 Scanning Electron Microscope (SEM)

The scanning electron microscope (SEM) uses the interaction between focused high energy electrons beam and the surface of solid specimens which generates various signals as show in the Figure 2. 8. The signals containing secondary electrons (SE), backscattered electrons (BSE), and diffracted backscattered electrons (EBSD), characteristic X-rays, visible light (cathodoluminescence), auger electrons and heat reveal the chemical composition, surface morphology and crystalline structure of the sample. Among them, SE showing morphology and topography and BSE showing composition contrasts in multiphase samples are used to generate images. Characteristic X-rays are unique for each element so it is used to identify the elements in the sample using the EDS. Figure 2. 9 shows schematic diagram of a SEM equipment.

In this dissertation, SEM works have been conducted to characterize the morphology, crystallography of the superconductor thin films with Quanta 600 FEG analytical microscope (200 V to 30 KV, Field emission gun assembly with Schottky emitter source) and JEOL JSM-7500F (100 V to 3 kV, Cold cathode UHV field emission conical anode gun).

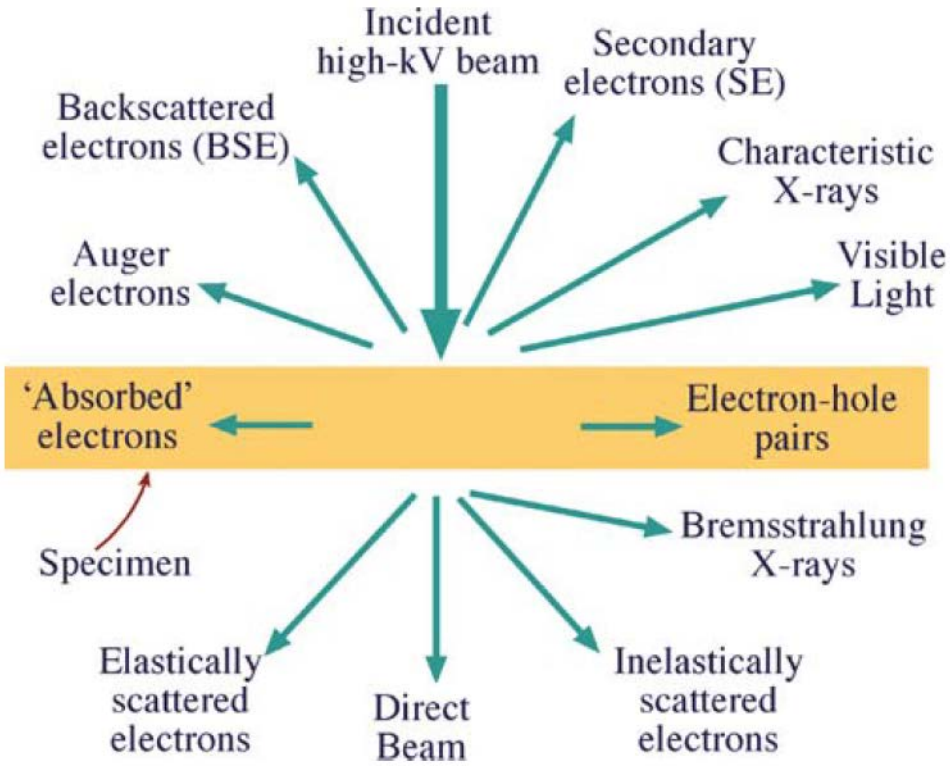

Figure 2. 8 Different kinds of electron scattering from a thin specimen in both the forward and back directions. [142]

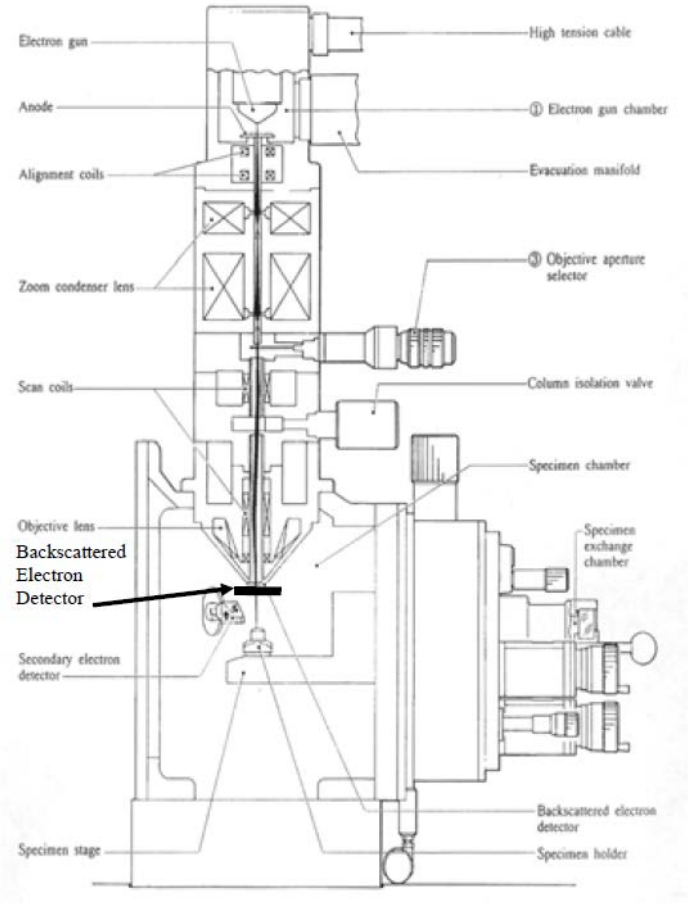

Figure 2. 9 Schematic diagram of SEM equipment.

2.2.3 Transmission Electron Microscopy (TEM)

Transmission electron microscopy (TEM) is a powerful tool for structure characterization. TEMs were developed to overcome the limitation of optical microscopes depending on the wavelength of visible light. In this dissertation, extensive TEM works have been conducted to characterize the morphology and crystallography of the superconductor thin films with JEOL 2010 analytical microscope (200 KV, LaB_6 filament with 0.23 nm point resolution) and FEI Tecnai F20 analytical microscope (200

KV, ZrO_2/W Schottky field emitter with 0.27 Å point resolution, Z-contrast dark-field STEM imaging using the HAADF detector).

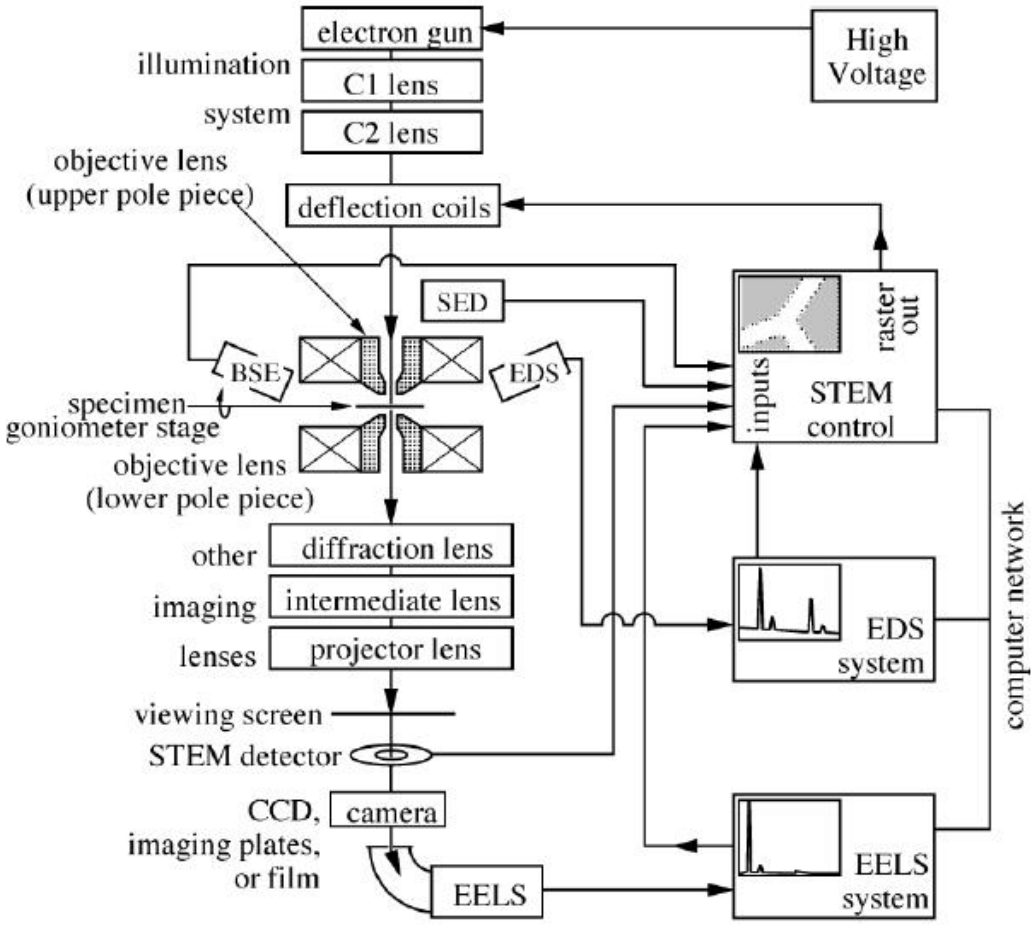

Figure 2. 10 The block diagram of a typical TEM system with analytical capabilities.

As shown in Figure 2. 10, a typical TEM system contains four parts: the electron source, electromagnetic lens system, sample stage and imaging systems, which all combined in a vacuum column backed up by the mechanical pump and turbo pump or diffusion pump. [143] The cathode emits electrons when heated or by high voltage. The electron beam is then accelerated towards the anode by the positive voltage. Then the

electron beam is focused and confined by the condenser lens and apertures. Another set of lens focus the transmitted beam after passing through the specimen and project the enlarged image on the phosphorescent screen.

The resolution and magnification are closely related to each other in TEM. Magnification calculated as the product of the magnifying powers for all the lenses refers to the degree of enlargement of the final image compared to the original object. The maximum resolution defined as the closest spacing of two points which can be distinguished under the microscope based on Rayleigh criterion:

$$r = \frac{0.612\lambda}{n\,(sin\,\alpha)}$$ (Equation 2. 5)

where λ is the wavelength of the electrons, α is the aperture angle of lens and n is refractive index.

There are two basic operation modes in the TEM: the diffraction mode and imaging mode as shown in Figure 2. 11. These two modes can be easily switched by changing the focal length of the intermediate lens depending on whether the image plane coincides with the back focal plane or the image plane of the objective lens. In the imaging mode, objective apertures are inserted at the back focal plane of the objective lens to increase the contrast of the images. Dark field (DF) or bright field (BF) images can be obtained depending on the objective aperture configuration and the beam diffraction as shown in Figure 2. 12. BF image is formed when the aperture is positioned to allow only the transmitted electrons to pass, while DF image is formed when the aperture is positioned to allow only some diffracted electrons to pass and there are two methods to obtain the DF image.

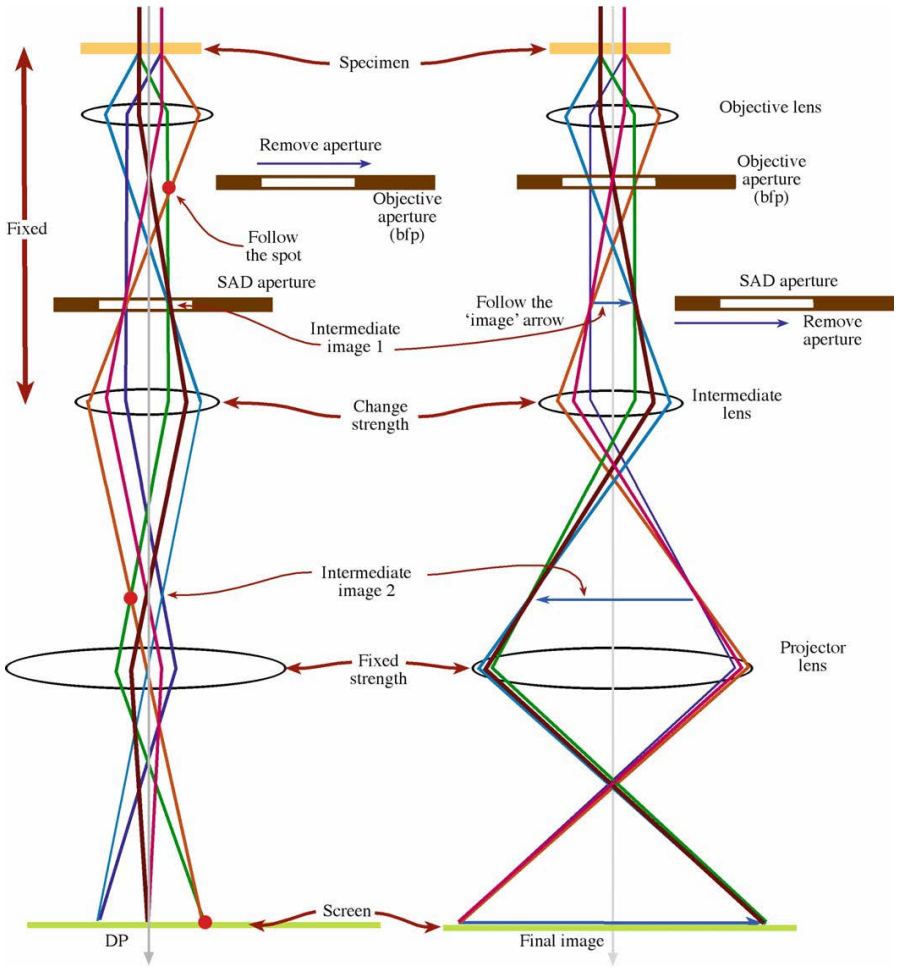

Figure 2. 11 Two basic operation modes of TEM system: (a) the diffraction mode and (b) the imaging mode.[142]

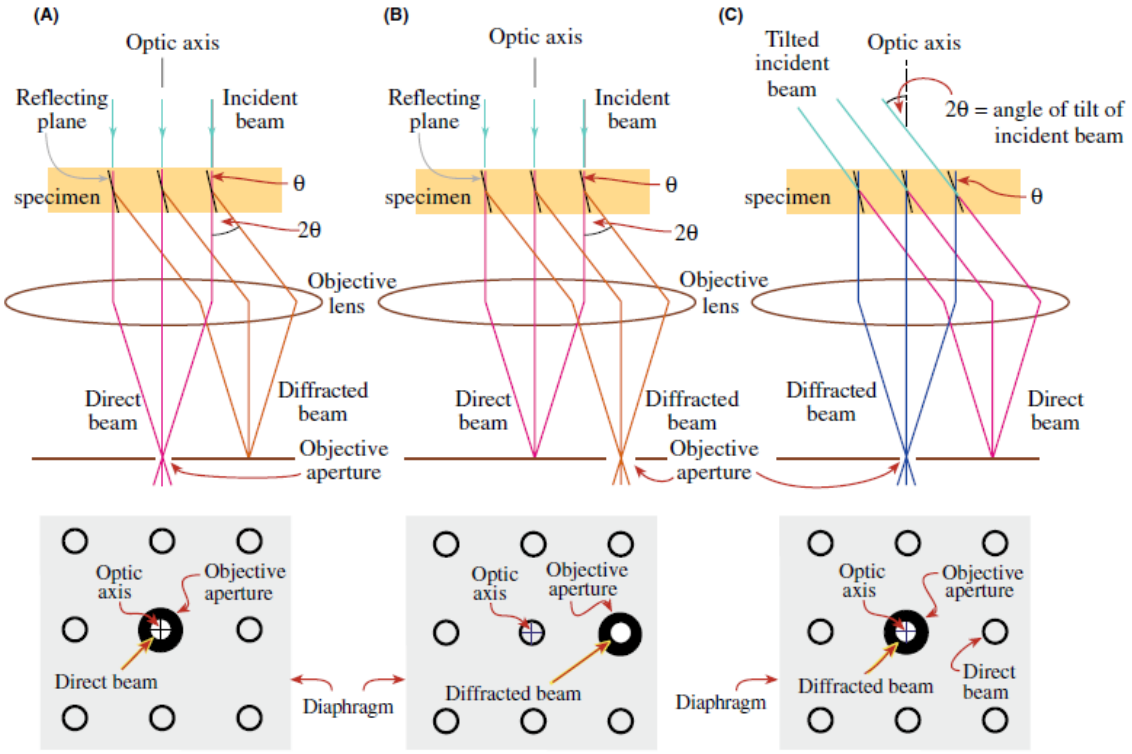

Figure 2. 12 Diagrams of the objective lens and objective aperture combination to produce (A) a BF image formed from the direct electron beam, (B) a displaced-aperture DF image formed with a specific off-axis scattered beam, and (C) a CDF image where the incident beam is tilted so that the scattered beam emerges on the optic axis. [142]

High resolution TEM is an imaging mode in the atomic scale allowing the imaging of the crystallographic structure for semiconductors, metals and complex oxides. In the HRTEM mode, the objective lens should be adjusted to get the shortest focal length and higher accelerating voltages should be used for higher resolution. Chromatic aberration and spherical aberration correction with special lenses and small condenser lens apertures shall be considered to get more coherent beam. In addition small objective aperture may be used to enhance the contrast but at price of resolution. A

thin Specimen without too much ion damage is critical to enhance the resolution capability.

The scanning transmission electron microscope (STEM) is one of the working modes of TEM where the beam scans parallel to the optic axis. By the interaction between the beam and sample it will generate multiple signals which can be collected for mapping such as energy dispersive X-ray (EDX) spectroscopy, electron energy loss spectroscopy (EELS) and annular dark-field imaging (ADF). These signals can be obtained simultaneously, which allows direct correlation of morphology and quantitative data. By using a STEM and a high-angle detector, image where the contrast is directly related to the atomic number (Z-contrast image) can be obtained, which is used in this dissertation to get the composition information.

The TEM specimen preparation is critical for the high quality images and an electron transparent thin region less than 100nm in the sample is preferred. The preparation method depends on the material properties and objective. In this dissertation, both the cross-section and plan-view samples were prepared to study the interphase, secondary phase, film orientation and grain alignment. By conventional method, the thin films specimen can be obtained with the following steps: (1) cutting thin slice from the substrate with thin film; (2) glue two slices together and pre-thinning on sand paper and diamond paper (3) final grinding and polishing; (4) ion milling. Ion-milling is a powerful tool to get an area surrounding the ion milling hole with a thickness less than 100nm and a shorter ion milling duration is preferred to reduce the ion damages. Depends on the

materials, types of TEM samples and initial surface topology, various factors can be adjusted including ion energy, angle of incidence, ion orientation and beam energy.

2.3 Transport and Magnetism Properties Measurement

Superconductor thin films magnetization and transport properties in this dissertation were measured by a Physics Property Measurement System (PPMS) (EverCool, Quantum Design, Inc) with a vibrating sample magnetometer (VSM) head. The PPMS provides a flexible, automated workstation that can perform a variety of experiments with precise thermal control including magnetization and transport resistivity vs. temperature measurements (R-T). The PPMS has a capacity to apply magnetic fields up to -9 T ~ 9 T and a temperature range of 1.9 ~ 400 K using liquid He and heater. The temperature sweep rate ranges from 0.01 K/min to 12K/min. Superior temperature controlling within ±2 mK during measurements is achieved in this system.

The DC transport measurement option in PPMS incorporates a high precision current source and a high precision voltmeter in the Model 6000 control unit. The R-T option supports four-terminal probe measurements. Measurements are typically made by passing a known current through the sample using two leads and measuring the voltage difference across the sample direction using another two leads and the sample resistivity is calculated according Ohm's law and the sample dimension.

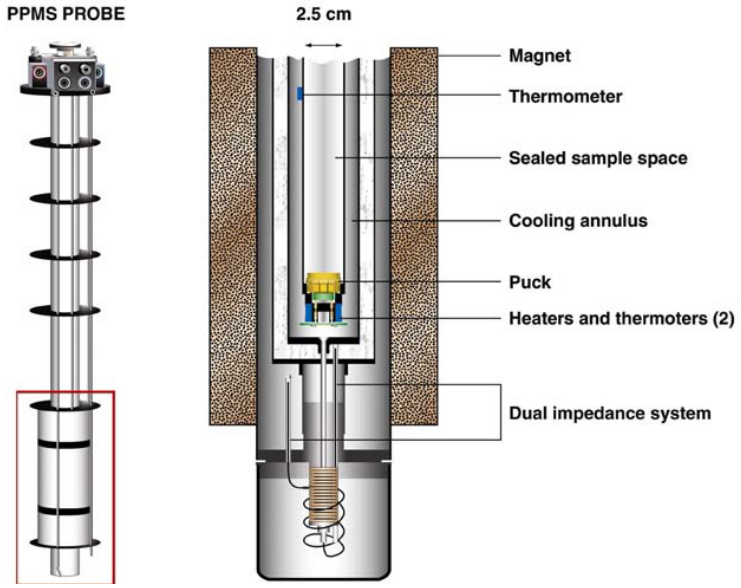

Figure 2. 13 Schematics of the sample rod and puck setup in the dewar of the PPMS.

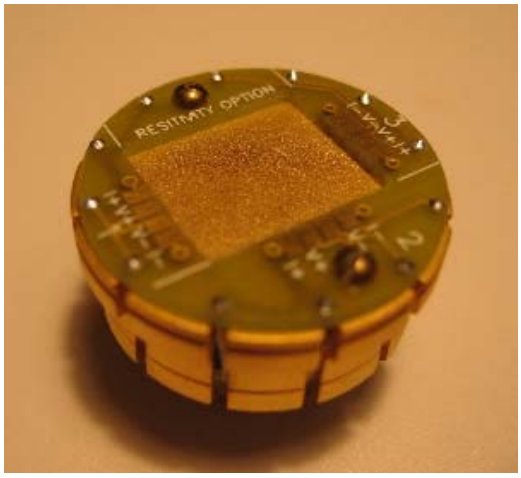

Figure 2. 14 Standard DC Resistivity puck with three channels

Figure 2. 13 shows the sample rod used for transport properties measurements in PPMS. The sample is mounted on easily removable printed circuit boards as show in Figure 2. 14. This DC Resistivity Standard puck has three channels which can measure up to three samples in four point probe arrangement at one time.

For the superconductor with the DC puck, the Resistivity vs. Temperature (R-T) plot can be measured under magnetic field from 0 to 9 T. The critical transition temperature and the upper critical field can be estimated from the measurement result. In addition Current vs. Voltage (I-V) curve can be measured to extract the critical current density of the superconductor at low temperature by preset criterion.

The VSM module with linear motor to vibrate the sample in PPMS is a fast and sensitive DC magnetometer. The measurement is accomplished by oscillating the sample under applied magnetic field or self-field near a detection coil and synchronously detecting the voltage induced by the magnetic response in the sample.

With the VSM head the magnetization of the superconductor under weak magnetic field can be measured. From the zero field cooling (ZFC) and field cooling (FC), the superconducting transition temperature can be measured and for the bulk materials the superconducting volume can be estimated by the susceptibility measurement according to the perfect diamagnetism of the superconductor. The magnetic hysteresis loops are measured to extract the critical current density according to the self-circulated current inside each domain of the superconducting material using the Bean model:

$$J_c = 20\Delta M/[2(1 - w/3l)] \text{ (Equation 2. 6)}$$

where w and l is the width and length of the film and M is the magnetic moment and ΔM is the moment difference between up and down branches in the magnetic hysteresis loop.

CHAPTER III

ENHANCED SUPERCONDUCTING PROPERTIES IN EPITAXIAL FESE THIN FILMS WITH SELF–ASSEMBLED FE_3O_4 NANOPARTICLES*

3.1 Overview

Epitaxial tetragonal iron selenide thin films were grown on single crystal $SrTiO_3$ (STO) (001) and MgO (001) substrates by a pulsed laser deposition (PLD) technique. Deposition temperature and annealing process were found to be critical for achieving the tetragonal phase and the optimum superconducting properties of the films. The critical transition temperature of the thin films ranges from 2 K to 11.5 K depending on the deposition temperature and annealing condition. The samples with higher critical transition temperatures show self-assembled Fe_3O_4 nanoparticles (~15 nm in average particle size) in the films according to both X-ray diffraction (XRD) and transmission electron microscopy (TEM) analysis. Besides the better crystallinity in the films achieved at higher deposition temperatures or through post-annealing, the formation of Fe_3O_4 nanoparticles could assist the formation of the tetragonal FeSe phase and thus lead to the enhanced superconducting properties.

3.2 Introduction

Ever since the discovery of the iron-based superconductor of $LaFeAsO_{1-x}F_x$ [21] with similar layered structure as cuprates, the new group of superconductors has attracted much research attention in exploring its superconducting mechanism, which could guide the exploration of the room temperature superconductor with comparison of the most studied cuprates since 1987 [8] . The discovery of the simplest iron-based superconductor iron selenide with a transition temperature T_c around 8 K [25] arouses much research interest. The superconducting FeSe has the tetragonal PbO structure containing Fe-Se planar sub-lattice with an interval of 5.518 Å. This layered structure is equivalent to the layered FeAs structure in previously found iron pnictide superconductors. FeSe provides a simple system to study the iron-based superconductors in comparison with cuprates [38]. The material contains identical Fe-Se layers similar to the layered structure in cuprates which is believed to be responsible for the superconductivity [39]. Since then, the effects of stoichiometry [40-42], structure variation [31, 43, 44], strain and stress [45], pressure [28, 31, 46] and doping [27, 47] on its superconducting properties have been explored for FeSe.

Besides the bulk FeSe that has been explored extensively [25, 27, 43, 46, 53] , the epitaxial FeSe thin films have recently attracted great research interests [45, 54, 55]. Most of the FeSe films reported were deposited by pulsed laser deposition (PLD). Compared with its bulk counterpart, FeSe thin film has a great potential in developing the ordered quasi-2D structure and is suitable for coating technology which has already been applied in $YBa_2Cu_3O_{7-x}$ coated conductors [56]. In the previous FeSe thin film

work, it was reported that the film thickness and orientation [54] as well as film stoichiometry and deposition temperature are critical factors for the superconducting properties [42, 55, 57] of FeSe thin film. Wang *et al.* reported the optimum deposition temperature for FeSe films on MgO is 500°C. The T_c^{onset} and T_c^{zero} are 10 K and 4K respectively with the film thickness of 140 nm. However the film is not in the *c*-axis orientation [54]. Nie *et al.* reported that the optimum deposition temperature of FeSe films with *c*-axis orientation on different substrates is 380°C. The T_c^{onset} of the films is lower than 10 K on $SrTiO_3$ (STO) (001) and MgO (001). The upper critical field H_{c2} of the film was estimated to be 35 T with linear extrapolation method. It was also reported that the tensile strain in *a*-*b* plane suppresses the superconductivity [45]. Han *et al.* reported single-phased, *c*-axis oriented epitaxial $FeSe_{0.88}$ films on STO (001), (La, Sr)(Al, Ta)O_3 (001) and $LaAlO_3$ (001) with the T_c^{onset} of 11.8 K and the T_c^{zero} of 3.4 K [55]. Based on the previous studies, it is evident that the optimum growth temperatures, the film compositions and the resulted superconducting properties are largely varied. There is not yet a solid explanation for the variation of the superconducting properties of FeSe films based on the deposition conditions. The properties of FeSe films also need to be further optimized for the study on dopants incorporation.

In this report, we focus on the optimization of pure FeSe thin films with different growth conditions using PLD and post-annealing procedures. The microstructure properties of the films including the epitaxial quality, interface structure and secondary phase have been studied and correlated with the superconducting properties.

3.3 Experimental

The FeSe thin films were deposited on single crystal MgO (001) and STO (001) substrates in a PLD system with a KrF excimer laser (Lambda Physik Compex Pro 205, λ=248nm). The laser power density was varied from 3 J/cm^2 to 5 J/cm^2 by adjusting the laser output energy. The base pressure for all the depositions was ~ 10^{-6} Torr. The FeSe targets were made by pressing pure FeSe powder and followed by vacuum sintering at various temperatures. The deposition temperature was varied from 400°C to 550°C. Post-annealing was applied with annealing temperature of 500°C in the vacuum chamber with a base pressure of ~ 10^{-6} Torr to explore the effects of processing parameters on the superconducting properties. The film thickness was kept around 150 nm for all the samples.

The microstructure of the films was characterized by X-ray diffraction (XRD) (BRUKER D8 powder X-ray diffractometer), scanning electron microscope (SEM) (JEOL JSM-7500F with a field emission gun) and transmission electron microscope (TEM) (JEOL-2010 with a point-to-point resolution of 2.34 Å). The superconducting properties were characterized using resistivity-temperature (R-T) measurement from 2K-300K under applied magnetic field (0 -7 T) in a physical property measurement system (PPMS, Quantum Design).

3.4 Results and Discussion

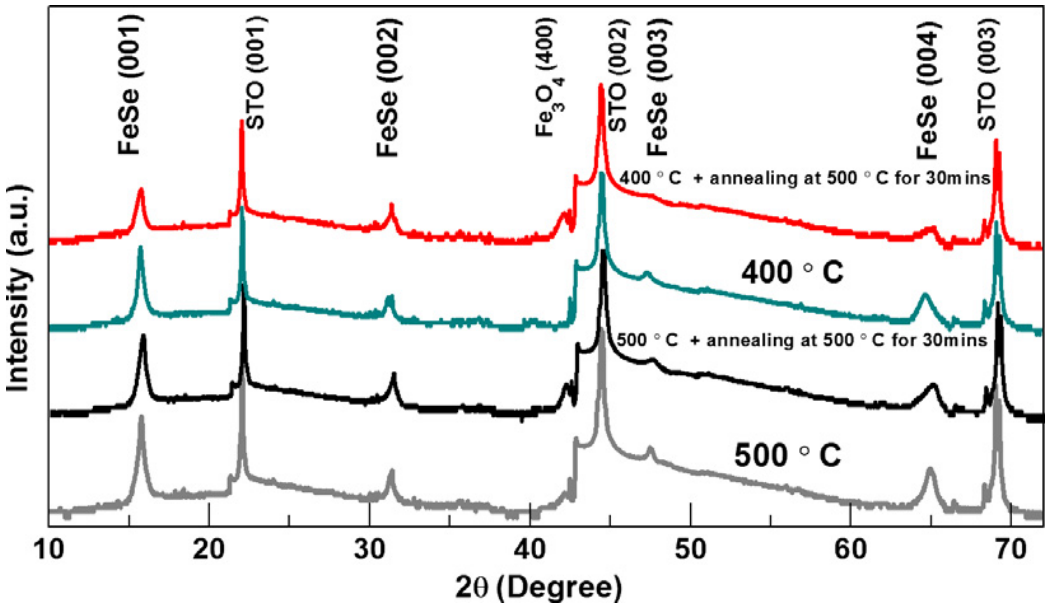

Figure 3. 1 XRD patterns of the FeSe thin films on STO deposited at 400 °C and 500 °C compared with the patterns for the samples after annealing at 500 °C.

A standard θ-2θ XRD analysis was performed for all the films deposited on MgO and STO substrates. Figure 3. 1 shows the θ-2θ XRD scans for the FeSe films deposited on STO substrates at 400°C and 500°C. It is clear that both films have grown highly textured along (00*l*) on STO (001). Based on the lattice parameter calculated from the out-of-plane *d*-spacings, the FeSe thin films are determined to be tetragonal phase with an out-of-plane lattice parameter of 5.515 Å for the film deposited at 400°C and 5.505 Å for the film deposited at 500°C. In both cases the out-of-plane lattice parameter is slightly smaller than that of the bulk value (5.518 Å). Different from the sample deposited at 400°C, the sample deposited at 500°C has a small amount of Fe_3O_4 formed indicated by the obvious Fe_3O_4 (400) peak in the XRD profile. Samples deposited at

higher temperature start to show hexagonal FeSe (101) peak in the XRD profile. The as-deposited samples were then annealed at 500°C for 30 minutes. The XRD θ-2θ scans are plotted along with the samples without annealing as comparison in Figure 3. 1. Obviously, both of the annealed samples show a preferred (00*l*) orientation on STO (001) similar to the as-deposited films. It is interesting that the Fe_3O_4 (400) peak starts to show up in the 400°C deposited sample after annealing and the peak gets stronger for the 500°C sample after annealing compared with the as-deposited sample indicated by the XRD profile. This suggests that annealing introduces a small amount of Fe_3O_4 in the 400°C deposited sample and additional Fe_3O_4 phase in the 500°C deposited sample. It is also noted that the FeSe peaks shift to higher angles after annealing along with the appearance of Fe_3O_4, i.e., the *c*-axis lattice parameter of FeSe shrinks from 5.515 Å to 5.487 Å for film deposited at 400°C and from 5.505 Å to 5.491 Å for the film deposited at 500°C. A similar *c*-axis lattice parameter reduction was reported in $SrFe_2As_2$ previously [144].

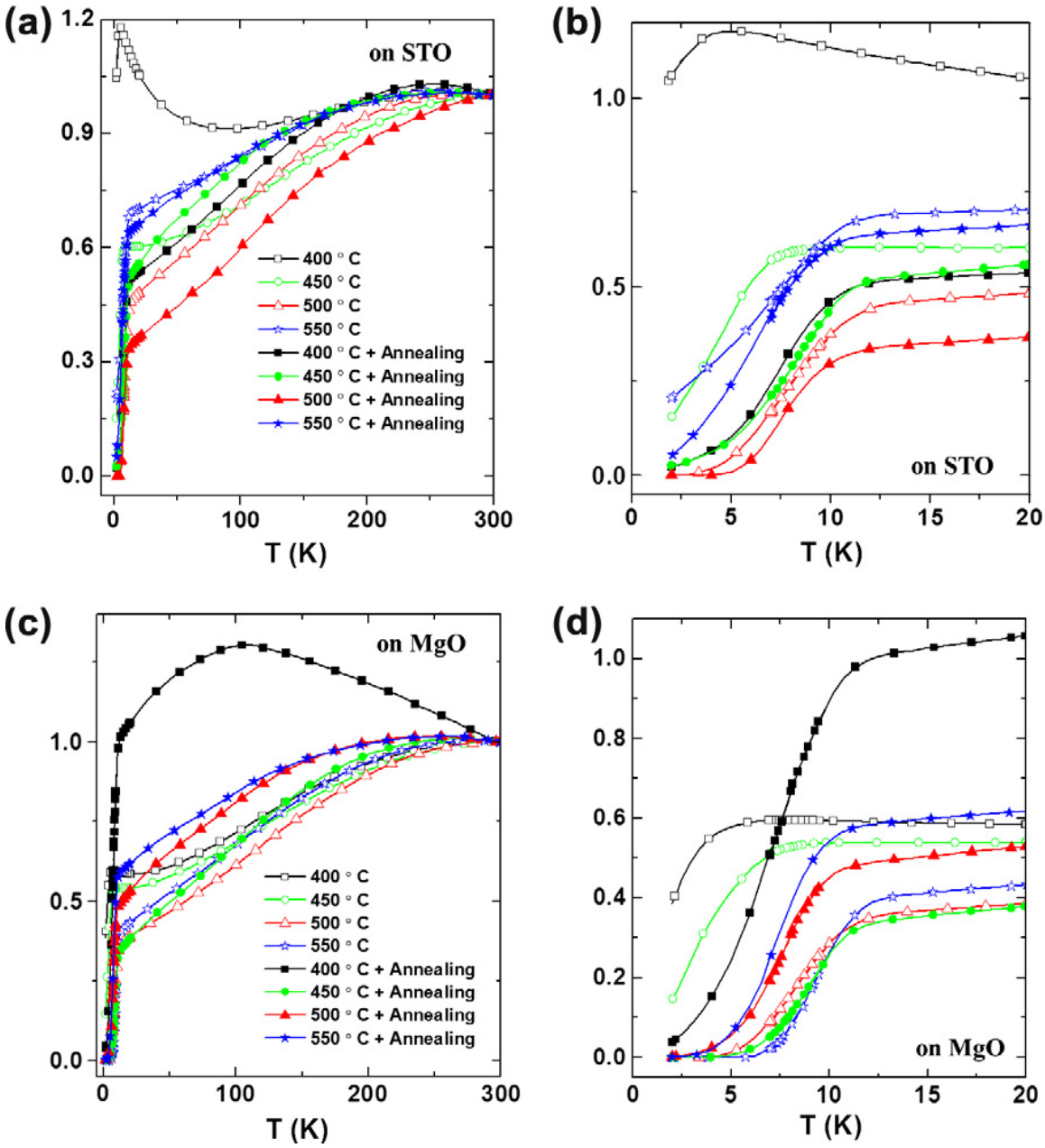

Figure 3. 2 Normalized R–T plots of FeSe thin film samples on (a) STO and (c) MgO substrates with different deposition temperatures and annealing conditions. (b) and (d) show the details from 2 K to 20 K for (a) and (b) respectively.

R-T measurements (2 K-300 K) were conducted for all the samples on STO and MgO by a four-point probe method and plotted in Figure 3. 2 (a) and (c), respectively. The details of the transition region 2K ~ 20K were enlarged in Figure 3. 2 (b) and (d) for

FeSe films on STO and MgO, respectively. For the 400°C deposited sample, it shows pure FeSe tetragonal phase in the XRD result. However the R-T result shows an upturn before the superconducting transition as the temperature decreases and zero resistance cannot be achieved even at 2 K. Interestingly, after annealing it shows a decent superconducting transition starting at 10 K along with the formation of the Fe_3O_4 phase indicated by XRD profile. All the films deposited at 450°C or higher show an obvious T_c transition. After annealing, along with the formation of Fe_3O_4 phase, the T_c for the films on STO slightly increases with a sharper transition as shown in Figure 3. 2 (b). However the films deposited at higher temperatures on MgO (e.g., 500°C and 550°C) show a slight drop of T_c along with the weakening of the Fe_3O_4 peak indicated by XRD. The highest transition temperature T_c ranges from 6 K (T_c^{zero}) to 11.5 K (T_c^{onset}) for the films on MgO and from 4 K (T_c^{zero}) to 10.8 K (T_c^{onset}) for the films on STO. Based on the T_c measurements, the optimum deposition temperature is determined to be ~ 500°C and 550°C in the tested range for films on STO and MgO substrates, respectively.

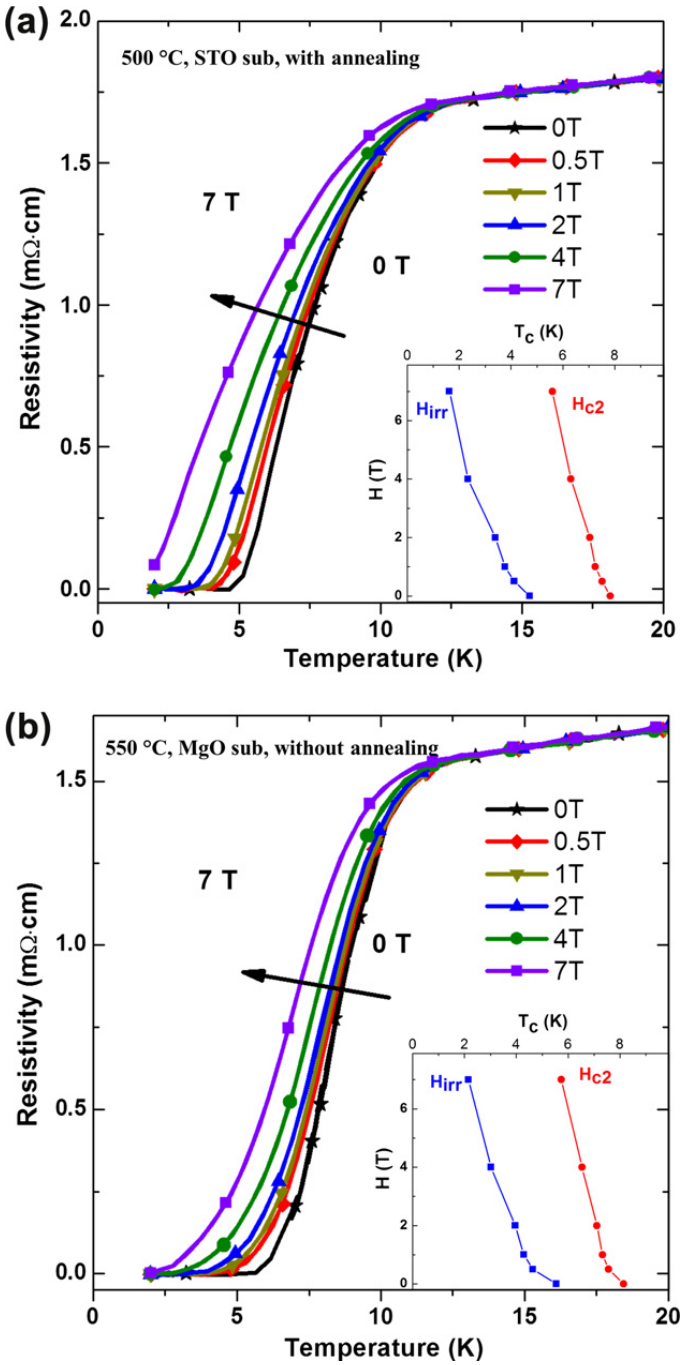

Figure 3. 3 R–T plots of FeSe thin films on (a) STO and (b) MgO under magnetic field (0–7 T) and the insets show irreversibility line $H_{irr}(T)$ and the upper critical field $H_{c2}(T)$.

Magnetic field was then applied during the R-T measurements to estimate the upper critical field. The irreversibility line $H_{irr}(T)$ and the upper critical field $H_{c2}(T)$ are plotted as insets in Figure 3. 3. The upper critical field was estimated by the Werthamer-Helfand-Hohenberg model,

$$-H_{c2}(0)=0.7T_c dH_{c2}/dT|T_c \quad \text{(Equation 3. 1)}$$

using the middle point of the superconducting transition temperature [55, 101]. From Figure 3. 3 the upper critical field H_{c2} is estimated to be ~ 20 T, for both thin films on STO and MgO. The upper critical field of the films is comparable to the previous report of H_{c2} = 14 T [55] and H_{c2} = 25.7 T [101] calculated with the same method.

To further explore the effects of deposition temperature and annealing condition, we conducted a detailed microstructure characterization on the as-deposited samples and the samples after annealing. Figure 3. 4 (a) and (b) show the SEM images for the surface of the samples deposited at 550°C and 450°C, respectively. Figure 3. 4 (c) shows the surface of the 450°C sample after annealing. It is evident that the 550°C deposited film has an obvious grain structure on the surface. The grains are well connected with very few clusters on the film surface. Interestingly, the surface morphologies of 4a (550°C sample) and 4c (450°C sample with annealing) are very similar, i.e., the grains are more faceted which indicates a better crystallinity of the films. In Figure 3. 4 (b), the 450°C deposited film shows a lot of round clusters, which suggests the nucleation is not yet complete and the grain size in the clusters is relatively small. This result is consistent with R-T measurements where a better superconducting properties were observed in the high temperature deposited sample and the low temperature sample after annealing.

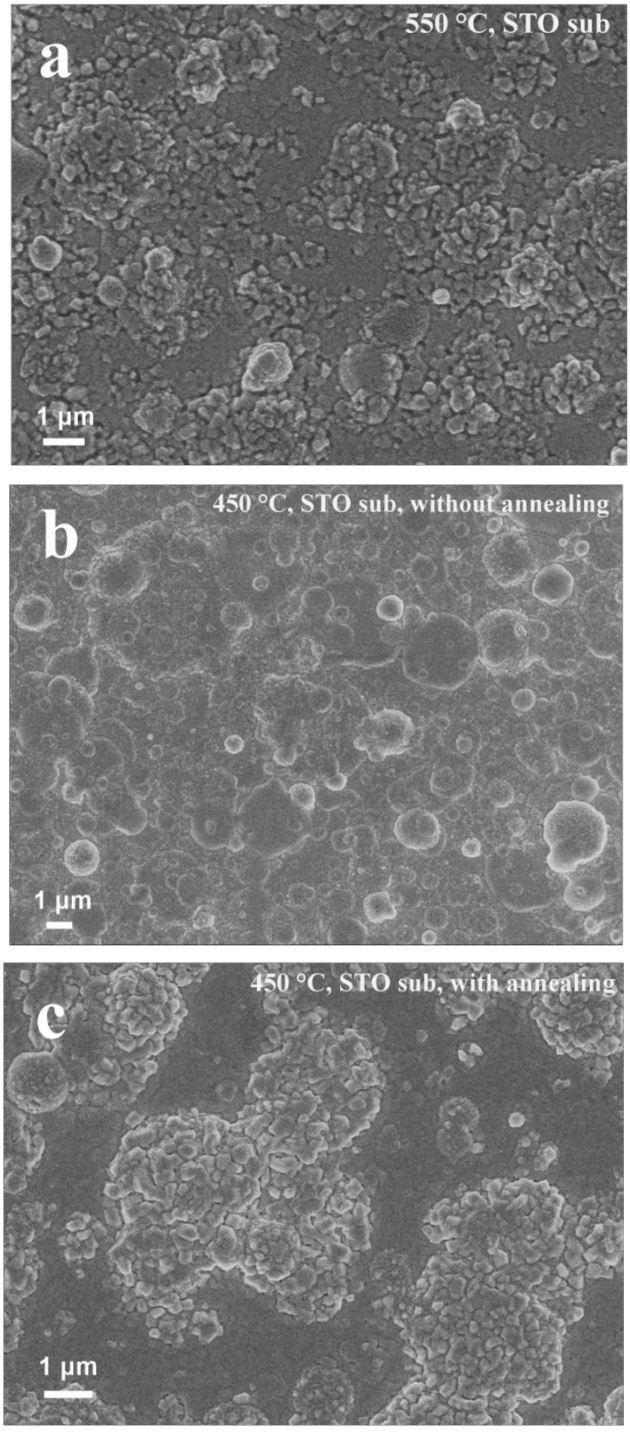

Figure 3. 4 SEM micrographs of FeSe films: (a) deposited at 550 °C, (b) deposited at 450 °C, and (c) deposited at 450 °C followed by annealing at 500 °C for 30 min.

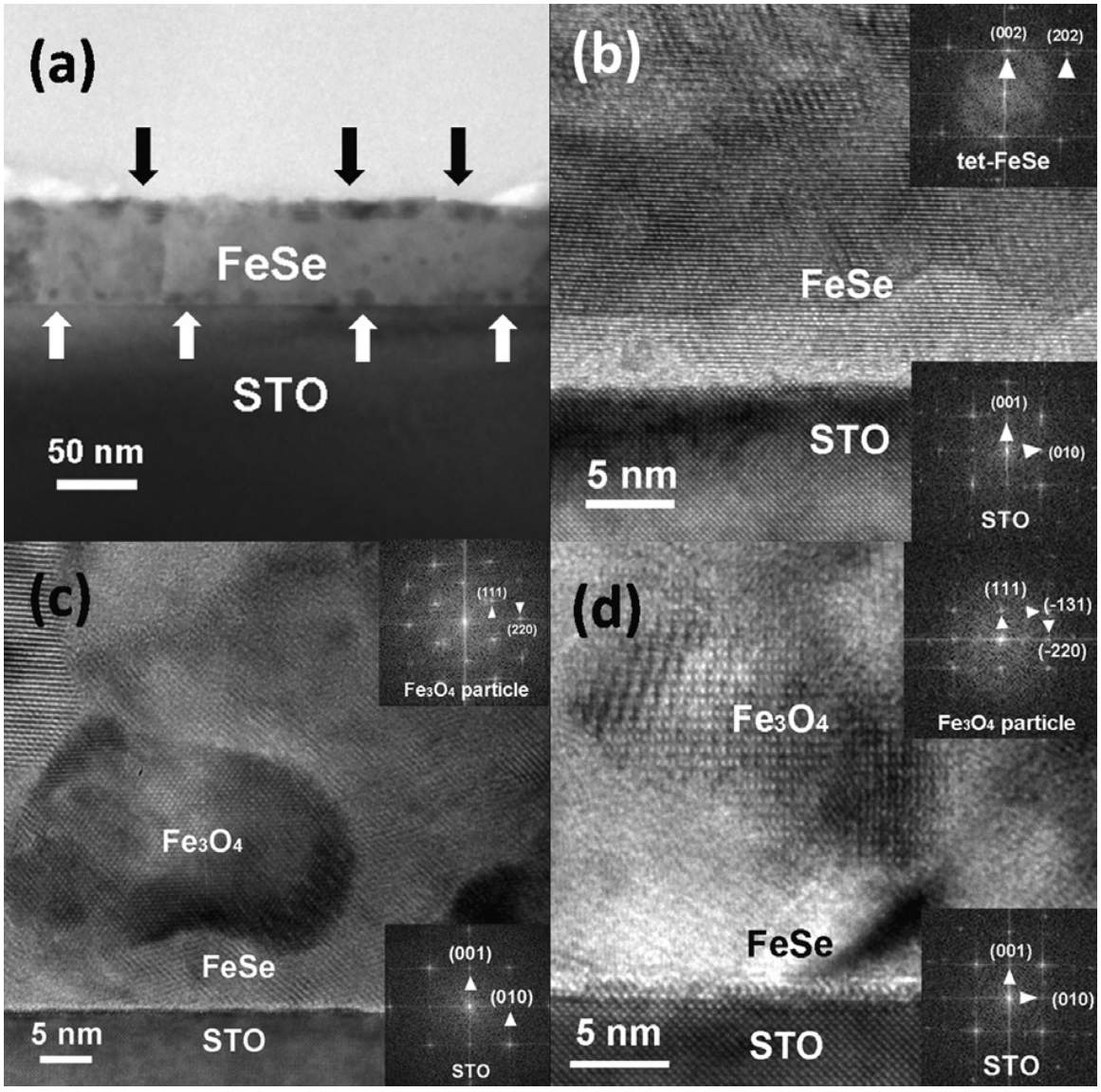

Figure 3. 5 (a) Cross-sectional TEM micrograph of the FeSe film on STO deposited at 500 °C. The black/white arrows indicate the particles at the film surface and the film/substrate interface. (b) Cross-section high resolution TEM micrograph and the corresponding Fast Fourier transform (FFT) of epitaxial FeSe film on STO. (c) and (d) are Cross-section high resolution TEM micrographs of the FeSe film with Fe_3O_4 particle and corresponding FFT of Fe_3O_4 nanoparticle.

Besides the differences in the film crystallinity and the surface morphology due to the different processing conditions, Fe_3O_4 formation is another feature that is strongly

correlated with the superconducting properties. A detailed cross-sectional TEM and high resolution TEM (HRTEM) study was conducted to explore the microstructure of the FeSe films as well as the secondary phase Fe_3O_4. Figure 3. 5 (a) shows the cross-sectional TEM image of FeSe film deposited on STO at 500°C. The film thickness is ~ 150 nm. There are obvious nanoparticles embedded in both the top surface and the film/substrate interface regions (marked by arrows). The average size of the particles is ~ 15 nm. To confirm the quality of the film and the structure of the nanoparticles, we conducted a detailed HRTEM analysis on this sample. In Figure 3. 5 (b) high quality epitaxial FeSe was observed. The corresponding Fast Fourier transformation (FFT) from the film and the substrate area confirms the high epitaxial quality of FeSe on STO. The lattice matching orientations between the film and the substrate are determined to be $(001)_{FeSe}//(001)_{STO}$ and $(100)_{FeSe}//(100)_{STO}$. Detailed HRTEM and the corresponding FFT analysis were conducted on the nanoparticles at the film/substrate interface. Based on the d-spacing calculation from FFT diffraction, it confirms that the nanoparticles are Fe_3O_4. The typical Fe_3O_4 nanoparticle in Figure 3. 5 (c) has matching relations with the FeSe film matrix of $(220)_{Fe3O4}//(010)_{FeSe}$ and $(001)_{Fe3O4}//(001)_{FeSe}$.

The formation of the Fe_3O_4 particles at the film/substrate interface is possibly due to that the excess Fe in the film reacts with the oxygen diffused from the underlying substrate. A similar oxygen diffusion from underlying substrate was reported previously [145]. The Fe_3O_4 nanoparticles on the top surface might form by the reaction of the excess Fe in the film with the residual oxygen in the vacuum chamber during deposition and annealing. The formation of Fe_3O_4 nanoparticles reduces the excess Fe due to the

loss of volatile selenium in the film, and thus results in FeSe films with better superconducting properties.

The stoichiometry issue has been reported for the FeSe bulks [40, 41] and films [42, 55] previously. In bulk FeSe, several reports discussed that the excess Fe exists in the form of Fe_3O_4 and the iron selenide maintains the superconducting composition [40, 41]. In thin films, Se deficiency is more likely to happen due to the vapour pressure difference between Fe and Se during deposition, which causes the Se deficiency in the resulted films. The Fe_3O_4 formation could help to remove the excess Fe in the films. The effect could become even more significant because the surface effect in thin films is a lot stronger than that in bulks. Compared with previous reports on the undoped FeSe systems [45, 54, 55], the films in this work with Fe_3O_4 nanoparticles formed at the interface and surface show better superconducting properties. The best values reported here are T_c^{onset} of 11.5 K and T_c^{zero} of 6 K with an upper critical field H_{c2} ~ 20 T. Even though the mechanism of the enhancement is still under investigation and the film crystallinity is certainly an important factor, the coexistence of the enhanced superconducting properties and the formation of the self-assembled Fe_3O_4 nanoparticles is evident. It is also possible that the self-assembled Fe_3O_4 nanoparticles could act as flux pinning centers for future flux pinning engineering in the FeSe and related coated conductors.

3.5. Conclusions

High quality epitaxial FeSe thin films were deposited on STO and MgO substrates. The optimum deposition temperatures are ~ 500°C and 550°C for samples on

STO and MgO substrates, respectively. In addition, the superconducting property can be further enhanced by the post-annealing procedure at 500°C for 30 minutes which induces secondary phase of Fe_3O_4 particles. HRTEM indicates that the self-assembled Fe_3O_4 particles form at the FeSe film surface and the film/substrate interface. The samples with Fe_3O_4 nanoparticles present better superconducting property with higher transition temperatures (e.g., T_c of the samples on MgO ranges from 6 K to 11.5 K and T_c of the samples on STO is from 4 K to 10.8 K) and sharper transitions. Better crystallinity and surface morphology, and the formation of the Fe_3O_4 particles in the films all contribute to the enhanced superconducting properties in the FeSe thin films.

Based on the previous studies, it is evident that the optimum growth temperatures, the film compositions and the resulted superconducting properties are largely varied. There is not yet a solid explanation for the variation of the superconducting properties of FeSe films based on the deposition conditions. The properties of FeSe films also need to be further optimized for the study on dopants incorporation.

In this proposal, we will focus on the optimization of pure FeSe thin films on STO and MgO substrates with different growth conditions using PLD and post-annealing procedures. The microstructure properties of the films including the epitaxial quality, interface structure and secondary phase will be studied and correlated with the superconducting properties.

The deposition temperature will varied from 400°C to 550°C. Post-annealing will be applied with annealing temperature of 500°C in the vacuum chamber with a base

pressure of ~ 10^{-6} Torr to explore the effects of processing parameters on the superconducting properties.

The preliminary results shows high quality epitaxial FeSe thin films were deposited on STO and MgO substrates. The optimum deposition temperatures are ~ 500°C and 550°C for samples on STO and MgO substrates, respectively. In addition, the superconducting property can be further enhanced by the post-annealing procedure at 500°C for 30 minutes which induces secondary phase of Fe_3O_4 particles. HRTEM indicates that the self-assembled Fe_3O_4 particles form at the FeSe film surface and the film/substrate interface. The samples with Fe_3O_4 nanoparticles present better superconducting property with higher transition temperatures (e.g., T_c of the samples on MgO ranges from 6 K to 11.5 K and T_c of the samples on STO is from 4 K to 10.8 K) and sharper transitions. Better crystallinity and surface morphology, and the formation of the Fe_3O_4 particles in the films all contribute to the enhanced superconducting properties in the FeSe thin films.

CHAPTER IV

ENHANCED FLUX PINNING PROPERTIES IN SUPERCONDUCTING $FESE_{0.5}TE_{0.5}$ THIN FILMS WITH SECONDARY PHASES*

4.1 Overview

In this paper we report epitaxial superconducting $FeSe_{0.5}Te_{0.5}$ thin films grown on single crystal $SrTiO_3$ (STO) (100) substrates by a pulse laser deposition (PLD) technique. The films include a single layer grown in vacuum, a single layer grown in controlled oxygen atmosphere and a tri-layer film with a 7 nm-thick CeO_2 interlayer. All the films show a similar transition temperature T_c ranging from ~12 K (T_c^{onset}) to ~ 10 K (T_c^{zero}) while the CeO_2 nanolayer sample shows a significantly enhanced critical current density under magnetic field. The calculated critical current density of the film with the CeO_2 interlayer is ~10^5 A/cm^2 at 2 K in self-field and 2.8×10^4 A/cm^2 at 7 T at 2 K. The power-law exponent α value of the sample is determined to be as low as 0.21 at 2 K. Microstructural analysis shows both the oxygen grown sample and the sample with CeO_2 nanolayer have uniform nanoclusters in the film matrix. These secondary phases as well as the defects around the interlayer interfaces might be responsible for the enhanced pinning properties.

4.2 Introduction

Since the discovery of the iron selenide (FeSe) superconductor with a transition temperature around 8 K [25], this simple iron-based arsenic-free superconductor has attracted much research interest [27, 28, 40, 41, 46, 48, 60, 146]. The superconducting FeSe has a tetragonal PbO structure containing the Fe-Se planar sub-lattice with an interval of 5.518 Å. FeSe provides a simple system to study the iron-based superconductors in comparison with the cuprates [38]. Following the similar research approaches of the iron pnictide superconductors, high external pressure [28, 46, 48], and, the doping of the chalcogens [41], the transition metals [49, 50] and the alkali metals [51, 52], were applied to enhance the superconducting properties. Although the critical transition temperature (T_c) of the iron-based superconductor is much lower than that of the cuprates, the iron-based superconductor has lower anisotropy which is good for magnets applications [29]. Besides the superconducting transition temperature, critical current density (J_c) is another important factor for future applications. Although compared to the cuprates or even the iron pnictides, the J_c of the iron chalcogenide superconductor is lower, its slow decrease of the J_c with increasing magnetic field as well as its easy composition control makes the iron chalcogenide a promising candidate for high field applications [58, 59].

In the isovalent-doped FeSe, either tellurium or sulfur was used, which is similar to the effect of external pressure to induce structure distortion to the ground state of the superconductivity [60]. The effect of doping concentration was also studied for achieving optimum stoichiometry in iron chalcogenide systems such as $FeSe_{1-x}Te_x$ and

$FeTe_{1-x}S_x$ [41, 61, 62]. T_c up to 21 K in the epitaxial $FeSe_{0.5}Te_{0.5}$ thin films used to be reported [63]. In bulk form, the critical current density of the single crystal $FeSe_{0.4}Te_{0.6}$ was reported to be around 10^5 A/cm^2 at 2 K [58, 59, 64, 65]. Recently enhancing the critical current of the iron chalcogenide thin films has attracted great research interests [66, 67]. Most of the iron chalcogenide films reported were deposited by pulsed laser deposition (PLD). Compared to its bulk counterpart, due to the layered structure the iron chalcogenide thin film has a great potential in developing the ordered quasi-2D structure and it is more practical to apply the coating technology which has already been well developed in $YBa_2Cu_3O_{7-x}$ (YBCO) coated conductors [56]. In cuprates, various pinning centers were used to enhance the critical current density under magnetic field which include the second phase particles [146, 147], dislocation at the interface [131], nanorod array across the film [148] or the combination of them to enhance the magnetic flux pinning properties in all directions [149].

Flux pining centers could also be introduced into the iron-based superconductor to enhance its in-field performance. For example, nanosize columnar defects correlated with oxygen incorporation during film growth were observed in Co-doped $BaFe_2As_2$ as strong vortex pinning centers [150]. In this report, we report our initial attempt on introducing the flux pinning centers in $FeSe_{0.5}Te_{0.5}$ either under a controlled oxygen atmosphere or by depositing the film with a thin CeO_2 interlayer. The CeO_2 interlayer has been previously introduced to overcome the J_c thickness dependence in the YBCO film [151]. The microstructure of the $FeSe_{0.5}Te_{0.5}$ films including the epitaxial quality,

the interface structure and the secondary phase have been studied and correlated with the superconducting properties to explore the pinning properties of these nanoscale defects.

4.3 Experimental

A $FeSe_{0.5}Te_{0.5}$ target was prepared by a standard solid-state reaction method with appropriate stoichiometric mixture of the Fe, Se and Te powders. The pure $FeSe_{0.5}Te_{0.5}$ thin film and the $FeSe_{0.5}Te_{0.5}$ thin film with a 7 nm thick CeO_2 interlayer were deposited at 400 °C on single crystal STO (001) substrates in the PLD system with a KrF excimer laser (Lambda Physik Compex Pro 205, λ=248nm, 5Hz). During deposition, the target-substrate distance was kept at 4.5 cm. The growth rates of the $FeSe_{0.5}Te_{0.5}$ and CeO_2 are around 0.5 Å/pulse and 1 Å/pulse, respectively. The CeO_2 interlayer was introduced into $FeSe_{0.5}Te_{0.5}$ matrix by alternating ablation of the $FeSe_{0.5}Te_{0.5}$ and the CeO_2 targets. The laser power density was 3 J/cm^2 for both $FeSe_{0.5}Te_{0.5}$ and CeO_2 layer. The base pressure for all the depositions was around 10^{-6} Torr in vacuum. The depositions under oxygen pressure were conducted around 10^{-4} Torr. The total thickness of the $FeSe_{0.5}Te_{0.5}$ thin films was kept around 150 nm.

The microstructure of the films was characterized by X-ray diffraction (XRD) (BRUKER D8 powder X-ray diffractometer), transmission electron microscopy (TEM) and scanning transmission electron microscopy (STEM) (FEI Tecnai G2 F20). The superconducting properties were characterized using resistivity-temperature (R-T) measurement by a four point probe method from 2 K to 300 K in a physical property measurement system (PPMS, Quantum Design). Both the self-field and in-field critical current density (J_c^{sf} and $J_c^{in\text{-}field}$ (H//c)) were measured under the applied magnetic field

of 0 T ~ 7 T at various temperatures (8 K, 4 K and 2 K) by the vibrating sample magnetometer (VSM) in the PPMS.

4.4 Results and Discussion

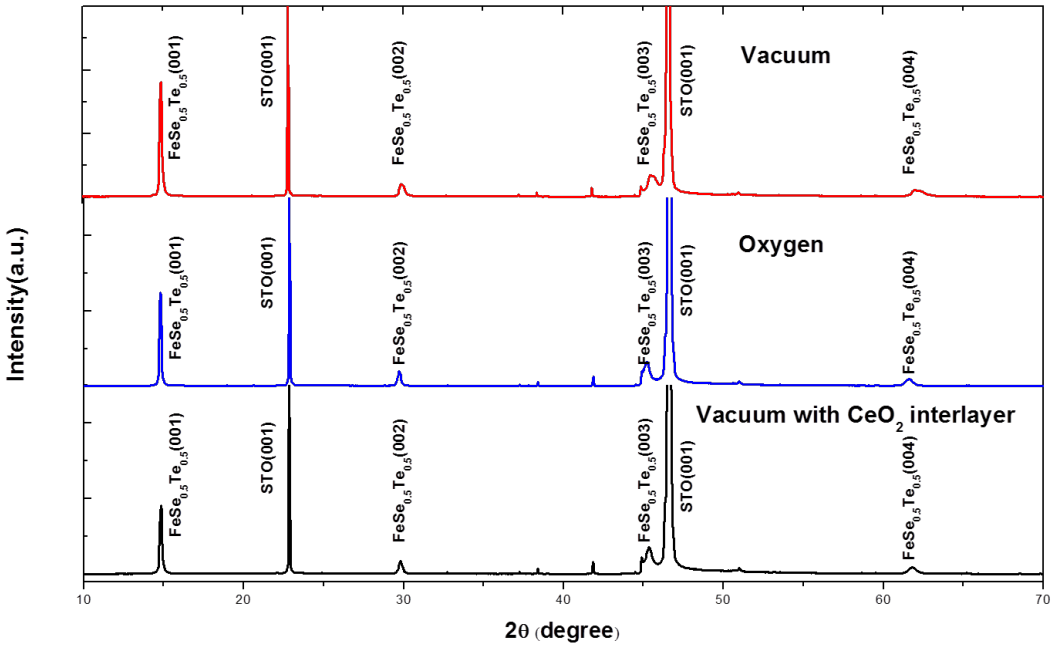

Figure 4. 1 XRD plots of the single layer $FeSe_{0.5}Te_{0.5}$ thin films and the film with the CeO_2 interlayer on STO.

Figure 4. 1 shows the standard θ-2θ XRD scans for the $FeSe_{0.5}Te_{0.5}$ films deposited on the STO substrates at 400°C. All the $FeSe_{0.5}Te_{0.5}$ films are determined to be tetragonal phase without impurity phase and highly textured along $FeSe_{0.5}Te_{0.5}$ (00*l*) on STO (001). The c-axis lattice parameters for the $FeSe_{0.5}Te_{0.5}$ film deposited in vacuum, deposited in oxygen atmosphere and the film with the CeO_2 interlayer are 5.9527 Å, 5.9848 Å and 5.9718 Å, respectively, which are comparable to the literature reports

[152, 153]. Because of the small amount of CeO_2, there is no obvious CeO_2 peak in the XRD plot. Interestingly, the film deposited in oxygen atmosphere does not have a reduced c-axis parameter compared to the other films. Based on this observation, it is possible that the introduction of oxygen during deposition caused the film structure variation which could reduce the film stress partially. Further discussion can be found in the later part of the paper.

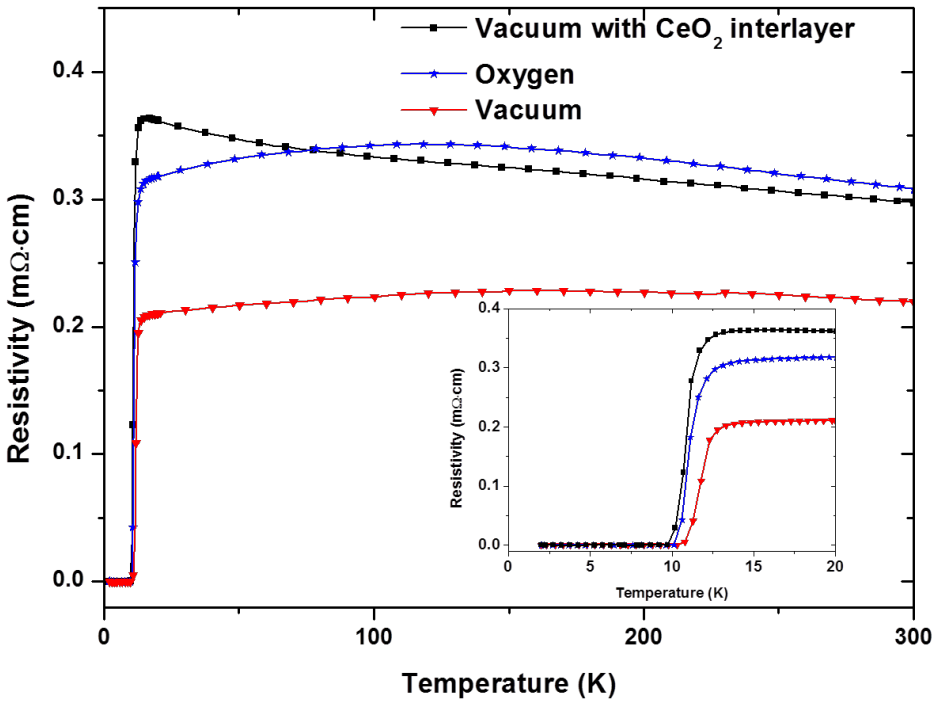

Figure 4. 2 R-T plots of the $FeSe_{0.5}Te_{0.5}$ thin films on STO from 2 K to 300 K. The inset shows the detailed superconducting transition regime from 2 K to 20 K.

R-T measurements (2 K-300 K) were conducted for all the films on STO and the results are plotted in Figure 4. 2. The details from 2 K to 20 K are shown in the inset. All

the films show a similar transition temperature T_c ranging from ~12 K (T_c^{onset}) to ~ 10 K (T_c^{zero}). The minor difference is the film deposited in vacuum shows the highest T_c^{zero} and the vacuum film with the CeO_2 interlayer shows a lower T_c^{zero}. Besides, the normal state resistivity for different film configurations ranges from 0.3 mΩ·cm to 0.5 mΩ·cm. The film deposited in oxygen atmosphere has a slightly higher normal state resistivity than the film deposited in vacuum, which possibly indicates additional defects in the oxygen deposited film. The film with the CeO_2 layer has the highest normal state resistivity among all the samples which can be partly attributed to the CeO_2 interlayer that gives a semiconductor-like behavior before the superconducting transition.

The magnetic hysteresis loops measured with the magnetic field parallel to the c-axis of the thin films are compared in Figure 4. 3a, b and c for the vacuum one, the oxygen one and the one with the CeO_2 interlayer, respectively. There is no obvious fishtail shape in the hysteresis loops for all the samples. The fishtail shape was reported in the bulk $FeSe_{0.5}Te_{0.5}$ and is correlated to the existence of a weak or non-superconducting phase [58, 59]. This suggests the films are free from those weak or non-superconducting phases. The critical current densities for all the films were derived by the Bean model which gives a reasonable estimation of the actual J_c value for the moderate magnetization change in the testing range [58, 59, 65]. The calculated J_c values are plotted in Figure 4. 3d, e and f, for 2 K, 4 K and 8 K, respectively. First, the vacuum and oxygen samples show very similar self-field J_c and in-field performance up to 4 T. After 4 T, the oxygen deposited sample shows a better in-field performance. More interestingly the sample with the CeO_2 interlayer shows an obviously enhanced J_c value

in all field range up to 7 T. The calculated self-field current density for the film with the CeO_2 interlayer at 2 K is ~10^5 A/cm^2. This value is comparable to the bulk single crystal counterpart reports [59, 64, 65]. Even at 8 K the J_c plot remains flat up to 7 T. To quantitatively compare the flux pinning property, the power-law exponent α values for the low-field regime were estimated and compared for different films based on the insets of the log-log plots of J_c vs. field. The α values for the single layer sample deposited in vacuum are 0.30, 0.38 and 0.65 at 2 K, 4 K and 8 K, respectively. The one with the CeO_2 interlayer has the lowest α values among all the samples, i.e., 0.21, 0.24 and 0.33 at 2 K, 4 K and 8 K, respectively. This suggests a significantly improved in-field performance for the sample with the CeO_2 interlayer compared to the other configurations. Comparing two single layer samples, the sample deposited in oxygen atmosphere shows a better in-field performance especially under high magnetic fields. It is possible that the defects introduced during the oxygen deposition could act as the pinning centers in the sample. An improved flux pinning property was also reported in single crystal $FeSe_{0.5}Te_{0.5}$ bulk samples and it was correlated with a possible iron oxide formation in the sample [65]. However the flux pinning enhancement is much more significant in the film with the CeO_2 interlayer.

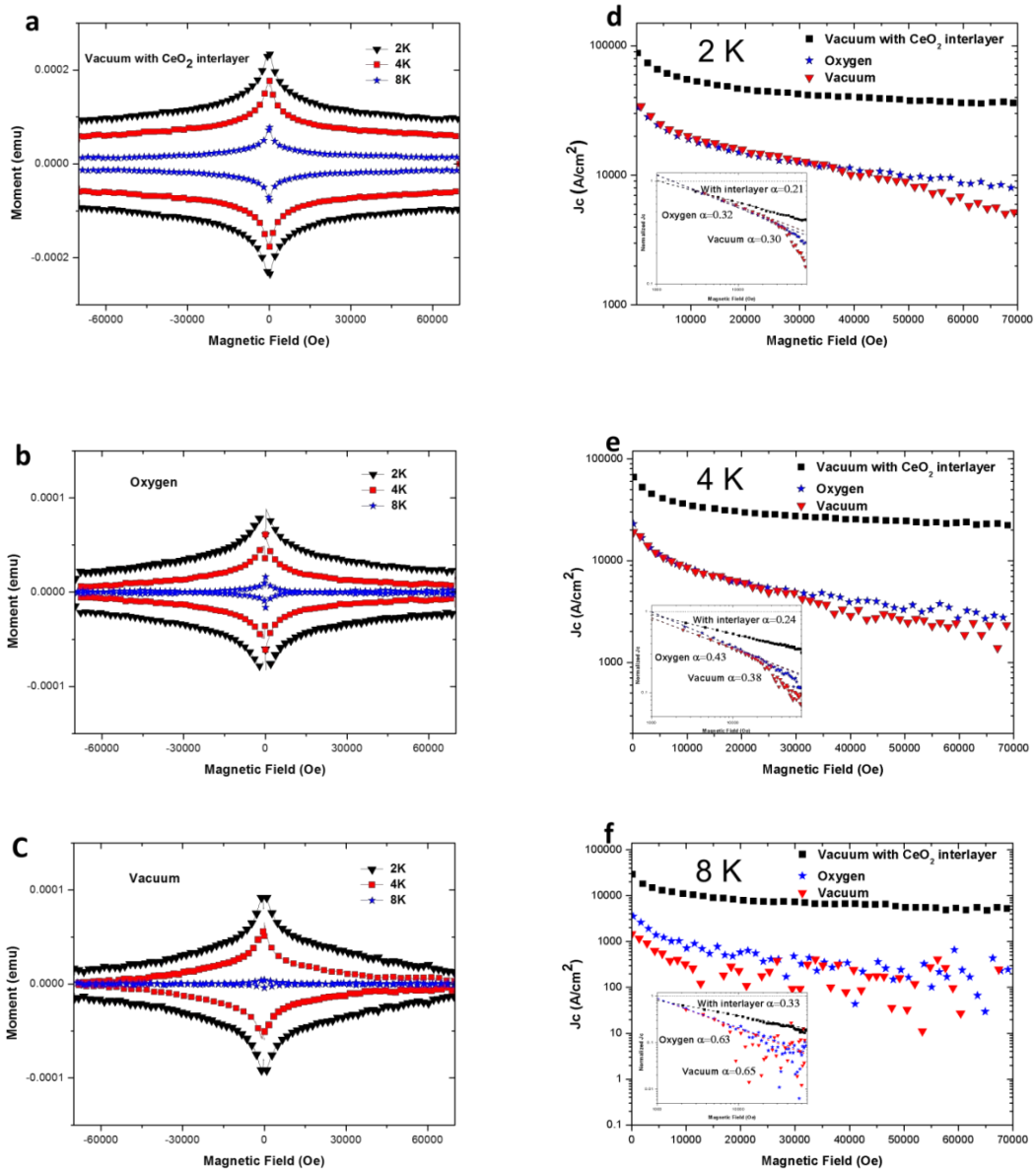

Figure 4. 3 Magnetic hysteresis loops of the $FeSe_{0.5}Te_{0.5}$ thin films deposited (a) in vacuum with the CeO_2 interlayer, (b) in oxygen, and (c) in vacuum, at 2 K, 4 K and 8 K. The corresponding field dependence of the critical current density for $FeSe_{0.5}Te_{0.5}$ thin films at (d) 2 K, (e) 4 K and (f) 8 K. The insets show the normalized critical current density plots in log-log scale for α value calculation.

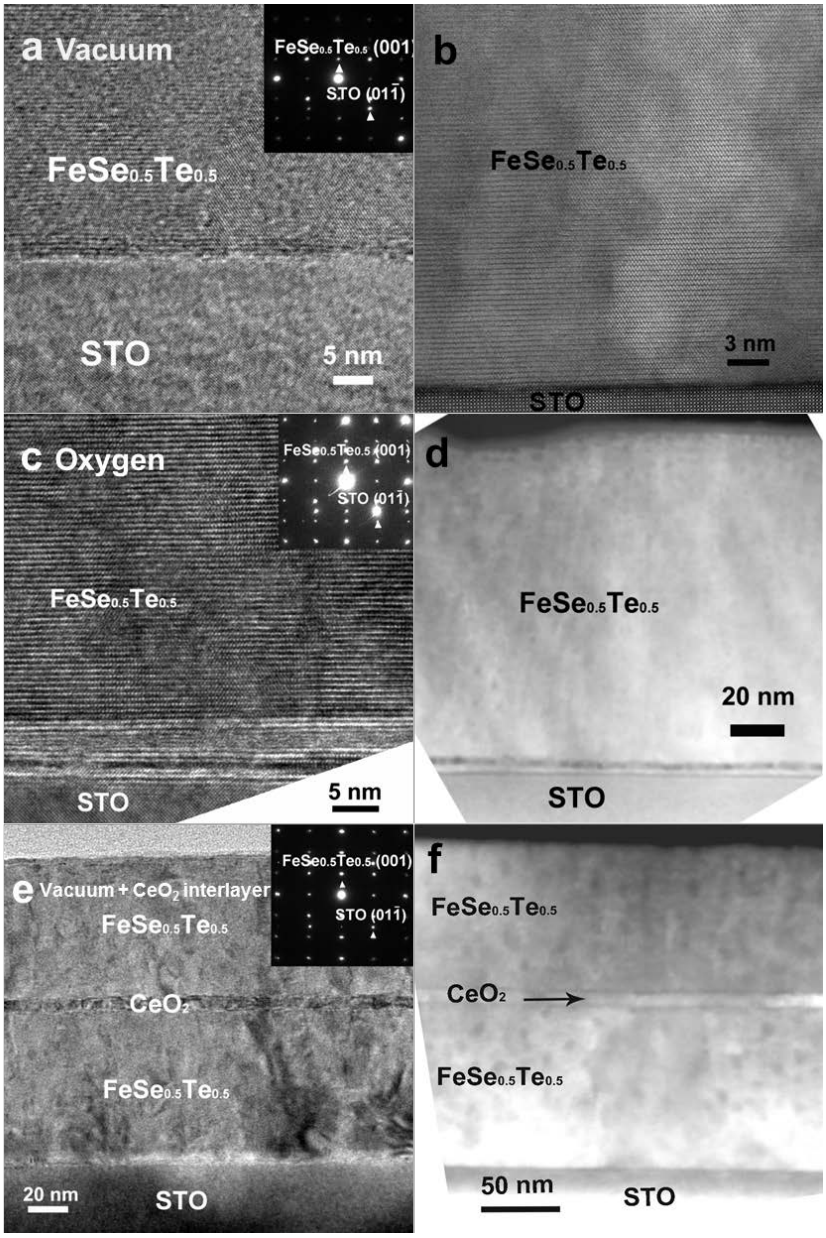

Figure 4. 4 Cross-sectional TEM images with the corresponding selected area electron diffraction (SAED) patterns of $FeSe_{0.5}Te_{0.5}$ film deposited (a) in vacuum at 400°C, (c) in the controlled oxygen atmosphere at 400°C and (e) with the CeO_2 interlayer deposited in vacuum at 400°C. The corresponding STEM images for (a), (c) and (e) are shown in (b), (d) and (f), respectively.

To explore the origin of the enhanced pinning properties, we conducted a detailed cross-sectional TEM, HRTEM and STEM study on the films. Figure 4. 4a shows the cross-sectional TEM image of the $FeSe_{0.5}Te_{0.5}$ film deposited on STO (001) at 400^{o}C in vacuum and Figure 4. 4b shows the STEM image. Based on the TEM image and the distinguished diffraction dots in the corresponding selected area electron diffraction (SAED) patterns in Figure 4. 4a, it confirms the high quality epitaxial growth of the $FeSe_{0.5}Te_{0.5}$ film on the substrate with all the (001) planes clearly observed and parallel to STO (001) planes. The interface between the $FeSe_{0.5}Te_{0.5}$ film and STO substrate is sharp without any intermixing observed. It is noted that in Figure 4. 4b, the STEM image for sample deposited in vacuum shows a small contrast difference in the film. This contrast difference is likely due to a small variation in the orientations of the two neighboring domains in the view area.

Figure 4. 4c shows the TEM image of the film grown in oxygen atmosphere. The high epitaxial quality is evident by the clear lattice fringes, similar to that of the film deposited in vacuum. One feature different from the film deposited in vacuum is the non-uniform contrast in the film observed in the STEM analysis in Figure 4. 4d. STEM is also called Z-contrast image where the contrast is proportional to Z^2 (more precisely $Z^{1.7}$). The contrast variation clearly demonstrates the non-uniform distribution of the film composition, i.e., there are uniformly distributed nanoclusters with dark contrast. The average diameter of the clusters is around 10 nm. The dark contrast suggests these clusters are Te-deficient or Se-rich areas. These clusters could relax the strain and stress in the film. Usually in an ultra-high vacuum chamber used to deposit oxide materials, it

tends to form oxides, e.g., Fe_3O_4 was observed by magnetic susceptibility measurement, XRD and TEM in previous reports [65, 146]. However in this case, the Fe_3O_4 peak was not observed in the XRD plot possibly because of the trace amount of Fe_3O_4 in the film. Most likely the observed nanoclusters are Te-deficient or Se-rich areas instead of Fe_3O_4, since the $FeSe_{0.5}Te_{0.5}$ film matrix lattices are continues without obvious lattice structure variation across the film in the TEM images. It is highly possible these nanoclusters (Te-deficient or Se-rich areas) introduced additional pinning centers in the sample that result in a better in-field performance compared to the sample deposited in vacuum.

Figure 4. 4e shows the cross-sectional TEM image of the $FeSe_{0.5}Te_{0.5}$ film with the CeO_2 interlayer deposited on STO (001) at 400^oC in vacuum. The sharp interface indicates the good chemical compatibility between $FeSe_{0.5}Te_{0.5}$ and CeO_2. The epitaxial quality is high and comparable with the single layer samples. This suggests that CeO_2 provides a nice epitaxial interlayer in the matrix and does not deteriorate the overall film epitaxial quality. Based on the fast Fourier Transformation (FFT) images in Figure 4. 5 as well as the XRD plots in Figure 4. 1 and SAED in Figure 4. 4, the epitaxial relations are determined to be $(001)_{FeSe0.5Te0.5}//(001)_{CeO2}//(001)_{STO}$ and $(200)_{FeSe0.5Te0.5}//(220)_{CeO2}//(200)_{STO.}$ The lattice mismatch is only as small as 0.3% between $(200)_{FeSe0.5Te0.5}$ and $(220)_{CeO2}$. The composition distribution analysis was performed by STEM as shown in Figure 4. 4f. The contrast difference in the thin interlayer is obvious. Again these nanoclusters are dark which suggests Se-rich or Te-deficient areas. However the clusters are bigger (~20 nm) compared to the film deposited

in oxygen. These nanoclusters could be effective pinning centers responsible for the enhanced pinning properties.

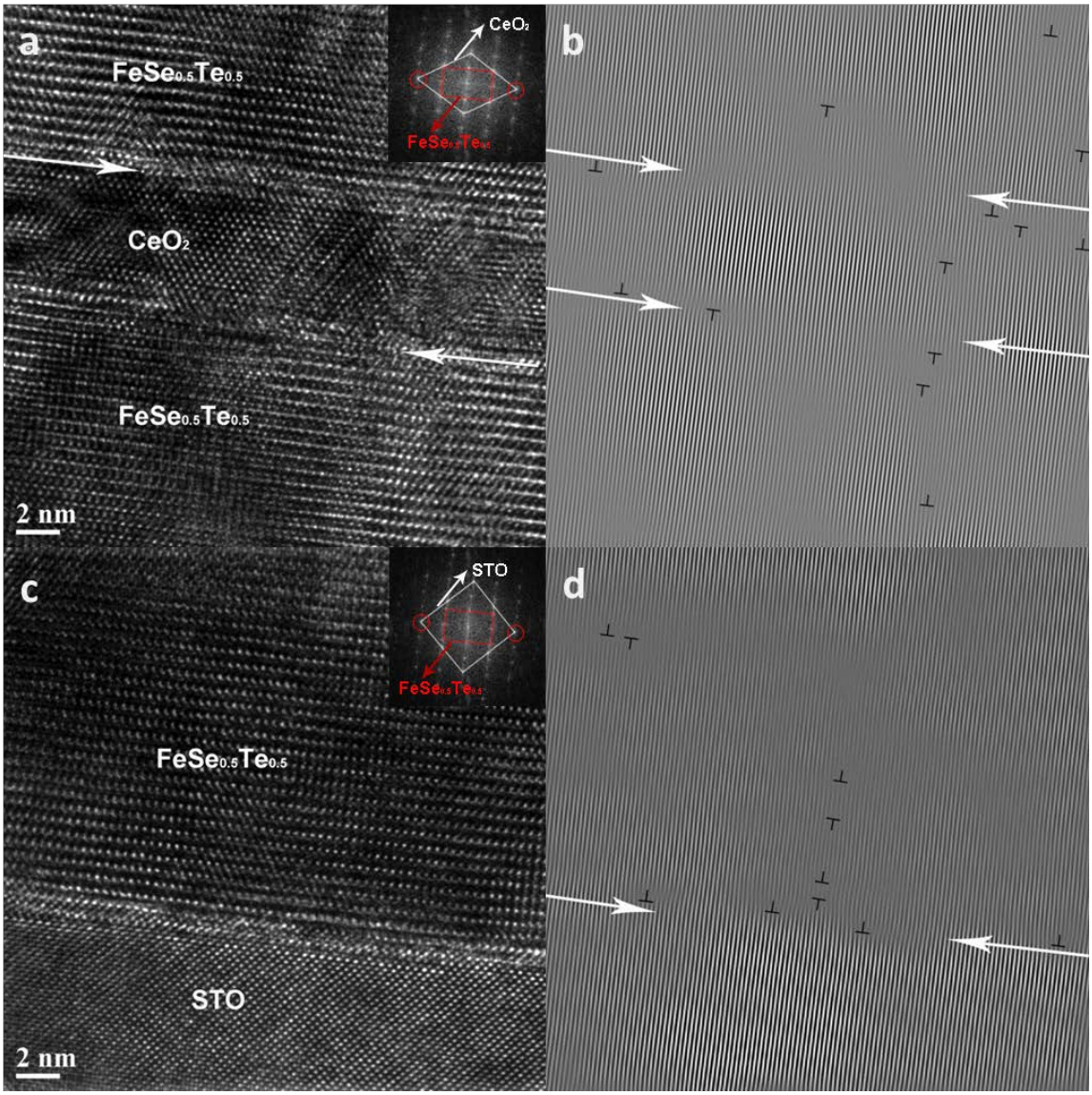

Figure 4. 5 Cross-sectional HRTEM images of (a) the CeO_2/$FeSe_{0.5}Te_{0.5}$ interface and (c) the $FeSe_{0.5}Te_{0.5}$/STO interface in the CeO_2 interlayer sample. The corresponding fast Fourier filtered images with dislocations indicated are shown in (b) and (d).

High resolution TEM image of the $FeSe_{0.5}Te_{0.5}$/CeO_2 interface and the corresponding FFT image are shown in Figure 4. 5a. The corresponding FFT filtered

image in Figure 4. 5b shows the defects along the $FeSe_{0.5}Te_{0.5}/CeO_2$ interface as well as in the $FeSe_{0.5}Te_{0.5}$ matrix. It is clear that high density misfit dislocations are observed along the interfaces as well as the area a few nms away from the interfaces. Similarly high resolution TEM image and the corresponding FFT filter image of the $FeSe_{0.5}Te_{0.5}$/STO interface from the nanolayer sample are shown in Figure 4. 5c and d, respectively. High density misfit dislocations are also observed at the interface area and extend to areas beyond the interface. This suggests that the dislocation density around the CeO_2 nanolayer interfaces is higher than that around the $FeSe_{0.5}Te_{0.5}$/STO interface.

The enhanced in-field performance in both the film with the CeO_2 interlayer and the single layer film deposited in oxygen might be originated from the nanoclusters observed as well as the interfacial defects (misfit dislocations and strains) introduced by the heterogeneous interfaces. The film with the CeO_2 interlayer has larger nanoclusters. However it also contains small defects including high density interfacial misfit dislocations along the interfaces as well as more grain boundaries in the top $FeSe_{0.5}Te_{0.5}$ layer. This combination of defects could introduce stronger pinning effects in the sample compared to the ones with just the smaller nanoclusters. Most likely the interfacial defects introduced by the CeO_2 nanolayer in the film are responsible for the enhanced superconducting properties under self-field and low field, while the uniformly distributed nanoclusters in the CeO_2 nanolayer sample are strong fluxing pinning centers at high magnetic field. A more detailed microstructural study is underway to reveal the exact composition of the nanoclusters as well as their formation mechanisms in the films.

4.5 Conclusions

We have successfully grown epitaxial superconducting $FeSe_{0.5}Te_{0.5}$ thin films on STO substrates with various deposition conditions and with or without the CeO_2 interlayer. The samples all have a similar T_c^{onset} around 12K, while their in-field performances are vastly different. The sample with the CeO_2 interlayer shows the highest J_c in the whole magnetic field range (0 T to 7 T) and the J_c is as high as 2.8×10^4 A/cm^2 at 7 T at 2 K. The J_c plot remains very flat up to 7 T and the extrapolated α value for the sample is around 0.21 at 2 K. It suggests the $FeSe_{0.5}Te_{0.5}$ thin film with the CeO_2 interlayer has the best in-field performance among all the samples. The enhanced in-field performance is attributed to the high epitaxial film quality, uniformly distributed nanosize clusters (Se-deficient and Te-rich regions) and the additional interfacial defects introduced by the CeO_2 nanolayer. This is an initial demonstration of enhanced in-field performance of $FeSe_{0.5}Te_{0.5}$ thin films using nanoscale defects in the film matrix.

CHAPTER V

HIGHLY TEXTURED SUPERCONDUCTING $FESE_{0.5}TE_{0.5}$ THIN FILMS ON GLASS SUBSTRATES*

5.1 Overview

Superconducting $FeSe_{0.5}Te_{0.5}$ thin films are deposited on amorphous substrates, i.e. glass substrates by a pulsed laser deposition (PLD) technique. Microstructural characterizations show that the films are highly textured along (*00l*) with good crystallinity. The superconducting critical transition temperature (T_c) ranges from ~8 to ~10 K. The self-field critical current density (J_c^{sf}) at 4 K is ~1.2×10^4 A/cm^2. The in-field critical current density ($J_c^{in\text{-}field}$) decreases slowly under high magnetic field confirmed by both transport and magnetization measurements. The growth of high quality superconducting $FeSe_{0.5}Te_{0.5}$ thin films on amorphous substrates demonstrates a low cost architecture for future iron-based superconductor coated conductors.

5.2 Introduction

High temperature superconducting (HTS) wires have gone through a revolution in the past two decades. The "first generation" (1G) powder-in-tube (PIT) HTS wires are based on the traditional wire drawing of the $Bi_2Sr_2Ca_2Cu_3O_{10+x}$ (BSCCO) (T_c=112 K). However the grains in the wire are not well aligned which results in low J_c and also the cost is relatively high due to the use of silver in these superconducting wires.[116] The "second generation" (2G) HTS coated conductor wires are based on the high quality epitaxial growth of $YBa_2Cu_3O_{7-\delta}$ (YBCO) films on either rolled textured metal substrates (so-called RABiTS process)[117] or the ion-beam-assisted deposition of highly textured template (IBAD) on metal substrates[118-120]. In the above two generations of HTS wires, either highly epitaxial template for the growth of YBCO film, or rolling and post-heat treatment for the case of highly textured BSCCO wires is required.

Since 2008 the discovery of iron-based superconductors $La[O_{1-x}F_x]FeAs$[21] has triggered the exploration of superconductors with even better performance than cuprates under some circumstance as well as their superconducting mechanism research. Among them iron chalcogenide is a promising material with a binary composition.[25] Compared to the iron pnictide it does not contain the toxic arsenic and it has the simplest structure without decoration between each iron layer which is responsible for the superconducting properties. The T_c of the FeSe can be boosted to 37 K by pressure effect.[31] In the covalent doped iron chalcogenide, the superconducting property was enhanced by changing the Se/Te height.[82] The epitaxial iron chalcogenide thin films were grown on various single crystalline substrates including $SrTiO_3$ (STO), MgO and

$LaAlO_3$ (LAO); by deposition parameter optimization, the superconducting properties can be further tuned.[45, 100] The J_c was also explored for bulk as well as thin films.[66, 109, 154, 155] For the optimized thin films on single crystal substrates[66, 154], the J_c^{sf} is as high as 8×10^5A/cm^2 at 4.2 K which is much higher than the polycrystalline thin film[155] with J_c^{sf} lower than 10^3A/cm^2. Even the design of the pinning landscape was carried out to optimize the in-field performance of iron chalcogenide thin films.[156] Very recently, IBAD epitaxial MgO coated Hastelloy substrates were used to grow high quality $FeSe_{0.5}Te_{0.5}$ tape with excellent in-field performance. It has a great potential to substitute Nb_3Sn wires which are dominant in the high field applications including the commercialized high field medical equipment and magnetic measurement systems.[67] However the films grown on single crystalline substrates cannot be easily used for large scale coated conductor applications and the films demonstrated on IBAD substrate involves multiple steps of seed layer and buffer layer deposition to establish the epitaxial growth template for the following iron chalcogenide growth. Therefore a simplified and cost effective iron-based coated conductor is more desirable.

Here we demonstrate for the first time that the superconducting $FeSe_{0.5}Te_{0.5}$ film can be directly grown on amorphous glass substrates with one-step deposition. Here glass substrates were selected for the demonstration of the highly textured thin film growth and excellent superconducting properties, e.g., transition temperature of 10 K and J_c under self-field as high as 1.2×10^4 A/cm^2 at 4 K. The possible mechanism for the textured growth on amorphous substrates is also discussed.

5.3 Experimental

$FeSe_{0.5}Te_{0.5}$ targets were prepared by a standard solid-state reaction method with the appropriate stoichiometric mixture of Fe, Se, and Te powders. The $FeSe_{0.5}Te_{0.5}$ thin films were deposited at 400 °C on glass slide (Thermo Fisher Scientific Microscope Slides) in a PLD system with a KrF excimer laser (Lambda Physik Compex Pro 205, λ=248 nm, 5Hz). The base pressure for all the depositions was around 10^{-6} Torr. The total thickness of the $FeSe_{0.5}Te_{0.5}$ thin films was kept around 100 nm.

5.4 Results and Discussion

Figure 5. 1 shows the θ-2θ X-ray Diffraction (XRD) data for a typical film on glass substrate. The peaks are all corresponding to the (*00l*) peaks of $FeSe_{0.5}Te_{0.5}$. The calculated *c*-axis lattice parameter is around 5.88 Å which is slightly smaller than the bulk value but comparable to other thin film reports.[102, 153] The preferred (*00l*) peaks suggest that the film has grown highly textured along (*00l*) with good film quality. The XRD profile of a bare glass substrate is presented in Figure 5. 1 to confirm the amorphous nature of the substrate.

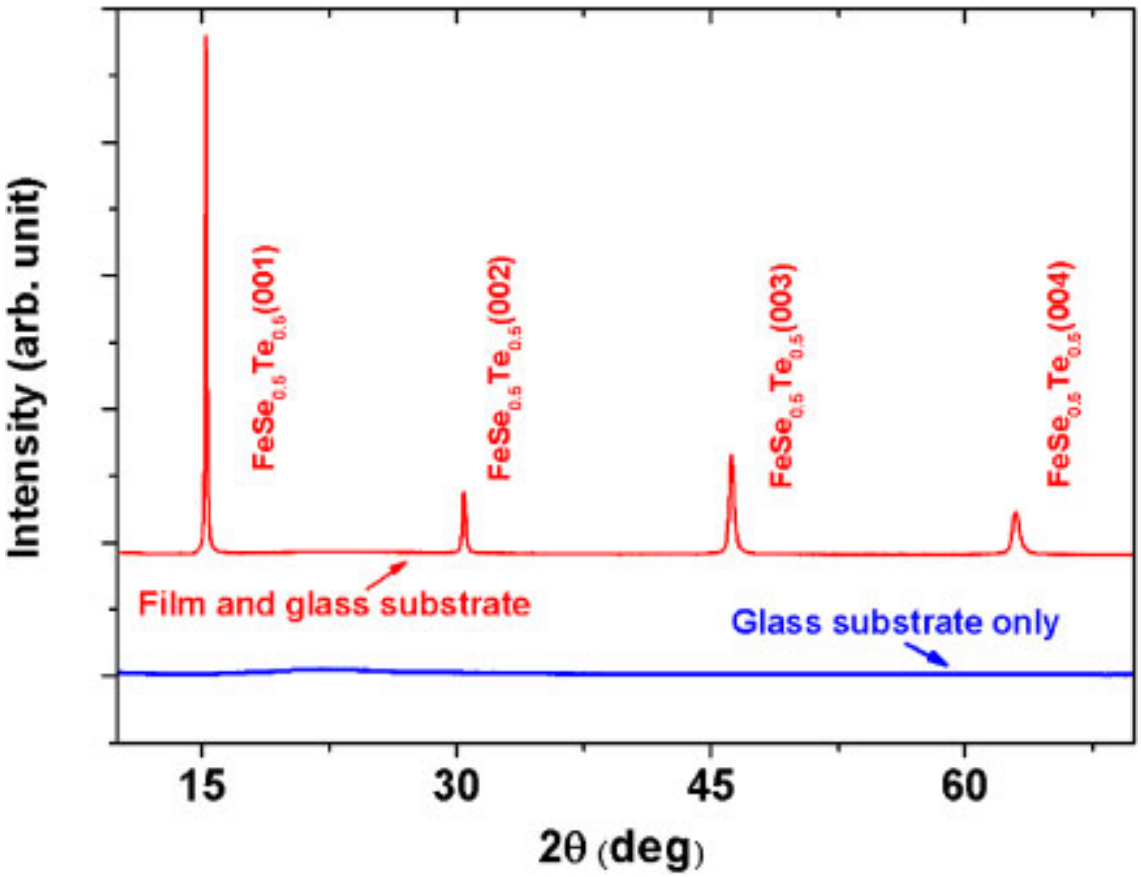

Figure 5. 1 XRD θ-2θ plots of the $FeSe_{0.5}Te_{0.5}$ thin film on glass substrate and a bare glass substrate as reference.

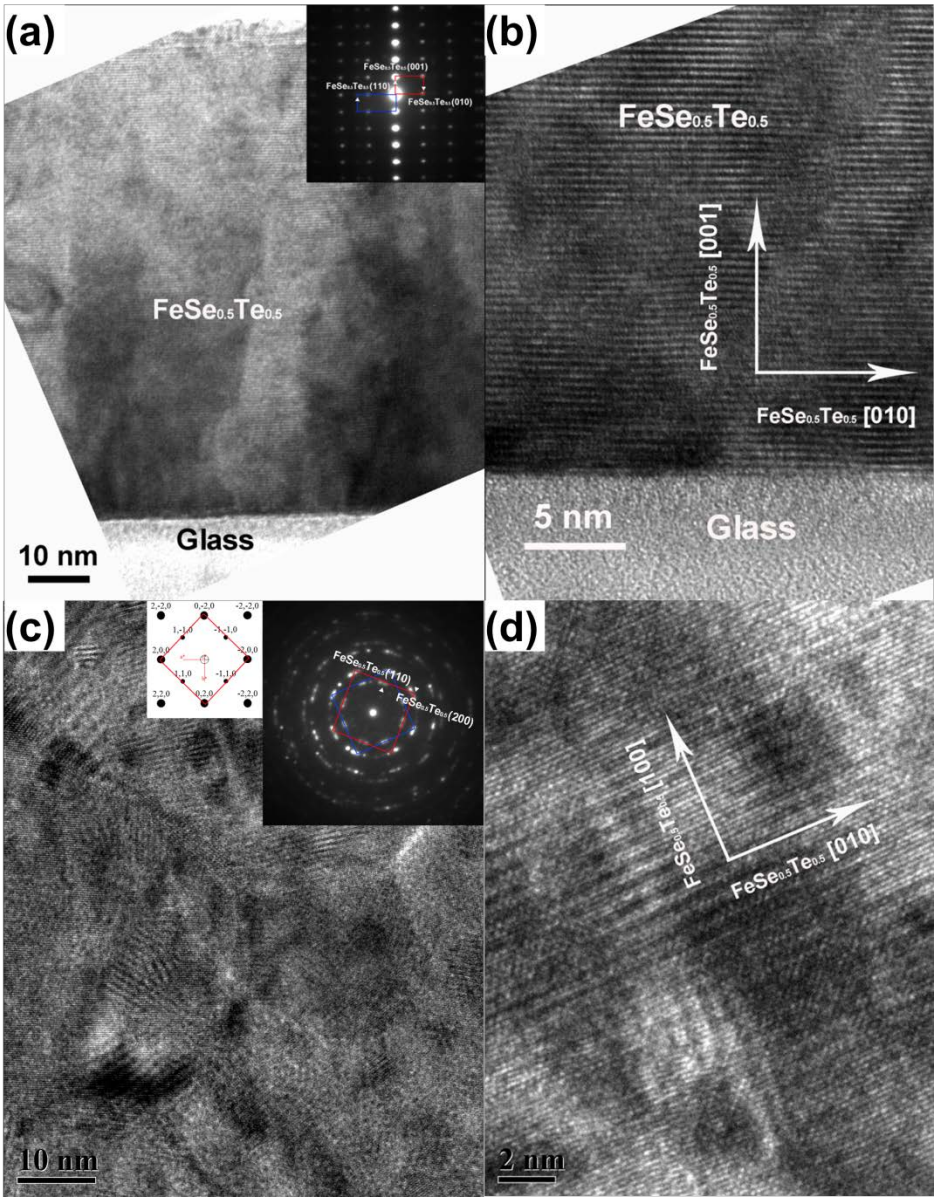

Figure 5. 2 (a) Cross-sectional TEM image with the corresponding SAED of $FeSe_{0.5}Te_{0.5}$ film deposited on glass substrate; (b) a high resolution cross-sectional TEM image; (c) plan-view TEM image with the corresponding SAED and SAED simulation in the insets; (d) a high resolution plan-view TEM image.

Figure 5. 2 presents the transmission electron microscopy (TEM) results for (a) low magnification cross-section overview, (b) high resolution cross-section view, (c)

low magnification plan-view overview and (d) plan-view high resolution image for a typical $FeSe_{0.5}Te_{0.5}$ film on glass. The cross-section TEM images (a) and (b) both present the *c*- planes are parallel to the glass surface with excellent film quality. High resolution image along the film-substrate interface shows obvious film lattices and the clean film-substrate interface. The film thickness is around 100 nm. The corresponding selected area electron diffraction (SAED) pattern demonstrates the perfect out-of-plane alignment as $FeSe_{0.5}Te_{0.5}$ (*00l*) diffraction dots are all distinguished along the vertical direction. It is interesting to note the local textured in-plane alignment of the film, i.e., the main in-plane orientation of $FeSe_{0.5}Te_{0.5}$ (010) with a minor orientation of $FeSe_{0.5}Te_{0.5}$ (110) indicated by the weak spots in the diffraction pattern in Figure 5. 2 (a) [the (010) and (110) orientations are notated by the red and blue rectangles in the diffraction pattern, respectively].

In Figure 5. 2 (c) the low magnification plan-view image with the corresponding diffraction pattern is shown. The diffraction pattern indicates two sets of diffraction dots (with certain range of arcs) marked as two squares which is consistent with the diffraction pattern simulation in the inset of Figure 5. 2 (c). The two sets of diffraction dots/arcs are ~ 45 ° apart which can be correlates to the two sets of grains that are 45 ° apart in-plane. It is noted that the local in-plane texture exists in the film on amorphous substrate but it is relatively local.

The surprising part comes from the semi-epitaxial growth of the $FeSe_{0.5}Te_{0.5}$ film (i.e., excellent out-of-plane texture and local in-plane texture property) on amorphous substrate, a substrate without any typical crystal structure or grain alignment. This

suggests that $FeSe_{0.5}Te_{0.5}$ has a great tendency in growing in a preferred grain alignment even on random amorphous substrate. In addition, based on previous thin film reports[45, 55], the substrate lattice confinement which introduces the tetrahedral distortion was claimed to be responsible for the *c*-axis reduction. In our case, based on SAED pattern in Figure 5. 2 (a), the *a* and *b*-axis parameters remain the same as the bulk value around 3.79 Å. But interestingly the *c*-axis from the SAED pattern is reduced to 5.88 Å, which is consistent with the XRD results. It is possible that the *c*-axis reduction is the intrinsic property of the $FeSe_{0.5}Te_{0.5}$ thin film compared to bulk, since there is no or very limited substrate confinement from the amorphous substrates. According to Imai *et al.* the high c/a ration is important for the superconducting transition temperature[157]; in our case the ratio is comparable to that on MgO, STO and LAO substrates.

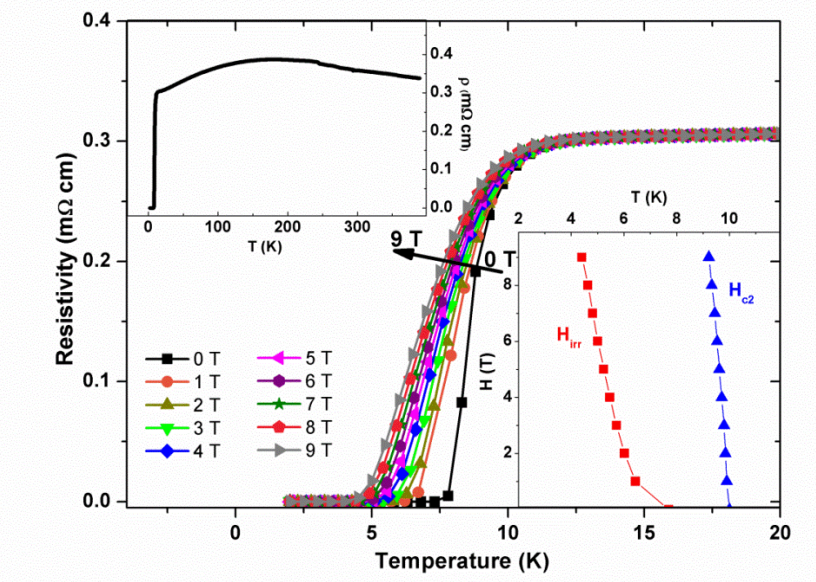

Figure 5. 3 R-T plot of the $FeSe_{0.5}Te_{0.5}$ thin film on glass substrate from 2 K to 20 K under magnetic field (0-9 T). The insets show the whole measurement range from 2 K to 400 K and the irreversibility line $H_{irr}(T)$ and the upper critical field $H_{c2}(T)$.

The superconducting properties of the films were first characterized using the resistivity-temperature (R-T) measurement by a four-point probe method in a physical property measurement system (Quantum Design PPMS 6000). The in-field transport measurement up to 9 T (H//c) is demonstrated. Figure 5. 3 shows the thin film has a transition from ~10 K (T_c^{onset}) to ~8 K (T_c^{zero}). The irreversibility line $H_{irr}(T)$ extrapolated with the T_c^{zero} and the upper critical field $H_{c2}(T)$ extrapolated with the T_c^{onset} are plotted in the inset. The upper critical field was estimated by the Werthamer-Helfand-Hohenberg model,

$$-\boldsymbol{H_{c2}(0) = 0.7T_c\, dH_{c2}/dT\,|T_c}$$ (Equation 5. 1)

using the onset of the superconducting transition temperature.[55, 101] The upper critical field H_{c2} is estimated to be ~ 77 T. Compared to the previous reports the upper critical field is slightly smaller than that of the film on single crystal substrate of 100 T [102] , however much higher than 27 T reported in the $FeSe_{0.5}Te_{0.5}$ superconductor wires made by PIT method [123].

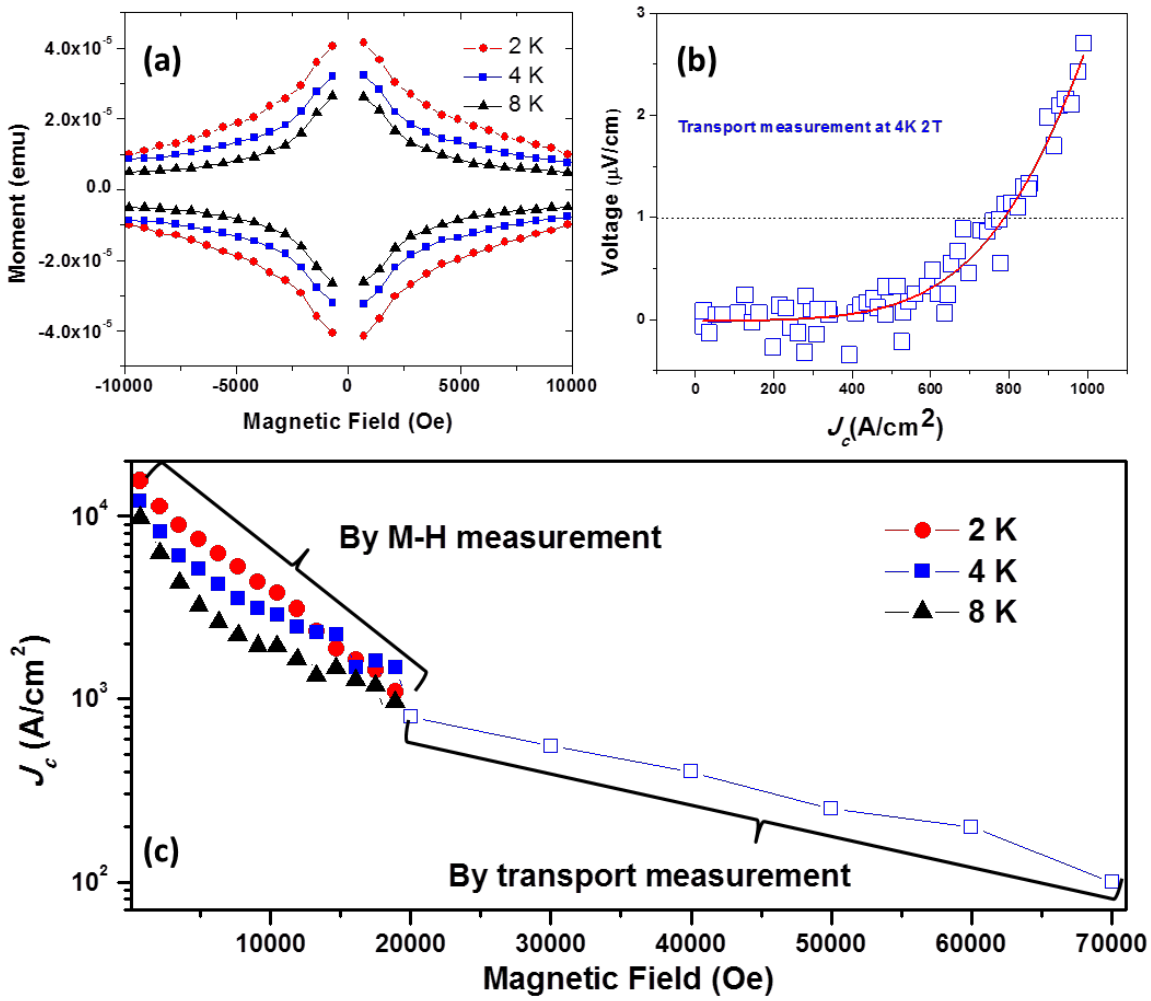

Figure 5. 4 (a)The field dependence of the critical current density for a typical $FeSe_{0.5}Te_{0.5}$ thin film on glass measured by both M-H and transport measurements; (b) the magnetic hysteresis loops at 2 K, 4 K and 8 K; (c) the representative transport measurement at 4 K and 2 T.

Both the self-field and in-field critical current density values [J_c^{sf} and $J_c^{in\text{-}field}$ (H//c)] were measured under the applied magnetic field of 0 T ~ 7 T at various temperatures (8, 4, and 2 K) by the vibrating sample magnetometer (VSM) in PPMS.

Here the moment versus magnetic field (M-H) hysteresis loops are shown in Figure 5. 4 (a). For the VSM measurement the critical current densities were derived by the Bean model,

$$J_c = \frac{20\Delta M}{a(1-a/3b)} \text{ (Equation 5. 2)}$$

where ΔM is the opening in the hysteresis loop; a and b are the sample dimensions. The calculated self-field current density at 4 K is ~1.2×10^4 A/cm^2.

In addition we carried out a transport measurement to directly measure J_c. Due to the current limit in PPMS (1000 A/cm^2) it could only measure from 2 to 7 T for these samples using the transport measurement. As an example, the measurement result at 4 K under 2 T was plotted in Figure 5. 4 (b). The 1 μV/cm criterion was used to measure the J_c. The J_c versus magnetic field plot using the VSM results as well as the transport measurement results at 4 K are plotted in Figure 5. 4 (c). The J_c results are quite consistent by these two techniques and the J_c plot is continuous at 4 K, for example J_c at 4 K, 2 T is ~800 A/cm^2. In the high magnetic field range the J_c decreases slowly as the field increases. This film presents a much higher J_c^{sf} than the iron chalcogens wires made by the diffusion method using the PIT technique which have a J_c^{sf} value around 200 A/cm^2.[123, 158, 159] The J_c^{sf} is still one order of magnitude smaller than the epitaxial films grown on the IBAD MgO which have a J_c^{sf} as high as 2×10^5 A/cm^2.[67] This could be correlated with the local in-plane textured property of the films with high grain boundary density in the film which is a common reason for the J_c depression in the cuprates as well as in iron pnictides[121]. In addition the T_c of 10 K is lower than the films on single crystal substrates which have a T_c^{onset} ranging from 12 to 21 K. [63, 109,

154, 156, 160] However this initial demonstration of iron chalcogenide thin film directly grown on amorphous substrate has already shown impressive in-plane and out-of-plane texture and good superconducting properties comparable to some literature reports.[157, 161] The initial amorphous layers on the single crystal substrate were considered detrimental to the superconducting properties. However in our case the amorphous substrate did not deteriorate the superconducting transition, on the contrary it shows better properties than the films on some of the incompatible single crystal substrates.[157, 161] With further optimization on the deposition and selecting different amorphous substrates, there is still room to further improve the film in-plane texturing to a larger scale and minimize the grain boundary density to achieve better superconducting properties. The approach demonstrates a low cost method for processing a new class of coated conductors on low cost substrates, including glass and amorphous buffered metal tapes. In addition, further work shall be considered to achieve a smooth growth surface regardless of the substrate texture or the atomic scale lattice parameter, and minimize the film-substrate interaction.

5.5 Conclusions

In conclusion, highly textured $FeSe_{0.5}Te_{0.5}$ thin films were deposited on glass substrates with a T_c^{onset} of 10 K and an upper critical field of 77 T. The self-field critical current density is around 1.2×10^4 A/cm^2 at 4 K and $J_c^{in\text{-}field}$ is ~800 A/cm^2 at 4 K, 2 T. This is the first demonstration of highly textured iron chalcogenide thin film on amorphous substrates, which presents a new approach for processing iron-based

superconductor coated conductors on amorphous substrates or amorphous buffered metal substrates.

CHAPTER VI

GROWTH AND PINNING PROPERTIES OF SUPERCONDUCTING NANOSTRUCTURED $FESE_{0.5}TE_{0.5}$ THIN FILMS ON AMORPHOUS SUBSTRATES*

6.1 Overview

$FeSe_{0.5}Te_{0.5}$ thin films were deposited by a pulsed laser deposition technique on amorphous substrates, e.g. for demonstration, glass substrates were used. Various interlayers were introduced to enhance the superconducting properties. Detailed microstructural characterizations including X-ray diffraction (XRD) and cross-sectional transmission electron microscopy (TEM) were conducted to verify the film quality. The results indicated the highly textured $FeSe_{0.5}Te_{0.5}$ film along *(00l)* direction on the glass substrate with good crystallinity. The transport properties were measured by a physical property measurement system (PPMS). The superconducting critical transition temperature (T_c) is around 6 K. The critical current densities (J_c) were measured by the vibrating sample magnetometer (VSM) in the PPMS at 2 K under magnetic field up to 1 T. The growth of high quality superconducting $FeSe_{0.5}Te_{0.5}$ thin film demonstrates a low cost method for processing future iron-based superconductor coated conductors.

*****This chapter is reprinted with permission from "*Growth and Pinning Properties of Superconducting Nanostructured $FeSe_{0.5}Te_{0.5}$ Thin Films on Amorphous Substrates*" by Li Chen, *et al.*, *IEEE Transactions on Applied Superconductivity,* **23**, 7500904 (2013). Copyright © 2013 IEEE.

6.2 Introduction

Since the discovery of superconductivity in iron selenide (FeSe) with a transition temperature around 8 K [25], this iron-based arsenic-free superconductor with simple structure has attracted much research interest regarding its origin of superconductivity [31, 38] and the property enhancement [27, 44, 47, 63, 102]. Although the iron chalcogenide superconductor has much lower T_c compared to the traditional cuprates, the high current density at high magnetic field and the small anisotropy make it a promising substitution of NbSn/NbTi in high field applications [102]. In addition, the magnetic energy stored in an superconducting magnetic energy storage (SMES) is proportional to B^2 and therefore the high H_{c2} makes it a favorable material for energy storage systems [67].

The bulk properties of FeSe were studied thoroughly including stoichiometry [40], pressure effect [31, 46, 89], critical current density [59, 65] and covalent doping such as $FeSe_xTe_{1-x}$ and $FeSe_xS_{1-x}$ [27]. The T_c of the FeSe can be boosted to 37 K by pressure effect.[31] In the covalent doped iron chalcogenide, the superconducting property was enhanced by changing the Se/Te height [82]. The magnetic current density was also explored for bulk first with J_c as high as 10^5 A/cm^2 at 2 K however with some minor non-superconducting or weakly superconducting phase indicated by the fishtail shape magnetic hysteresis loop [59]. Later the thin films were grown on single crystal substrates. Most of the thin films were deposited by pulsed laser deposition (PLD). The lattice matching between the iron chalcogenide and the ceramic substrates such as STO, MgO and LAO, results in a high quality film with *(00l)* plane parallel to the substrate

surface [47, 55, 102, 156]. The J_c^{sf} was reported as high as 8×10^5A/cm^2 at 4.2 K for the epitaxial thin films on single crystal substrates[66, 154], which is much higher than the polycrystalline thin films with J_c^{sf} lower than 10^3A/cm^2 [155]. Towards the practical applications, the wires were made by powder-in-tube (PIT) technique, however the critical current density of the wires was only several hundred A/cm^2 [158, 159, 162] at 4 K which was much lower than the bulk value. The $FeSe_{0.5}Te_{0.5}$ film was deposited on highly textured MgO template on metal tape with ion-beam-assisted deposition (IBAD) technique which was used to grow YBCO thin films [116] and the epitaxial film has a large critical current density as high as 2×10^5 A/cm^2 at 4 K. The IBAD MgO substrate is a promising substrate for coated conductor application, however the cost is relatively high [67].

In this paper we report highly textured $FeSe_{0.5}Te_{0.5}$ films directly grown on low cost amorphous substrates by PLD method. Here we demonstrate the growth of $FeSe_{0.5}Te_{0.5}$ on glass substrate and optimization of the film growth with various nanoscale interlayers. Compared to the cuprates with a quite complex buffer layer stack and strict growth conditions such as the single crystal substrate or substrate treatment and annealing procedure, the high crystallinity and the simple stacking order make the iron chalcogenide a potential candidate for future low cost coated conductors on amorphous substrates or amorphous buffered metal substrates.

6.3 Experimental

A $FeSe_{0.5}Te_{0.5}$ target was prepared by a standard solid-state reaction method with an appropriate stoichiometric mixture of the Fe, Se and Te powders. The

$FeSe_{0.5}Te_{0.5}/CeO_2$ (1:1) composite target was prepared by solid-state reaction of the stoichiometric mixture of the Fe, Se, Te and CeO_2 powders. The pure $FeSe_{0.5}Te_{0.5}$ thin film, the $FeSe_{0.5}Te_{0.5}$ thin film with a 7 nm thick CeO_2 interlayer and the $FeSe_{0.5}Te_{0.5}$ thin film with a 7 nm thick $FeSe_{0.5}Te_{0.5}/CeO_2$ (1:1) composite interlayer were deposited at 400 °C on amorphous glass substrates cut into size 5mm × 10mm (Regular microscopic glass slides, Thermo Fisher Scientific Inc.) in a PLD system with a KrF excimer laser (Lambda Physik Compex Pro 205, 248 nm, 5 Hz). During deposition, the target–substrate distance was kept at 4.5 cm.

The growth rate of the $FeSe_{0.5}Te_{0.5}$ is around 0.5 Å/pulse. The laser power density was 3 J/cm^2 for the $FeSe_{0.5}Te_{0.5}$, CeO_2 and $FeSe_{0.5}Te_{0.5}/CeO_2$ composite targets. The base pressure for all the depositions was around 10^{-6} Torr under vacuum. The total thickness of the $FeSe_{0.5}Te_{0.5}$ thin films was kept around 100 nm. The interlayer was introduced into the $FeSe_{0.5}Te_{0.5}$ film matrix by alternating ablation of the $FeSe_{0.5}Te_{0.5}$ and the corresponding interlayer targets. The CeO_2 interlayer has been previously introduced to overcome the J_c thickness dependence in YBCO film [151]. It was also introduced into $FeSe_{0.5}Te_{0.5}$ film [156], which shows enhanced superconducting properties (J_c and T_c).

The microstructure of the films was characterized by X-ray diffraction (XRD) and transmission electron microscopy (TEM). The superconducting properties were characterized using resistivity-temperature (R-T) measurement by a four point probe method from 2 K to 300 K in a physical property measurement system (PPMS, Quantum Design). Both the self-field and in-field critical current density (J_c^{sf} and $J_c^{in\text{-}field}$ (H//c))

were measured under the applied magnetic field of 0 T ~ 1 T at 2 K by the vibrating sample magnetometer (VSM) in the PPMS.

6.4 Results and Discussion

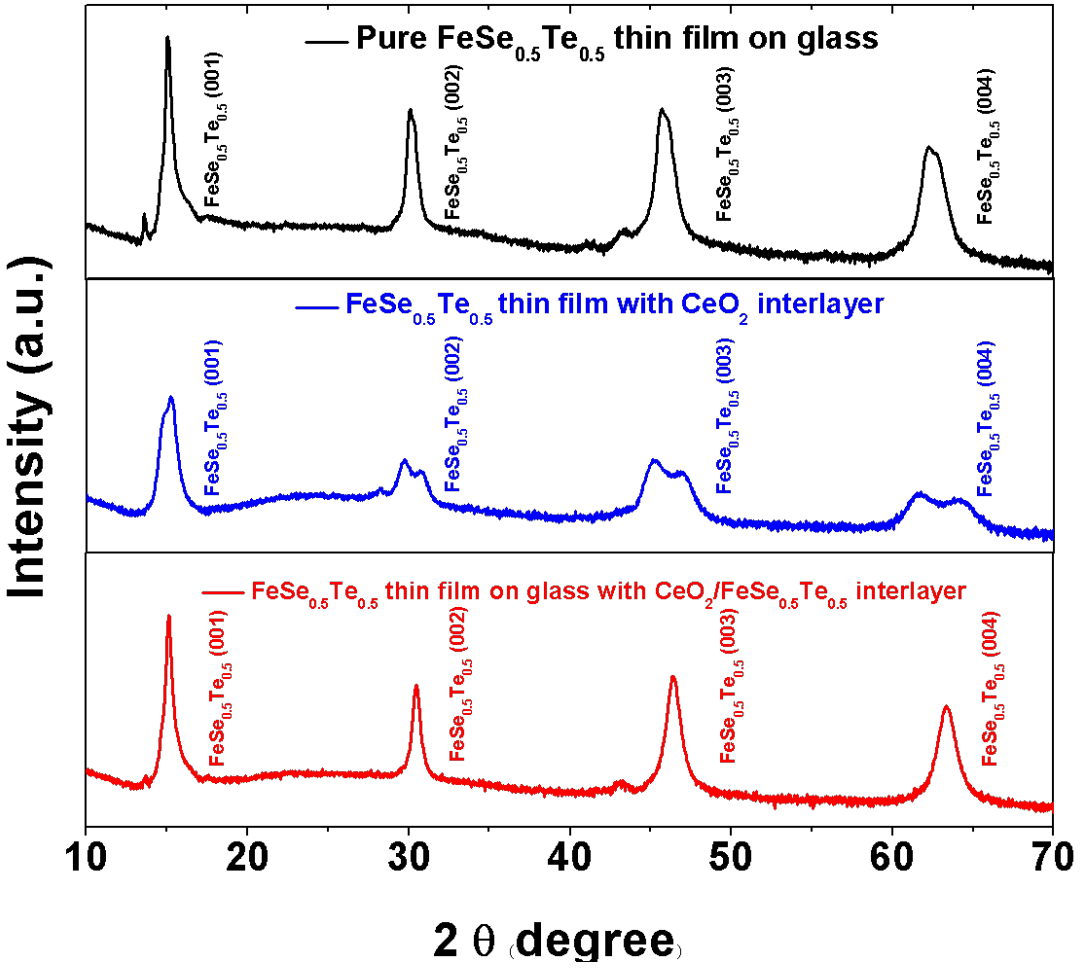

Figure 6. 1 XRD θ-2θ plots of the pure $FeSe_{0.5}Te_{0.5}$ thin film, $FeSe_{0.5}Te_{0.5}$ thin film with a CeO_2 interlayer and $FeSe_{0.5}Te_{0.5}$ thin film with a $FeSe_{0.5}Te_{0.5}/CeO_2$ composite interlayer on glass substrates.

Figure 6. 1 shows the θ-2θ XRD data for the $FeSe_{0.5}Te_{0.5}$ films on glass substrates. For all three film structures the peaks are all corresponding to the *(00l)* peaks of $FeSe_{0.5}Te_{0.5}$. The CeO_2 peak is not obvious due to the small amount of CeO_2 in the

film. The calculated *c*-axis lattice parameter is around 5.88 Å which is slightly smaller than the bulk value but comparable to other thin film reports [102, 153]. The preferred *(00l)* peaks suggest that the film has grown highly textured along *(00l)* with good film quality. The pure $FeSe_{0.5}Te_{0.5}$ film and film with $FeSe_{0.5}Te_{0.5}/CeO_2$ composite interlayer show stronger peaks compared to the film with CeO_2 interlayer. In addition the peaks for the $FeSe_{0.5}Te_{0.5}$ film with CeO_2 layer tend to split into two peaks for each *(00l)* peak. The possible reason is discussed later.

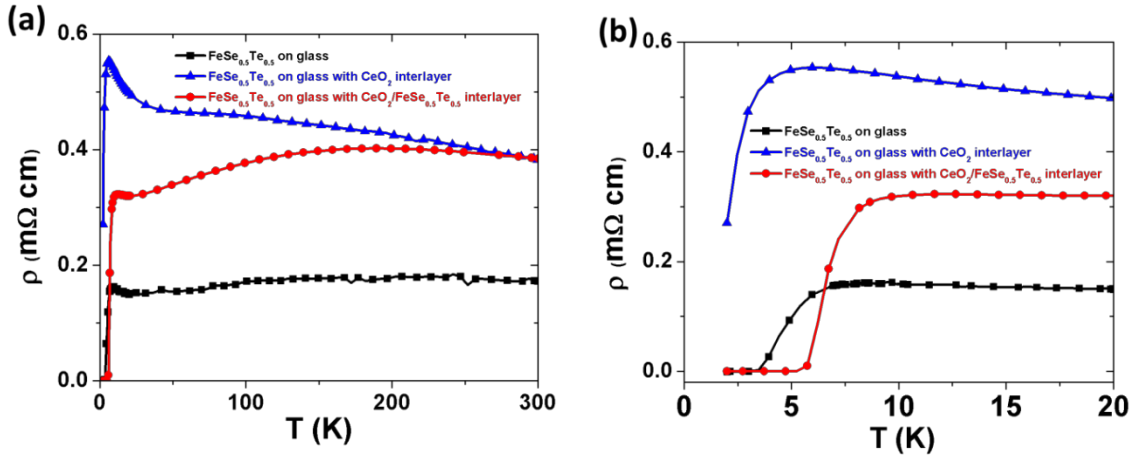

Figure 6. 2 (a) R-T plot of the pure $FeSe_{0.5}Te_{0.5}$ thin film, $FeSe_{0.5}Te_{0.5}$ thin film with CeO_2 interlayer and $FeSe_{0.5}Te_{0.5}$ thin film with $FeSe_{0.5}Te_{0.5}/CeO_2$ composite interlayer on glass substrates from 0 K to 20 K. (b) shows the whole measurement range from 2 K to 300 K.

In Figure 6. 2 R-T measurement results show a T_c^{zero} of 3 K for the pure $FeSe_{0.5}Te_{0.5}$ film. The T_c^{zero} for the film with $FeSe_{0.5}Te_{0.5}/CeO_2$ composite interlayer is around 6 K, which has the highest T_c among all three film structures. Surprisingly the film with the CeO_2 layer is not as good as expected. The reason is further illustrated in the TEM data where the CeO_2 *(001)* planes were not perfectly aligned parallel to the

substrate surface. The CeO_2 layer tends to be polycrystalline without long range order on the first $FeSe_{0.5}Te_{0.5}$ layer, which could result in the disordered alignment for the second layer $FeSe_{0.5}Te_{0.5}$ film. The T_c is lower than the epitaxial thin films on single crystal substrates that have a T_c^{onset} ranging from 12 K to 21 K [63, 109, 154, 160] and it is possibly due to the compositional variation at atomic scale.

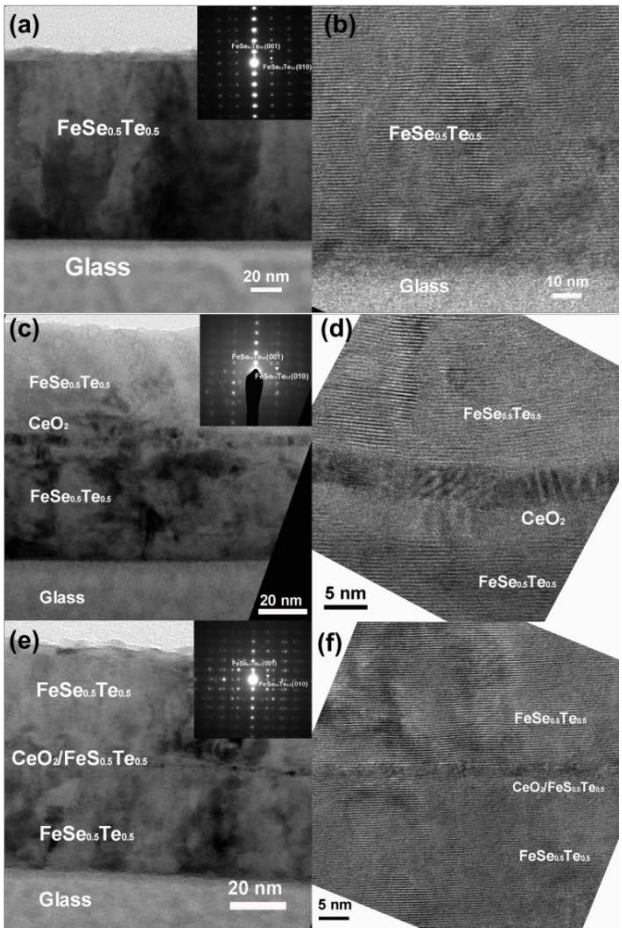

Figure 6. 3 (a) Cross-sectional TEM image with the corresponding SAED of single layer $FeSe_{0.5}Te_{0.5}$ film deposited on glass substrate and the high resolution cross-sectional TEM image is shown in (b). (c) Cross-sectional TEM image with the corresponding SAED of the $FeSe_{0.5}Te_{0.5}$ thin film with CeO_2 interlayer on glass substrate and the high resolution cross-sectional TEM image is shown in (d). (e) Cross-sectional TEM image with the corresponding SAED of the $FeSe_{0.5}Te_{0.5}$ thin film with $FeSe_{0.5}Te_{0.5}/CeO_2$ composite interlayer on glass substrate and the high resolution cross-sectional TEM image is shown in (f).

The cross-sectional TEM images in Figure 6. 3 show the microstructure analysis of all three samples. Figure 6. 3 (a) and (b) show the low magnification and high resolution TEM image of a pure $FeSe_{0.5}Te_{0.5}$ film on glass substrate. The inset in (a) is the corresponding diffraction pattern. The image demonstrates that the overall quality of the single layer film is high except some columnar grain structure. The grain boundary is across the entire film thickness. Figure 6. 3 (c) and (d) show the low magnification and high resolution TEM image of the film with a 7 nm CeO_2 interlayer. The interlayer introduced into the film may provide the platform for the second $FeSe_{0.5}Te_{0.5}$ layer. However, in the film with the CeO_2 interlayer, the CeO_2 did not grow on the $FeSe_{0.5}Te_{0.5}$ film with the perfect $FeSe_{0.5}Te_{0.5}$ *(001)* planes // CeO_2 *(001)* planes as in the epitaxial film [156], instead the CeO_2 turns out to be polycrystalline without long range order, which disrupts the second layer growth. Comparing to the film with the CeO_2 interlayer, the film with the $FeSe_{0.5}Te_{0.5}/CeO_2$ composite interlayer provides a very smooth platform for the second layer growth as shown in Figure 6. 3 (e) and (f). This interlayer fills the gap of the grain boundary from the first layer. In addition the top surface is smoother than the one with the CeO_2 interlayer. The a-b plane alignment of the second layer is much better than the first layer. From the diffraction patterns of the three films as inset in a, c and e respectively, the c-axis is aligned vertical to the substrate surface. However for the diffraction pattern corresponding to the a-b plane, there are extra diffraction dots suggesting some in-plane rotation of the grains in the films for all three cases. The film is in-plane textured however it is relatively local comparing to the film grown on single crystal substrates.

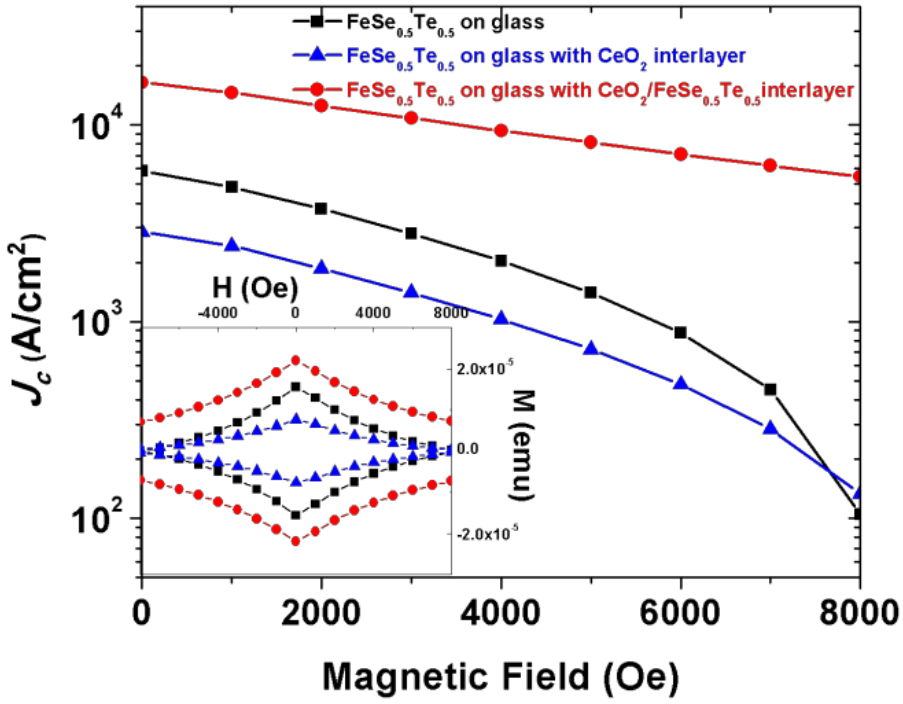

Figure 6. 4 (a) M-H loops of the pure $FeSe_{0.5}Te_{0.5}$ thin film, $FeSe_{0.5}Te_{0.5}$ thin film with CeO_2 interlayer and $FeSe_{0.5}Te_{0.5}$ thin film with $FeSe_{0.5}Te_{0.5}/CeO_2$ composite interlayer on glass substrates. (b) The calculated critical current densities for the pure $FeSe_{0.5}Te_{0.5}$ thin film, $FeSe_{0.5}Te_{0.5}$ thin film with CeO_2 interlayer and $FeSe_{0.5}Te_{0.5}$ thin film with $FeSe_{0.5}Te_{0.5}/CeO_2$ composite interlayer on glass substrates.

Both the self-field and in-field critical current density values (J_c^{sf} and $J_c^{in\text{-}field}$ (H//c)) were measured under the applied magnetic field of 0 T ~ 1 T at 2 K by VSM in the PPMS. Here the moment versus magnetic field (M-H) hysteresis loops are shown in Figure 6. 4. For the VSM measurement the critical current densities were derived by the Bean model:

$$\boldsymbol{J_c = \frac{20\Delta M}{a(1-a/3b)}} \quad \text{(Equation 6. 1)}$$

where ΔM is the opening in the hysteresis loop; a and b are the sample dimensions. Bean model gives a reasonable estimation of the actual J_c value for the moderate

magnetization change in the testing range [59, 65]. The calculated self-field current densities at 2 K for the film with the composite interlayer, the pure film and the film with CeO_2 interlayer are 1.6×10^4 A/cm^2, 5.8×10^3 A/cm^2 and 2.9×10^3 A/cm^2, respectively. Compared to the previous report [162] on the $FeSe_{0.5}Te_{0.5}$ wires by PIT technique, the critical current density is much higher for all of these three film configurations. Comparing these three film configurations, the J_c values are largely varied and the critical current density variation is possibly due to the grain boundary effect, i.e., the high density of large angle boundaries block the current flow in the superconductor. The enhancement in the case of the $FeSe_{0.5}Te_{0.5}/CeO_2$ composite interlayer results from the good film quality and better alignment of the a-b plane confirmed by the TEM result. However for the case of CeO_2 interlayer film, due to the polycrystalline CeO_2, the second $FeSe_{0.5}Te_{0.5}$ layer growth was disrupted without a good a-b plane alignment. This is also confirmed by the XRD results where the peak split and widening were observed. The superconducting properties could therefore be deteriorated by misaligned lattice planes, similar to the case in cuprates as well as iron pnictides [121]. It is noted that the film with the CeO_2 interlayer begins to show a higher critical current density under 0.8 T compared to the pure film possibly because of the flux pinning from the misfit dislocations formed between the interlayer and the $FeSe_{0.5}Te_{0.5}$ film. The growth of $FeSe_{0.5}Te_{0.5}$ films on glass substrates demonstrates a low cost method for processing iron-based superconductor on low cost substrates such as glass and amorphous buffered metal tapes. In addition, further work shall be considered to

achieve a smooth growth condition regardless of the substrate or the interlayer texture or the atomic scale arrangement, and to minimize the film-substrate/interface interaction.

6.5 Conclusion

In conclusion, $FeSe_{0.5}Te_{0.5}$ films, in single layer form, with CeO_2 interlayer and $FeSe_{0.5}Te_{0.5}$ films with $FeSe_{0.5}Te_{0.5}/CeO_2$ composite interlayer were grown on glass substrates with high *c*-axis texturing. The superconducting transition temperature is around 6 K. The critical current density at 2 K is around 1.6×10^4 A/cm^2 for the optimized film structure with the $FeSe_{0.5}Te_{0.5}/CeO_2$ composite interlayer. With further optimization on the growth condition to increase the in-plane texture, the superconducting properties could be further enhanced for future iron-based superconductor coated conductors.

CHAPTER VII

SUPERCONDUCTING PROPERTIES OF IRON CHALCOGENIDE CLOSE TO AFM ORDERING

7.1 Overview

In this study the Te rich iron chalcogenide thin film with composition close to the AFM ordering has been demonstrated. Compared to the optimum composition $FeSe_{0.5}Te_{0.5}$ according to the literature report, the $FeSe_{0.1}Te_{0.9}$ is even more promising for the high field application with its high upper critical field and high critical current density at the same time.

7.2 Introduction

The iron chalcogenide demonstrates the interplay of structure, magnetism and superconductivity; the end-member FeSe and FeTe have quite different physical properties although with a similar crystal structure. FeSe exhibits metallic behavior in the normal state and has a T_c^{onset} of 13 K [27]. FeSe film and the composition close to the FeSe end will experience a structure transition tetragonal to orthorhombic at low temperature described as distortion in the xrd result by Wang *et al.* [54] which is important to the superconducting transition. The transition may be suppressed by the substrate confinement such as thin film on MgO, STO and LAO substrate with square thin film growth template (a = b) which will suppress the superconducting transition.

FeTe used to be predicted the iron chalcogenide with highest transition temperature [60], however FeTe exhibits AFM ordering around 70K along with a

structural transition from tetragonal to monoclinic where the anomaly appears in the resistivity vs. temperature curve, and does not show superconductivity. [73]

So the $FeSe_{1-x}Te_x$ epitaxial thin film with compositions far away from the FeSe side without the orthorhombic transition at low temperature and close to the FeTe without the monoclinic transition at low temperature [75] may have better superconducting properties.

The high quality epitaxial thin film is an ideal template to do comparison study with the theoretical calculation. Compared to the bulk materials the epitaxial FeTe superconducting thin films have been demonstrated by strain effect [103] and oxygen incorporation [104, 105]. The Se or S can be covalently doped in FeTe to suppress the AFM state from long range to short range to induce the superconducting transition. [75] The bulk materials already been studied for tellurium substitution effect [27, 72, 73].

In this research Te riched targets of FeTe, $FeSe_{0.1}Te_{0.9}$ and $FeSe_{0.5}Te_{0.5}$ was synthesized for a systematic study for the thin films. Here we demonstrate the Te rich iron chalcogenide may have even better superconducting properties than the $FeSe_{0.5}Te_{0.5}$ which is commonly thought to be the one with the best properties [73]. Upon small amount of Se doping into the FeTe, high J_c comparable to the optimized composition $FeSe_{0.5}Te_{0.5}$ and extremely high H_{c2} comparable to the FeTe : O_x [104] were achieved. The $FeSe_{0.1}Te_{0.9}$ thin film can be also grown on amorphous substrate such as glass substrate a in a highly textured layer by layer fashion with high performance. And the FeTe used to be considered as non-superconducting phase in bulk form is grown into

thin films on various substrates including the glass substrate with superconducting properties.

7.3 Experimental

$FeSe_{0.5}Te_{0.5}$, $FeSe_{0.1}Te_{0.9}$ and FeTe targets were prepared by a standard solid-state reaction method with appropriate stoichiometric mixture of the Fe, Se and Te powders. The pure $FeSe_{1-x}Te_x$ (x = 0.5, 0.9 and 1) thin films were deposited at 400 °C on single crystal STO (001) substrates and glass substrate in a PLD system with KrF excimer laser (Lambda Physik Compex Pro 205, λ = 248nm, 5Hz). During deposition, the target-substrate distance was kept at 4.5 cm. The growth rate of the $FeSe_{1-x}Te_x$ is around 0.5 Å/pulse. The laser power density was 3 J/cm^2. The base pressure for all the depositions was around 10^{-6} Torr in vacuum. The total thickness of the $FeSe_{0.5}Te_{0.5}$ thin films was kept around 100 nm.

The microstructure of the films was characterized by X-ray diffraction (XRD) (Panalytical XPert X-ray diffractometer and BRUKER D8 powder X-ray diffractometer), transmission electron microscopy (TEM). The superconducting properties were characterized using resistivity-temperature (R-T) measurement by a four point probe method from 2 K to 300 K in a physical property measurement system (PPMS, Quantum Design). Both the self-field and in-field critical current density (J_c^{sf} and $J_c^{in\text{-}field}$ (H // c)) were measured under the applied magnetic field of 0 T ~ 7 T at various temperatures by the vibrating sample magnetometer (VSM) in the PPMS.

7.4 Results and Discussion

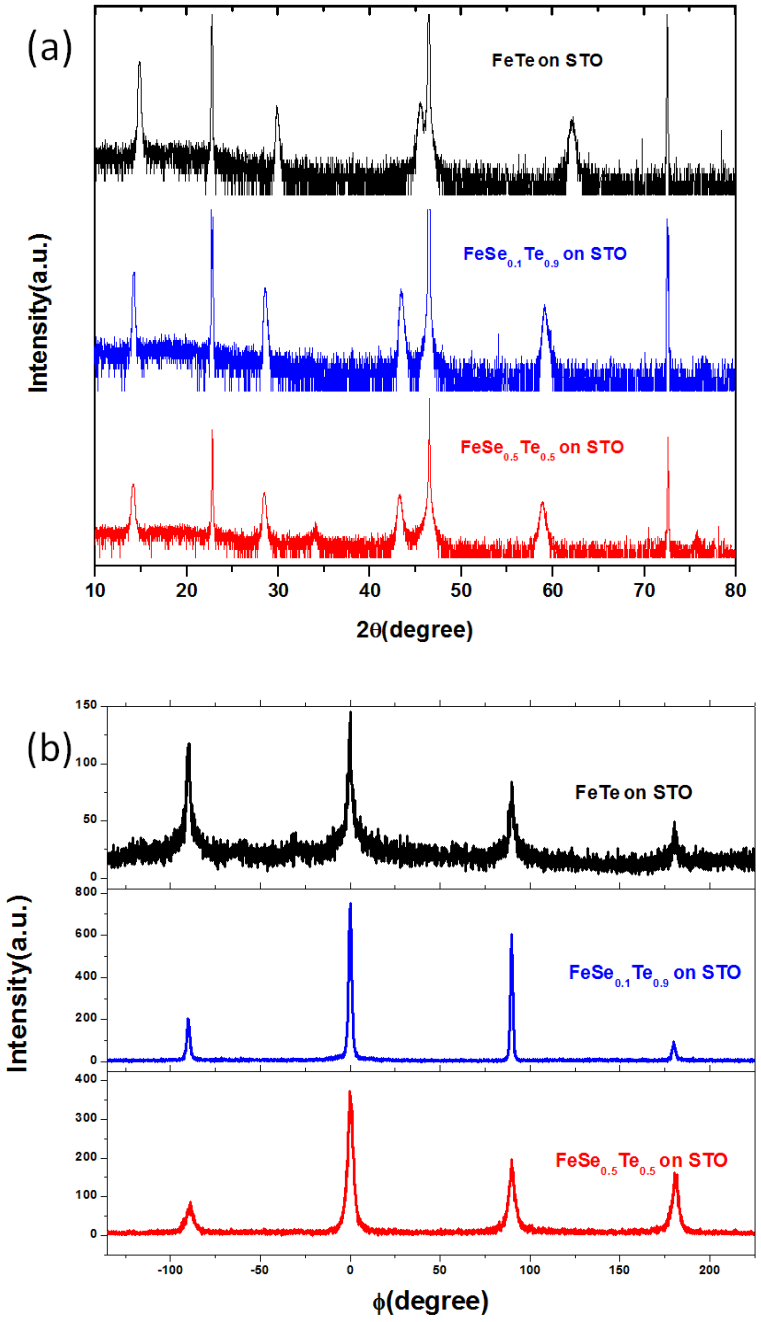

Figure 7. 1 XRD plots of the single layer $FeSe_{0.5}Te_{0.5}$, $FeSe_{0.1}Te_{0.9}$ and FeTe thin films on STO substrates. (a) θ-2θ scan. (b) φ scan of the $FeSe_{1-x}Te_x$ (112) peak.

Figure 7. 1 (a) shows the standard θ-2θ XRD scans for the $FeSe_{0.5}Te_{0.5}$, $FeSe_{0.1}Te_{0.9}$ and FeTe films deposited on the STO substrates. All the $FeSe_xTe_{1-x}$ films are determined to be tetragonal phase without impurity phase and highly textured along $FeSe_xTe_{1-x}$ (00*l*) on STO (001). With increasing Te concentration the c axis parameter becomes larger and the c-axis lattice parameters for the $FeSe_{0.5}Te_{0.5}$, $FeSe_{0.1}Te_{0.9}$ and FeTe films are 5.9615 Å, 6.1851 Å and 6.2585 Å, respectively. Figure 7. 1 (b) shows the φ scan of the $FeSe_{1-x}Te_x$ (112) peak. The four sharp peaks indicate the in plane texture for the thin films. The full width at half maximums (FWHM) for the $FeSe_{0.5}Te_{0.5}$, $FeSe_{0.1}Te_{0.9}$ and FeTe are 3.7°, 1.9° and 5.3° respectively. The in plane alignment for the FeTe film is not as good as the doped one with the FeSe framework. Notice the $FeSe_{0.1}Te_{0.9}$ has even a better in plane texture than the $FeSe_{0.5}Te_{0.5}$ thin film.

The cross-section TEM images in Figure 7. 2 (a) and (b) both present the *c*-planes are parallel to the glass surface with excellent film quality. High resolution image along the film-substrate interface shows obvious film lattices and the clean film-substrate interface. The film thickness is around 100 nm. The film quality is comparable to the $FeSe_{0.5}Te_{0.5}$ thin film on STO substrate we reported before [156]. The *c*-axis parameter and *ab* plane lattice parameter are calculated to be 6.1721 Å and 3.8519 Å according to the diffraction pattern. The *c*-axis parameter is consistent with the XRD result. Compared to the previous bulk $FeSe_{0.1}Te_{0.9}$ with $c \sim 6.2136$ Å and $a \sim 3.8175$ Å [72], the unit cell volume almost remain the same. It is similar to the FeTe thin film on STO substrate which was ready to change shape to accommodate the mismatch between the interface [103].

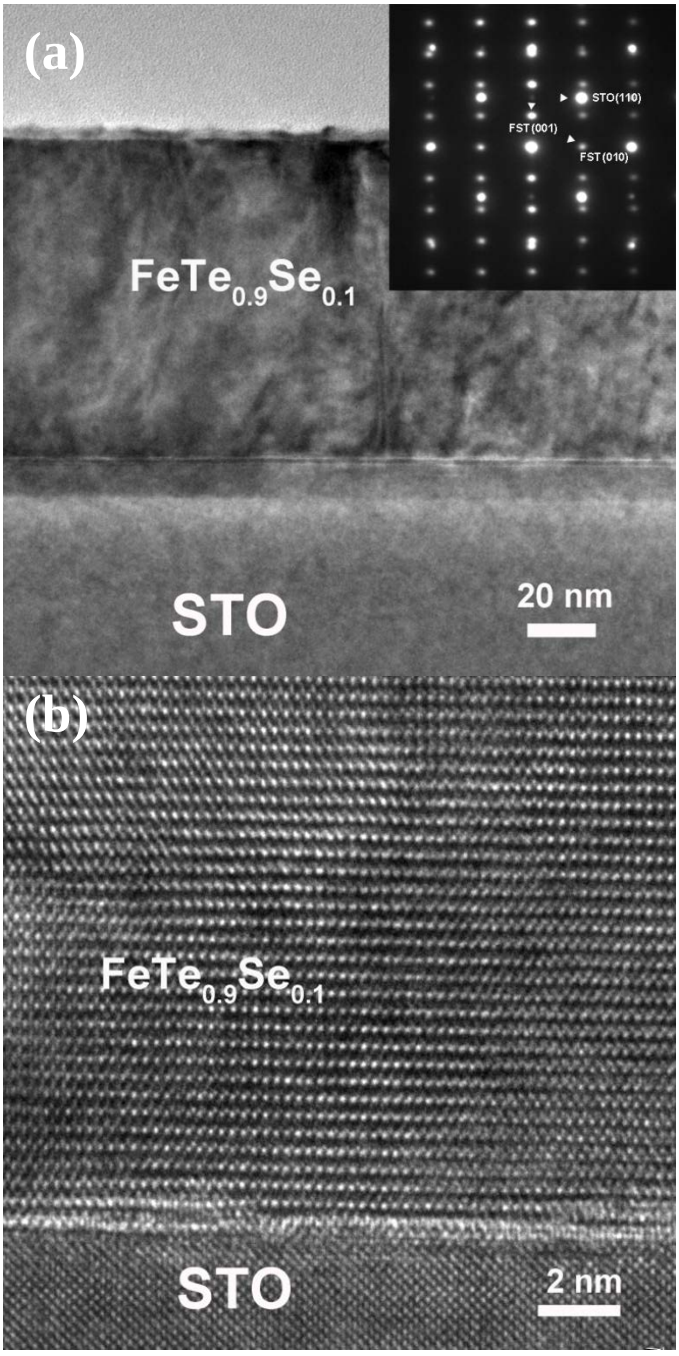

Figure 7. 2 TEM results for (a) low magnification cross-section overview with inset showing the SAED for the film with substrate, (b) high resolution cross-section view for at $FeSe_{0.1}Te_{0.9}$ thin film on STO substrate.

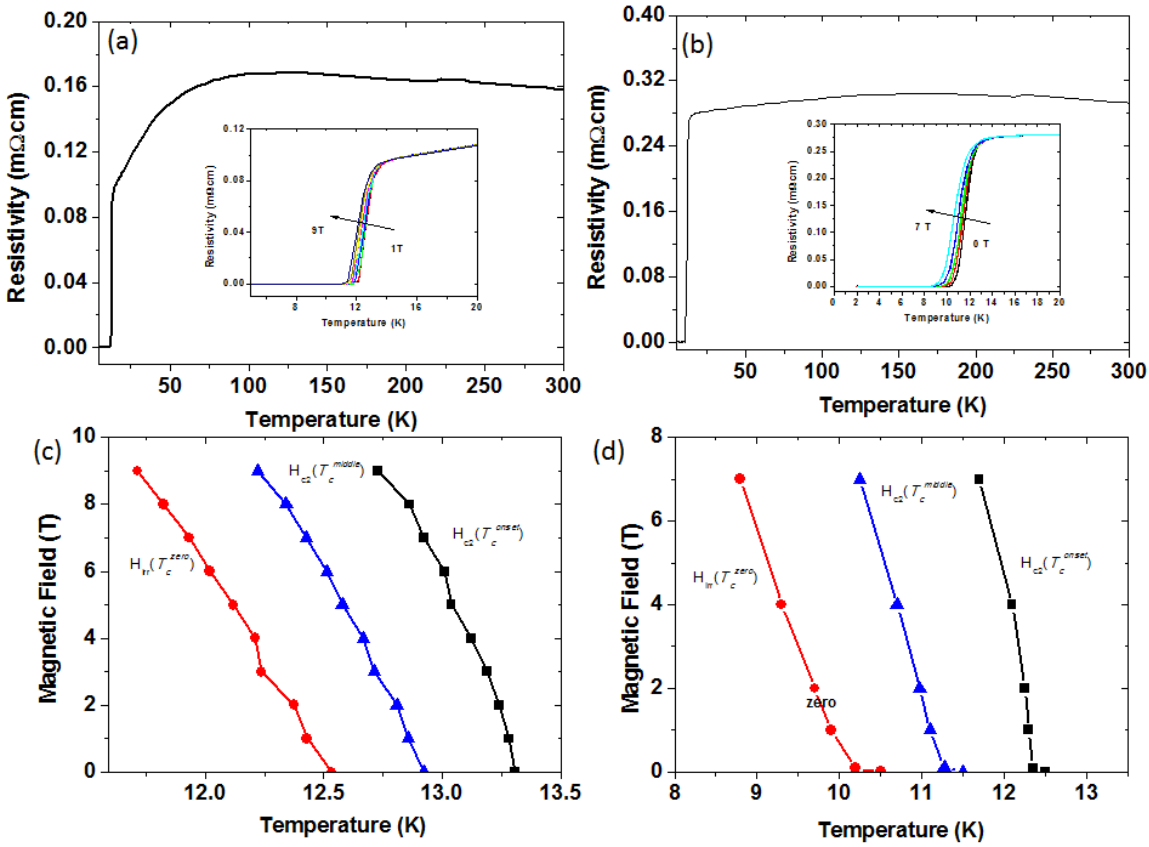

Figure 7. 3 (a) and (b) show the R-T plots of the $FeSe_{0.1}Te_{0.9}$ and $FeSe_{0.5}Te_{0.5}$ thin films on STO from 2 K to 300 K. The insets of (a) and (b) show the detailed superconducting transition regime from 2 K to 20 K under magnetic field. The estimations of H_{irr} and the H_{c2} are shown in (c) and (d) for $FeSe_{0.1}Te_{0.9}$ and $FeSe_{0.5}Te_{0.5}$, respectively.

R-T measurements (2 K-300 K) were conducted for $FeSe_{0.1}Te_{0.9}$ and $FeSe_{0.5}Te_{0.5}$ films on STO and the results are plotted in Figure 7. 3. The details from 2 K to 20 K are shown in the inset of (a) and (b). The $FeSe_{0.5}Te_{0.5}$ film shows a transition temperature T_c ranging from ~12.5 K (T_c^{onset}) to ~ 10.5 K (T_c^{zero}). In comparison the $FeSe_{0.1}Te_{0.9}$ has a higher transition temperature T_c ranging from ~13.3 K (T_c^{onset}) to ~ 12.5 K (T_c^{zero}) which is also higher than its bulk counterpart [72, 73]. The R-T measurement under magnetic field parallel to the *c*-axis up to 9 T was carried out to estimate the upper critical field.

The irreversibility line $H_{irr}(T)$ extrapolated with the T_c^{zero} and the upper critical field $H_{c2}(T)$ extrapolated with the middle point of T_c [55, 101] are plotted. The upper critical field was estimated by the Werthamer-Helfand-Hohenberg model,

$$-H_{c2}(0) = 0.7T_c \, dH_{c2}/dT \,|T_c \quad \text{(Equation 7. 1)}$$

The upper critical field H_{c2} is estimated to be ~ 49 T and 114 T for the $FeSe_{0.5}Te_{0.5}$ and $FeSe_{0.1}Te_{0.9}$ film respectively. The H_{c2} is much higher in $FeSe_{0.1}Te_{0.9}$ and the value is comparable to the pure superconducting FeTe thin films [104] deposited in controlled oxygen atmosphere. The vacuum deposited $FeSe_{0.1}Te_{0.9}$ is easier to get reproducible result for the magnets application in terms of homogeneity and deposition condition control.

Notice the $FeSe_{0.1}Te_{0.9}$ shows smaller normal state resistivity compared to the $FeSe_{0.5}Te_{0.5}$. Another feature of $FeSe_{0.1}Te_{0.9}$ is the abnormal in the R-T plot usually reported at around 70K for bulk and thin film [134] which indicates the AFM state becomes broader hump at temperature higher than 100 K. The phase separation used to be proposed in the FeTe thin film deposited in controlled oxygen atmosphere with minor amount of oxygen doping [134]. The intrinsic chemical inhomogeneity was reported in $Fe_{1+y}Se_{1-x}Te_x$ study by STEM [163] and this nanoscale phase separation of the Te rich or Te deficient clusters are possible flux pinning centers to enhance the in-field J_c and the pinning force [156]. In case of $FeSe_{0.1}Te_{0.9}$, it is highly possible that point defects of the Te rich regions as parent compound, being AFM can work as the flux pinning centers which yield high upper critical field. Better pinning properties are expected upon further optimize the composition to get more self-assembled pinning centers [114].

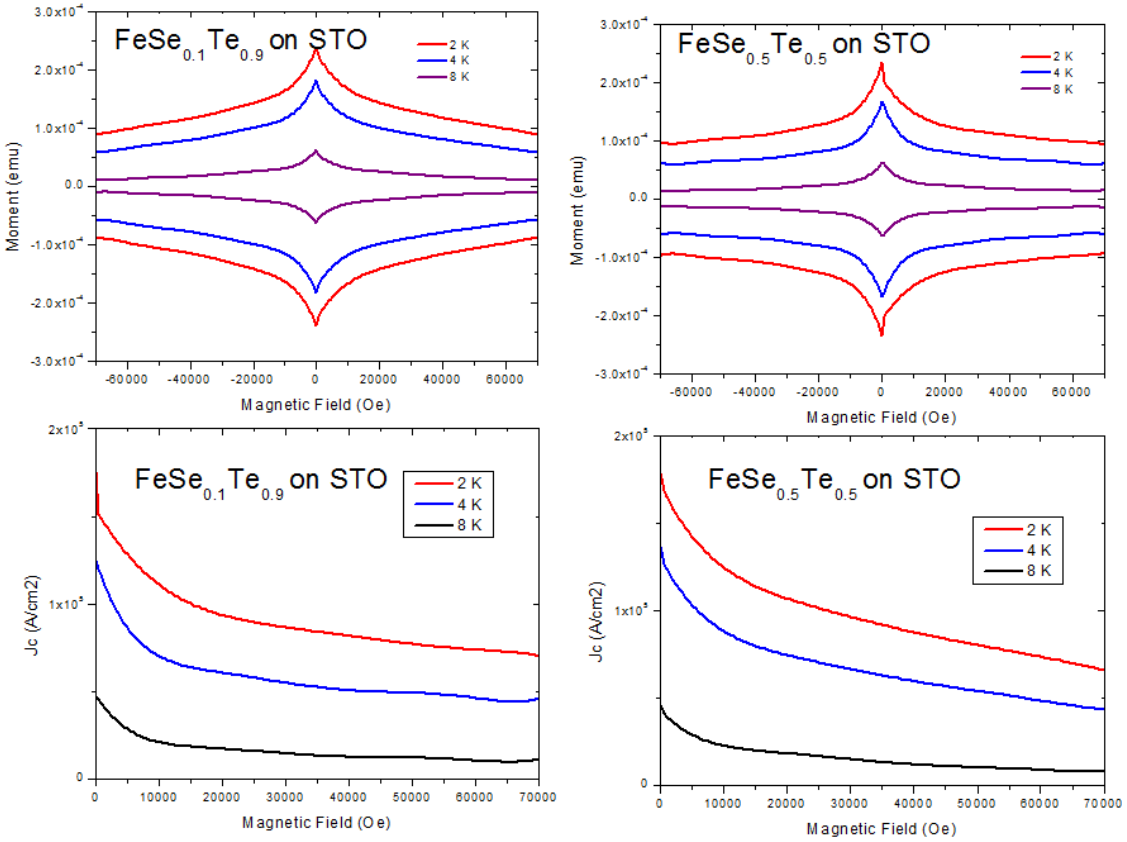

Figure 7. 4 Magnetic hysteresis loops of the $FeSe_{0.5}Te_{0.5}$ and $FeSe_{0.1}Te_{0.9}$ thin films at 2 K, 4 K and 8 K. The corresponding field dependence of the critical current density for $FeSe_{0.5}Te_{0.5}$ and $FeSe_{0.1}Te_{0.9}$ thin films at (d) 2 K, (e) 4 K and (f) 8 K. The insets show the normalized critical current density plots in log-log scale for α value calculation.

The magnetic hysteresis loops measured with the magnetic field parallel to the *c*-axis of the thin films are compared in Figure 7. 4 for the $FeSe_{0.5}Te_{0.5}$ and $FeSe_{0.1}Te_{0.9}$ thin films. There is no obvious fishtail shape in the hysteresis loops for all the samples. The fishtail shape was reported in the bulk $FeSe_{0.5}Te_{0.5}$ and is correlated to the existence of a weak or non-superconducting phase [58, 59]. This suggests the films are free from those weak or non-superconducting phases. The critical current densities were derived by the Bean model which gives a reasonable estimation of the actual J_c value for the

moderate magnetization change in the testing range [58, 59, 65]. The calculated J_c values are plotted in Figure 7. 4 for 2 K, 4 K and 8 K, respectively. Self-field J_c is as high as 1.8×10^5 A/cm^2 at 2 K, 1.3×10^5 A/cm^2 at 4 K and 0.5×10^5 A/cm^2 at 8 K for both $FeSe_{0.5}Te_{0.5}$ and $FeSe_{0.1}Te_{0.9}$ thin films.

For the pure FeTe thin film we first tried deposited the tetragonal FeTe thin films on STO substrates. By varying the deposition temperature, we optimized the growth condition with the R-T measurement shown in Figure 7. 5. The corresponding XRD plot is shown in Figure 7. 6. Higher superconducting transition temperature was found in the film deposited at 350 °C with much pure tetragonal phase indicated by the XRD results.

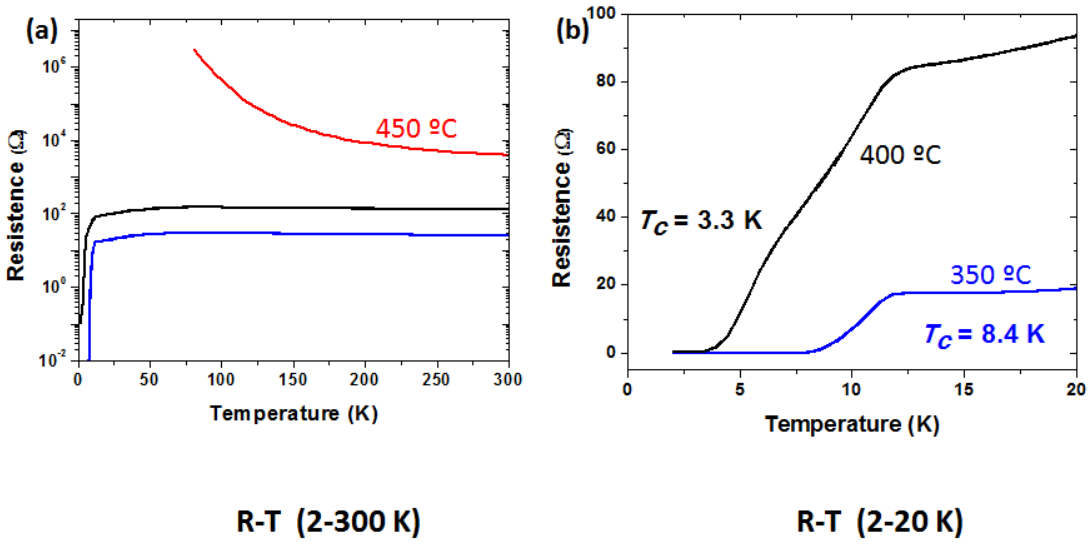

Figure 7. 5 R-T plot of the FeTe thin films grown on STO substrates with various deposition temperatures.

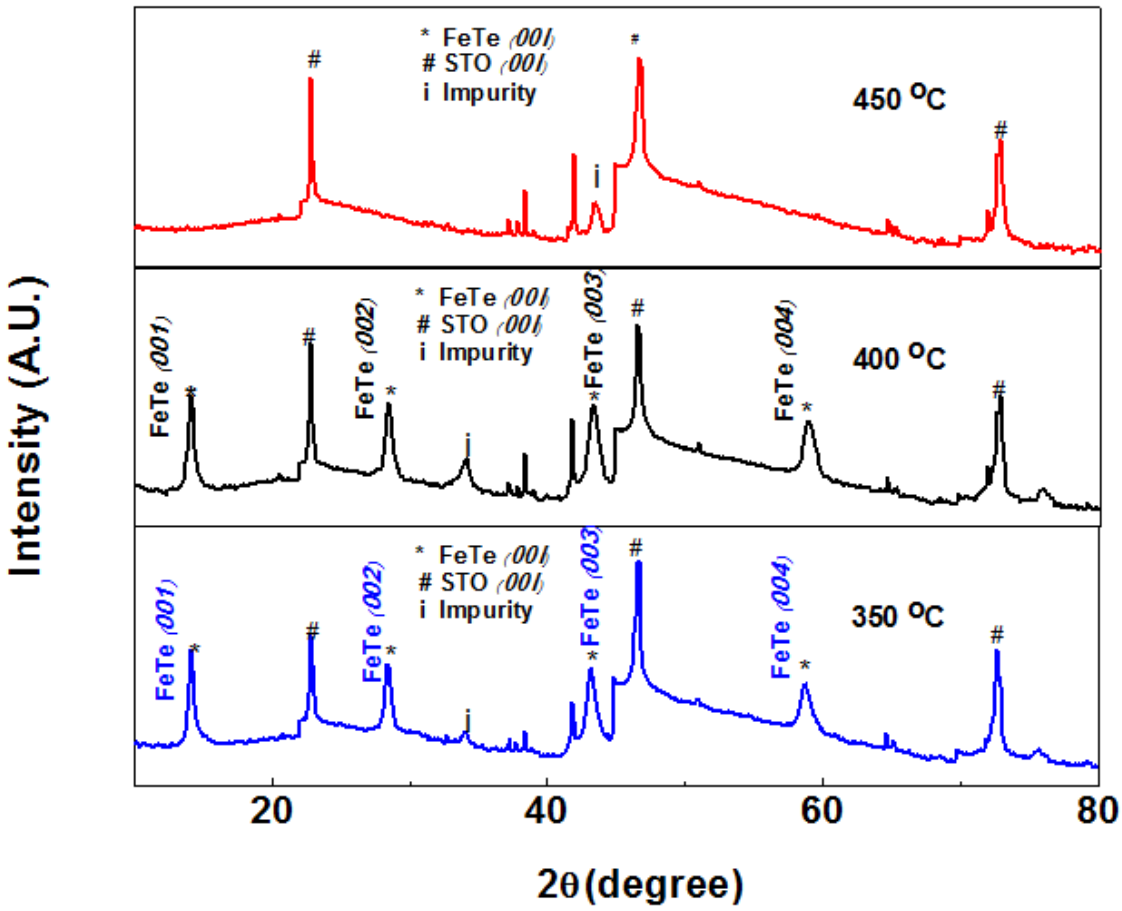

Figure 7. 6 XRD plot of the FeTe thin films grown on STO substrates with various deposition temperatures

To test the compatibility of the iron chalcogenide thin film with the coated conductor technology, the $FeSe_{1-x}Te_x$ thin film has also been deposited on glass substrate. Figure 7. 7 shows the standard θ-2θ XRD scans for the $FeSe_{0.5}Te_{0.5}$, $FeSe_{0.1}Te_{0.9}$ and FeTe films deposited on the glass substrates. All the $FeSe_{1-x}Te_x$ films are determined to be highly textured along the c axis of the tetragonal phase $FeSe_{1-x}Te_x$ (00*l*). However in the FeTe there is one extra peak corresponding to the impurity. The c-

axis lattice parameters for the $FeSe_{0.5}Te_{0.5}$, $FeSe_{0.1}Te_{0.9}$ and FeTe films are 5.8851 Å, 6.1691 Å and 6.2732 Å, respectively.

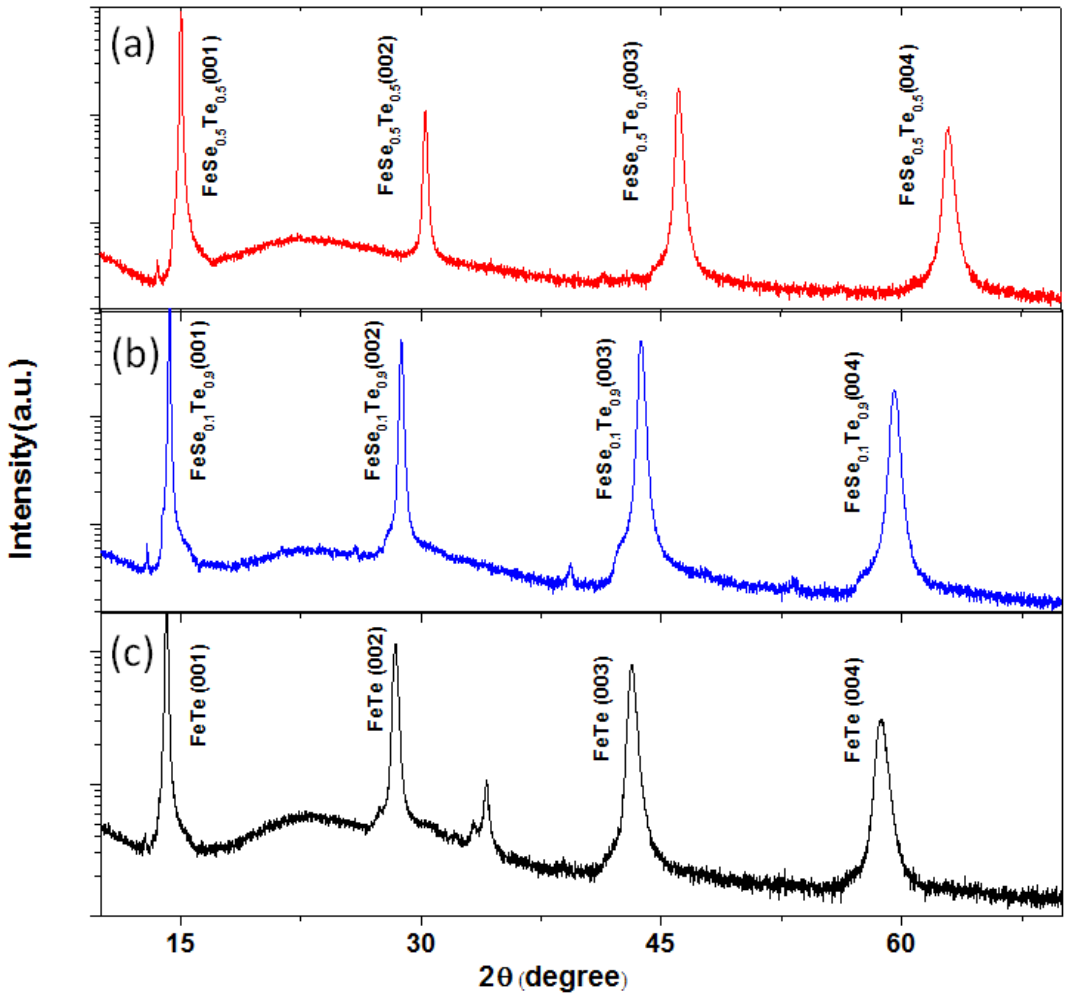

Figure 7. 7 θ-2θ scans of the $FeSe_{0.5}Te_{0.5}$, $FeSe_{0.1}Te_{0.9}$ and FeTe thin films on glass substrates.

The Figure 7. 8 shows the $FeSe_{0.1}Te_{0.9}$ thin films on glass substrate. Surprisingly the R-T measurement shows the $FeSe_{0.1}Te_{0.9}$ thin films on glass substrates have even higher transition temperature of T_c^{zero} ~ 10 K than the $FeSe_{0.5}Te_{0.5}$ thin films on glass substrates.

In addition, the H_{c2} estimated by the R-T measurement under magnetic field is much higher than the $FeSe_{0.5}Te_{0.5}$ thin films on glass substrates. This result demonstrates the possibility for the practical application of the $FeSe_{0.1}Te_{0.9}$ thin films in the coated conductors.

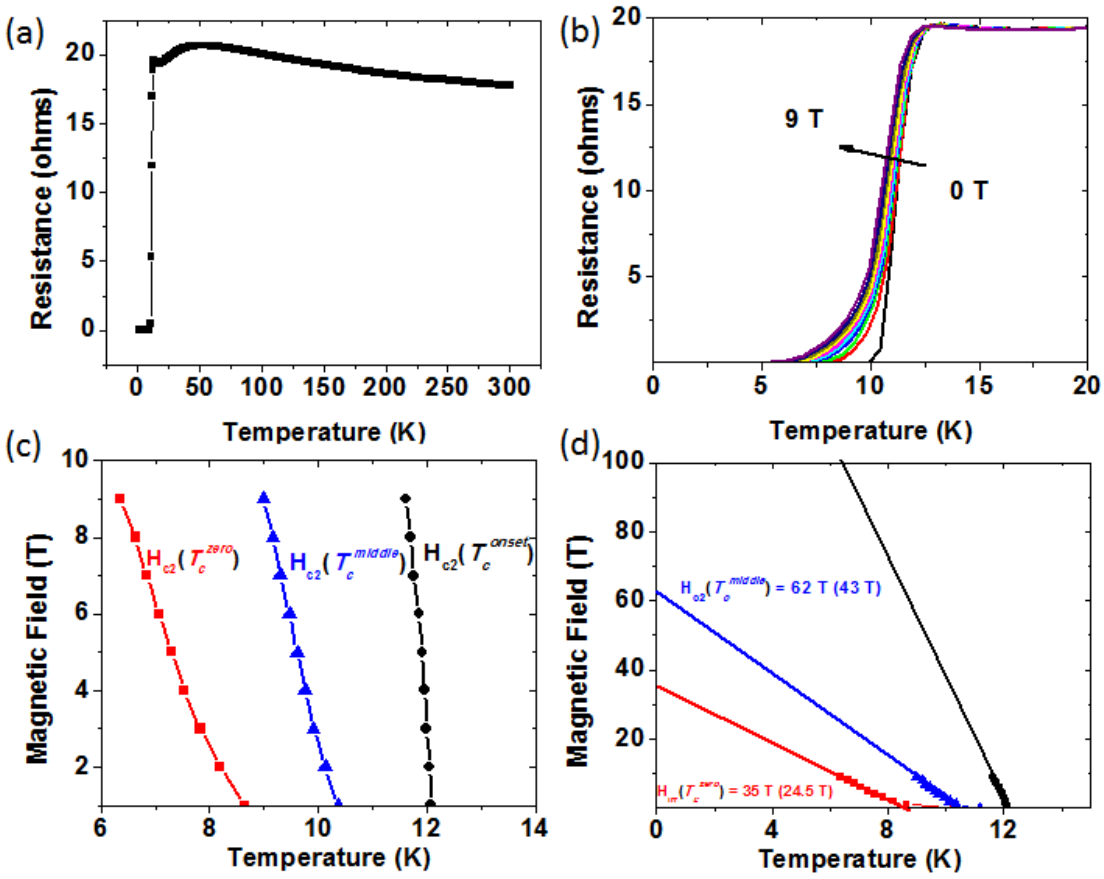

Figure 7. 8 (a) R-T plots of the $FeSe_{0.1}Te_{0.9}$ on glass substrate from 2 K to 300 K. (b) shows the detailed superconducting transition regime from 2 K to 20 K under magnetic field. (c) and (d) are the estimations of H_{irr} and the H_{c2}.

And even the pure FeTe thin films on glass substrates can show the superconducting transition. The R-T measurement shows pure FeTe film on glass

substrate with transition temperature of 8 K for the zero resistance and the T_c^{onset} is ~ 12 K. In addition in the R-T plot the bump corresponding to the AFM transition is presented. It indicates the coexistence of the superconducting phase and the AFM phase. In addition the increasing of the resistance just before the superconducting transition is discovered, which is similar to the FeTe thin film grown on STO substrate in the controlled oxygen atmosphere [104]. The results indicate the substrate may not be the key for the FeTe to be superconductor.

The TEM of the FeTe thin film on glass substrate is as shown in Figure 7. 10. Although the film has some texture properties as shown in the XRD plot in Figure 7. 7 the epitaxial quality is not as good as the doped one.

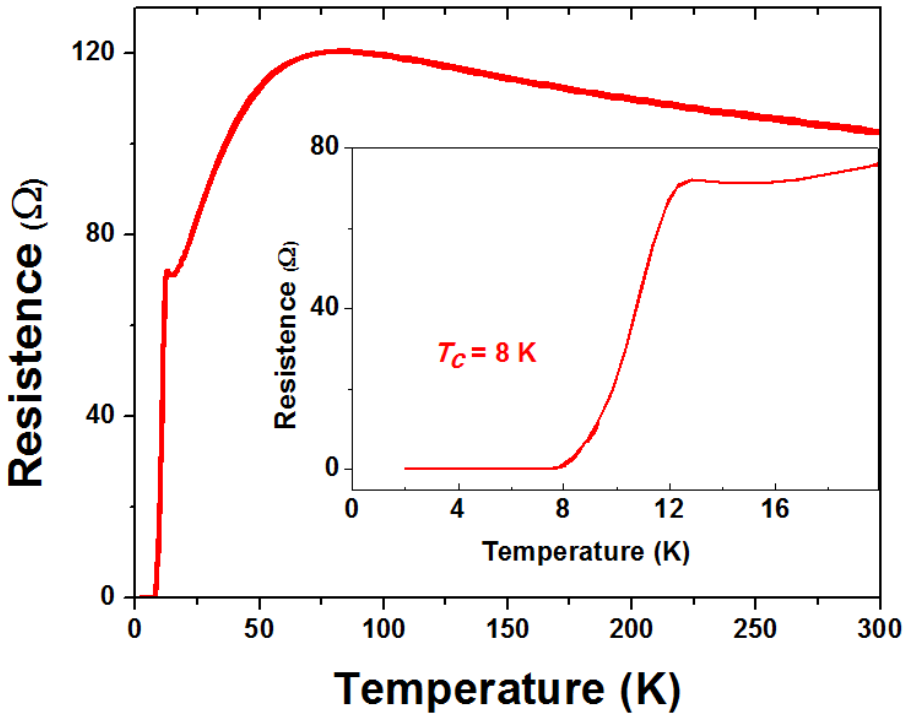

Figure 7. 9 R-T plot of the FeTe thin film on glass substrate from 2 to 300 K and the inset shows the detail of the superconducting transition from 2 to 20 K.

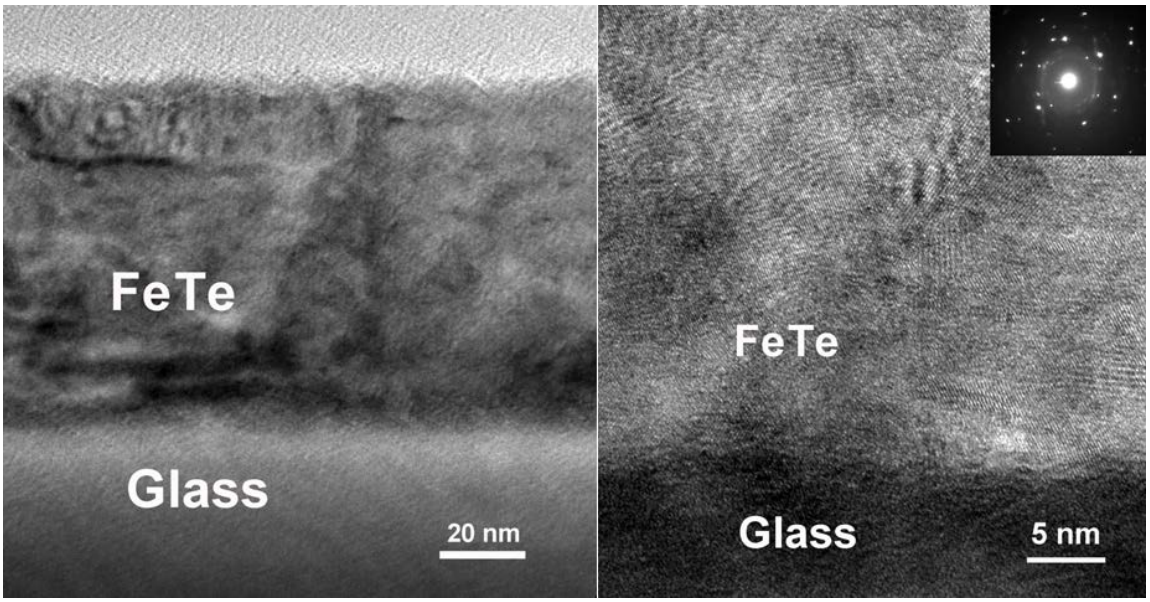

Figure 7. 10 TEM results for (a) low magnification cross-section overview, (b) high resolution cross-section view for at FeTe thin film on glass substrate with inset showing the SAED for the film.

7.5 Conclusion

In this research we have successfully grown epitaxial superconducting $FeSe_{0.5}Te_{0.5}$, $FeSe_{0.1}Te_{0.9}$ and FeTe thin films on STO and glass substrates. The $FeSe_{0.1}Te_{0.9}$ on STO has a transition temperature T_c ranging from ~13.3 K (T_c^{onset}) to ~ 12.5 K (T_c^{zero}) with H_{c2} of ~ 114 T which is comparable to the superconducting FeTe thin film and much higher than the $FeSe_{0.5}Te_{0.5}$ thin films on STO. The $FeSe_{0.1}Te_{0.9}$ on glass substrate also demonstrates higher T_c and H_{c2} compared to the $FeSe_{0.5}Te_{0.5}$ film on glass substrate. All these results show the iron chalcogenide superconducting thin film with composition close to the magnetic order is more promising in the high field applications.

CHAPTER VIII

SUMMARY AND FUTURE WORK

In this dissertation, we systematically investigated the growth conditions and the superconducting properties of the iron chalcogenide thin films with various compositions on various substrates:

We first optimized pure FeSe thin films by different growth conditions using pulsed laser deposition (PLD) and post-annealing procedures. The annealing procedure which introduces the Fe_3O_4 is important for the superconducting properties: First it consumes the extra Fe due to the high vapor pressure of the Se during the PLD. In addition, annealing can improve the crystallinity.

Later on, we reported our initial attempt on introducing the flux pinning centers in $FeSe_{0.5}Te_{0.5}$ either under a controlled oxygen atmosphere or with a thin CeO_2 interlayer. The oxygen deposited thin film gives moderate improvement. The thin film with the CeO_2 interlayer shows notable improvement in the pinning property. The enhancement may originate from the nanoclusters as well as the interfacial defects introduced by the heterogeneous interface.

Towards the practical application, we demonstrated the growth of superconducting $FeSe_{0.5}Te_{0.5}$ film on amorphous glass substrates for the first time. The film is highly textured with excellent superconducting properties, e.g., T_c of 10 K and J_c under self-field as high as 1.2×10^4 A/cm^2 at 4 K. Further optimization of the film growth with various nanoscale interlayers has been carried out.

In addition the Te rich iron chalcogenide thin film with composition close to the composition with Antiferromagnetic (AFM) transition has been demonstrated. Compared to the $FeSe_{0.5}Te_{0.5}$ which was claimed to be the optimum composition from the literature report, the $FeSe_{0.1}Te_{0.9}$ is even more promising as the candidate to substitute conventional materials used in the high field applications such as Nb_3Sn and NbTi.

The future research can be focused on these aspects:

1. Find the optimum composition for the high field application: couple the superconducting properties including T_c, J_c and H_{c2}.
2. Further enhance the in-field performance of the iron chalcogenide thin films by interlayer approach and study the pinning mechanism with the vertical aligned nanocomposite (VAN) layer such as CeO_2/Fe_2O_3 [164].
3. Use the piezoelectric buffer layer to control the lattice parameters which assemble the pressure effect to tune the superconducting properties of the iron chalcogenide thin films.
4. Study the stability of the thin film at environment similar to the situation in the practical application such as the sensitivity of the superconducting properties to the air, creep effect of the film in the coated conductor during thermal cycle and the mechanical properties of the film such as the scratch test and indentation.

REFERENCES

[1] C. P. Poole, H. A. Farach, and R. J. Creswick, "Superconductivity," ed. San Diego, CA, USA: Academic Press, 1995.

[2] H. K. Onnes, "Further experiments with liquid helium D - On the change of the electrical resistance of pure metals at very low temperatures, etc V The disappearance of the resistance of mercury," *P K Akad Wet-Amsterd,* vol. 14, pp. 113-115, 1911.

[3] W. Meissner and R. Ochsenfeld, "Short initial announcements.," *Naturwissenschaften,* vol. 21, pp. 787-788, 1933.

[4] M. Tinkham, *Introduction to Superconductivity, Second Edition.* New York, NY: McGraw Hill 1996.

[5] V. L. Ginzburg and D. A. Kirzhnits, *High-Temperature Superconductivity*. New York, USA: Consultants Bureau, 1982.

[6] I. Guillamon, H. Suderow, A. Fernandez-Pacheco, J. Sese, R. Cordoba, J. M. De Teresa, M. R. Ibarra, and S. Vieira, "Direct observation of melting in a two-dimensional superconducting vortex lattice," *Nat Phys,* vol. 5, pp. 651-655, 2009.

[7] J. G. Bednorz and K. A. Muller, "Possible High-Tc Superconductivity in the Ba-La-Cu-O System," *Z Phys B Con Mat,* vol. 64, pp. 189-193, 1986.

[8] M. K. Wu, J. R. Ashburn, C. J. Torng, P. H. Hor, R. L. Meng, L. Gao, Z. J. Huang, Y. Q. Wang, and C. W. Chu, "Superconductivity at 93 K in a new mixed-phase Y-Ba-Cu-O compound system at ambient pressure," *Phys Rev Lett,* vol. 58, pp. 908-910, 1987.

[9] DOE Report, "http://energy.gov/sites/prod/files/oeprod/DocumentsandMedia/Albany__03_05_08.pdf."

[10] C. Buzea and T. Yamashita, "Review of the superconducting properties of MgB2," *Supercond. Sci. Technol.,* vol. 14, pp. R115-R146, 2001.

[11] S. Yamanaka, H. Kawaji, K. Hotehama, and M. Ohashi, "A new layer-structured nitride superconductor. Lithium-intercalated beta-zirconium nitride chloride, LixZrNCl," *Adv Mater,* vol. 8, pp. 771-&, 1996.

[12] S. Yamanaka, K. Hotehama, and H. Kawaji, "Superconductivity at 25.5 K in electron-doped layered hafnium nitride," *Nature,* vol. 392, pp. 580-582, 1998.

[13] L. M. Kahn and J. Ruvalds, "Structure and Superconductivity in Alkali Tungsten Bronzes," *Phys Rev B,* vol. 19, pp. 5652-5660, 1979.

[14] Z. Barkay, E. Grunbaum, G. Leitus, and S. Reich, "Study of the superconducting Cs-doped WO3 crystal surface by electron backscattered diffraction," *J. Supercond. Novel Magn.,* vol. 21, pp. 145-150, 2008.

[15] S. Reich, G. Leitus, Y. Tssaba, Y. Levi, A. Sharoni, and O. Millo, "Localized high-T-c superconductivity on the surface of Na-doped WO3," *J. Supercond.,* vol. 13, pp. 855-861, 2000.

[16] K. Ishida, Y. Nakai, and H. Hosono, "To What Extent Iron-Pnictide New Superconductors Have Been Clarified: A Progress Report," *J Phys Soc Jpn,* vol. 78, 2009.

[17] Z. A. Ren, J. Yang, W. Lu, W. Yi, G. C. Che, X. L. Dong, L. L. Sun, and Z. X. Zhao, "Superconductivity at 52 K in iron based F doped layered quaternary compound Pr[O1-xFx]FeAs," *Mater. Res. Innovations,* vol. 12, pp. 105-106, 2008.

[18] J. Yang, Z. C. Li, W. Lu, W. Yi, X. L. Shen, Z. A. Ren, G. C. Che, X. L. Dong, L. L. Sun, F. Zhou, and Z. X. Zhao, "Superconductivity at 53.5 K in GdFeAsO(1-delta)," *Supercond. Sci. Technol.,* vol. 21, 2008.

[19] M. Rotter, M. Tegel, and D. Johrendt, "Superconductivity at 38 K in the iron arsenide (Ba(1-x)K(x))Fe(2)As(2)," *Phys Rev Lett,* vol. 101, 2008.

[20] Y. Kamihara, H. Hiramatsu, M. Hirano, R. Kawamura, H. Yanagi, T. Kamiya, and H. Hosono, "Iron-based layered superconductor: LaOFeP," *J Am Chem Soc,* vol. 128, pp. 10012-10013, 2006.

[21] Y. Kamihara, T. Watanabe, M. Hirano, and H. Hosono, "Iron-based layered superconductor La[O1-xFx]FeAs (x=0.05-0.12) with T-c=26 K," *J Am Chem Soc,* vol. 130, pp. 3296-+, 2008.

[22] H. Takahashi, K. Igawa, K. Arii, Y. Kamihara, M. Hirano, and H. Hosono, "Superconductivity at 43 K in an iron-based layered compound LaO1-xFxFeAs," *Nature,* vol. 453, pp. 376-378, 2008.

[23] X. H. Chen, T. Wu, G. Wu, R. H. Liu, H. Chen, and D. F. Fang, "Superconductivity at 43 K in SmFeAsO(1-x)F(x)," *Nature,* vol. 453, pp. 761-762, 2008.

[24] X. C. Wang, Q. Q. Liu, Y. X. Lv, W. B. Gao, L. X. Yang, R. C. Yu, F. Y. Li, and C. Q. Jin, "The superconductivity at 18 K in LiFeAs system," *Solid State Commun,* vol. 148, pp. 538-540, 2008.

[25] F. C. Hsu, J. Y. Luo, K. W. Yeh, T. K. Chen, T. W. Huang, P. M. Wu, Y. C. Lee, Y. L. Huang, Y. Y. Chu, D. C. Yan, and M. K. Wu, "Superconductivity in the PbO-type structure alpha-FeSe," *Proc. Natl. Acad. Sci. U. S. A.,* vol. 105, pp. 14262-14264, 2008.

[26] C. W. Chu, F. Chen, M. Gooch, A. M. Guloy, B. Lorenz, B. Lv, K. Sasmal, Z. J. Tang, J. H. Tapp, and Y. Y. Xue, "The synthesis and characterization of LiFeAs and NaFeAs," *Physica C,* vol. 469, pp. 326-331, 2009.

[27] Y. Mizuguchi, F. Tomioka, S. Tsuda, T. Yamaguchi, and Y. Takano, "Substitution Effects on FeSe Superconductor," *J Phys Soc Jpn,* vol. 78, p. 074712, 2009.

[28] Y. Mizuguchi, F. Tomioka, S. Tsuda, T. Yamaguchi, and Y. Takano, "Superconductivity at 27 K in tetragonal FeSe under high pressure," *Appl Phys Lett,* vol. 93, p. 152505, 2008.

[29] A. Gurevich, "To use or not to use cool superconductors?," *Nat Mater,* vol. 10, pp. 255-259, 2011.

[30] H. H. Wen and S. L. Li, "Materials and Novel Superconductivity in Iron Pnictide Superconductors," *Annu Rev Conden Ma P,* vol. 2, pp. 121-140, 2011.

[31] S. Medvedev, T. M. McQueen, I. A. Troyan, T. Palasyuk, M. I. Eremets, R. J. Cava, S. Naghavi, F. Casper, V. Ksenofontov, G. Wortmann, and C. Felser, "Electronic and magnetic phase diagram of beta-Fe1.01Se with superconductivity at 36.7 K under pressure," *Nat Mater,* vol. 8, pp. 630-633, 2009.

[32] J. H. Tapp, Z. J. Tang, B. Lv, K. Sasmal, B. Lorenz, P. C. W. Chu, and A. M. Guloy, "LiFeAs: An intrinsic FeAs-based superconductor with Tc=18 K," *Phys Rev B,* vol. 78, p. 060505(R), 2008.

[33] H. H. Wen, G. Mu, L. Fang, H. Yang, and X. Y. Zhu, "Superconductivity at 25K in hole-doped (La(1-x)Sr4(x)) OFeAs," *Epl-Europhys Lett,* vol. 82, 2008.

[34] Y. Yin, M. Zech, T. L. Williams, X. F. Wang, G. Wu, X. H. Chen, and J. E. Hoffman, "Scanning Tunneling Spectroscopy and Vortex Imaging in the Iron Pnictide Superconductor BaFe1.8Co0.2As2," *Phys Rev Lett,* vol. 102, 2009.

[35] Z. Ren, Q. Tao, S. A. Jiang, C. M. Feng, C. Wang, J. H. Dai, G. H. Cao, and Z. A. Xu, "Superconductivity Induced by Phosphorus Doping and Its Coexistence with Ferromagnetism in EuFe2(As0.7P0.3)(2)," *Phys Rev Lett,* vol. 102, 2009.

[36] N. Hamdadou, J. C. Bernede, and A. Khelil, "Preparation of iron selenide films by selenization technique," *J Cryst Growth,* vol. 241, pp. 313-319, 2002.

[37] S. Margadonna, Y. Takabayashi, Y. Ohishi, Y. Mizuguchi, Y. Takano, T. Kagayama, T. Nakagawa, M. Takata, and K. Prassides, "Pressure evolution of the low-temperature crystal structure and bonding of the superconductor FeSe (T-c=37 K)," *Phys Rev B,* vol. 80, p. 064506, 2009.

[38] Adrian Cho, "The Hot Question: How New Are The New Superconductors?," *Science,* vol. 320, pp. 870-871, 2008.

[39] G. Logvenov, A. Gozar, and I. Bozovic, "High-Temperature Superconductivity in a Single Copper-Oxygen Plane," *Science,* vol. 326, pp. 699-702, 2009.

[40] T. M. McQueen, Q. Huang, V. Ksenofontov, C. Felser, Q. Xu, H. Zandbergen, Y. S. Hor, J. Allred, A. J. Williams, D. Qu, J. Checkelsky, N. P. Ong, and R. J. Cava, "Extreme sensitivity of superconductivity to stoichiometry in Fe1+delta Se," *Phys Rev B,* vol. 79, p. 014522, 2009.

[41] J. Janaki, T. G. Kumary, A. Mani, S. Kalavathi, G. V. R. Reddy, G. V. N. Rao, and A. Bharathi, "Synthesis, characterization and low temperature studies of iron chalcogenide superconductors," *J Alloy Compd,* vol. 486, pp. 37-41, 2009.

[42] S. Agatsuma, K. Yamagishi, S. Takeda, and M. Naito, "MBE growth of FeSe and Sr1-xKxFe2As2," *Physica C,* p. 1468, 2010.

[43] T. M. McQueen, A. J. Williams, P. W. Stephens, J. Tao, Y. Zhu, V. Ksenofontov, F. Casper, C. Felser, and R. J. Cava, "Tetragonal-to-Orthorhombic Structural Phase Transition at 90 K in the Superconductor Fe1.01Se," *Phys Rev Lett,* vol. 103, p. 057002 2009.

[44] K. Horigane, H. Hiraka, and K. Ohoyama, "Relationship between Structure and Superconductivity in FeSe1-xTex," *J Phys Soc Jpn,* vol. 78, p. 074718 2009.

[45] Y. F. Nie, E. Brahimi, J. I. Budnick, W. A. Hines, M. Jain, and B. O. Wells, "Suppression of superconductivity in FeSe films under tensile strain," *Appl Phys Lett,* vol. 94, p. 242505, 2009.

[46] T. Imai, K. Ahilan, F. L. Ning, T. M. McQueen, and R. J. Cava, "Why Does Undoped FeSe Become a High-T-c Superconductor under Pressure?," *Phys Rev Lett,* vol. 102, p. 177005, 2009.

[47] E. Bellingeri, R. Buzio, A. Gerbi, D. Marrè, S. Congiu, M. R. Cimberle, M. Tropeano, A. S. Siri, A. Palenzona, and C. Ferdeghini, "High quality epitaxial FeSe0. 5Te0. 5 thin films grown on SrTiO3 substrates by pulsed laser deposition," *Supercond. Sci. Technol.,* vol. 22, p. 105007, 2009.

[48] C. Felser, S. Medvedev, T. M. McQueen, I. A. Troyan, T. Palasyuk, M. I. Eremets, R. J. Cava, S. Naghavi, F. Casper, V. Ksenofontov, and G. Wortmann, "Electronic and magnetic phase diagram of beta-Fe(1.01)Se with superconductivity at 36.7 K under pressure," *Nat Mater,* vol. 8, pp. 630-633, 2009.

[49] T. W. Huang, T. K. Chen, K. W. Yeh, C. T. Ke, C. L. Chen, Y. L. Huang, F. C. Hsu, M. K. Wu, P. M. Wu, M. Avdeev, and A. J. Studer, "Doping-driven structural phase transition and loss of superconductivity in M(x)Fe(1-x)Se(delta) (M=Mn, Cu)," *Phys Rev B,* vol. 82, p. 104502 2010.

[50] A. M. Zhang, T. L. Xia, L. R. Kong, J. H. Xiao, and Q. M. Zhang, "Effects on superconductivity of transition-metal doping in FeSe(0.5)Te(0.5)," *J. Phys.: Condens. Matter,* vol. 22, p. 245701, 2010.

[51] Z. Shermadini, A. Krzton-Maziopa, M. Bendele, R. Khasanov, H. Luetkens, K. Conder, E. Pomjakushina, S. Weyeneth, V. Pomjakushin, O. Bossen, and A. Amato, "Coexistence of Magnetism and Superconductivity in the Iron-Based Compound Cs(0.8)(FeSe(0.98))(2)," *Phys Rev Lett,* vol. 106, p. 117602 2011.

[52] J. G. Guo, S. F. Jin, G. Wang, S. C. Wang, K. X. Zhu, T. T. Zhou, M. He, and X. L. Chen, "Superconductivity in the iron selenide K(x)Fe(2)Se(2) (0 <= x <= 1.0)," *Phys Rev B,* vol. 82, p. 180520 2010.

[53] S. B. Zhang, Y. P. Sun, X. D. Zhu, X. B. Zhu, B. Swang, H. Lei, X. Luo, Z. R. Yang, W. H. Song, and J. M. Dai, "Crystal growth and superconductivity of FeSex," *Supercond. Sci. Technol.,* vol. 22, p. 015020, 2009.

[54] M. J. Wang, J. Y. Luo, T. W. Huang, H. H. Chang, T. K. Chen, F. C. Hsu, C. T. Wu, P. M. Wu, A. M. Chang, and M. K. Wu, "Crystal Orientation and Thickness Dependence of the Superconducting Transition Temperature of Tetragonal FeSe1-x Thin Films," *Phys Rev Lett,* vol. 103, p. 117002, 2009.

[55] Y. Han, W. Y. Li, L. X. Cao, S. Zhang, B. Xu, and B. R. Zhao, "Preparation and superconductivity of iron selenide thin films," *J. Phys.: Condens. Matter,* vol. 21, p. 235702, 2009.

[56] C. S. Weber, C. T. Reis, A. Dada, T. Masuda, and J. Moscovic, "Overview of the underground 34.5 kV HTS power cable program in Albany, NY," *Ieee T Appl Supercon,* vol. 15, pp. 1793-1797, 2005.

[57] K. W. Lee, V. Pardo, and W. E. Pickett, "Magnetism driven by anion vacancies in superconducting alpha -FeSe_{1-x}," *Phys Rev B,* vol. 78, p. 174502, 2008.

[58] T. Taen, Y. Tsuchiya, Y. Nakajima, and T. Tamegai, "Characterization of superconductivity in FeTe(0.61)Se(0.39) single crystal with T(c) similar to 14 K," *Physica C (Amsterdam, Neth.),* vol. 470, pp. S391-S393, 2010.

[59] C. S. Yadav and P. L. Paulose, "Upper critical field, lower critical field and critical current density of FeTe(0.60)Se(0.40) single crystals," *New J. Phys.,* vol. 11, p. 103046 2009.

[60] A. Subedi, L. J. Zhang, D. J. Singh, and M. H. Du, "Density functional study of FeS, FeSe, and FeTe: Electronic structure, magnetism, phonons, and superconductivity," *Phys Rev B,* vol. 78, p. 134514 2008.

[61] Y. Mizuguchi, F. Tomioka, S. Tsuda, T. Yamaguchi, and Y. Takano, "Superconductivity in S-substituted FeTe," *Appl Phys Lett,* vol. 94, p. 012503 2009.

[62] K. Deguchi, Y. Mizuguchi, S. Ogawara, T. Watanabe, S. Tsuda, T. Yamaguchi, and Y. Takano, "Air-exposure effects of superconductivity in Fe (Te, S)," *Physica C,* p. doi:10.1016/j.physc.2009.10.124, 2009.

[63] E. Bellingeri, I. Pallecchi, R. Buzio, A. Gerbi, D. Marre, M. R. Cimberle, M. Tropeano, M. Putti, A. Palenzona, and C. Ferdeghini, "T(c)=21 K in epitaxial FeSe(0.5)Te(0.5) thin films with biaxial compressive strain," *Appl Phys Lett,* vol. 96, 2010.

[64] C. S. Yadav and P. L. Paulose, "The flux pinning force and vortex phase diagram of single crystal FeTe(0.60)Se(0.40)," *Solid State Commun,* vol. 151, pp. 216-218, 2011.

[65] V. Tsurkan, J. Deisenhofer, A. Gunther, C. Kant, M. Klemm, H. A. K. von Nidda, F. Schrettle, and A. Loidl, "Physical properties of FeSe(0.5)Te(0.5) single crystals grown under different conditions," *Eur. Phys. J. B,* vol. 79, pp. 289-299, 2011.

[66] M. Eisterer, R. Raunicher, H. W. Weber, E. Bellingeri, M. R. Cimberle, I. Pallecchi, M. Putti, and C. Ferdeghini, "Anisotropic critical currents in FeSe(0.5)Te(0.5) films and the influence of neutron irradiation," *Supercond. Sci. Technol.,* vol. 24, p. 065016, 2011.

[67] W. D. Si, J. Zhou, Q. Jie, I. Dimitrov, V. Solovyov, P. D. Johnson, J. Jaroszynski, V. Matias, C. Sheehan, and Q. Li, "Iron-chalcogenide

FeSe(0.5)Te(0.5) coated superconducting tapes for high field applications," *Appl Phys Lett,* vol. 98, p. 262509 2011.

[68] S. M. Rao, B. H. Mok, M. C. Ling, C. T. Ke, T. K. Chen, I. M. Tsai, Y. L. Lin, H. L. Liu, C. L. Chen, F. C. Hsu, T. W. Huang, T. B. Wu, and M. K. Wu, "Convective solution transport - An improved technique for the growth of big crystals of the superconducting alpha-FeSe using KCl as solvent," *J Appl Phys,* vol. 110, 2011.

[69] B. C. Sales, A. S. Sefat, M. A. McGuire, R. Y. Jin, D. Mandrus, and Y. Mozharivskyj, "Bulk superconductivity at 14 K in single crystals of Fe1+yTexSe1-x," *Phys Rev B,* vol. 79, 2009.

[70] A. R. Lennie, S. A. T. Redfern, P. F. Schofield, and D. J. Vaughan, "Synthesis and Rietveld crystal structure refinement of mackinawite, tetragonal FeS," *Mineral. Mag.,* vol. 59, pp. 677-683, 1995.

[71] F. Gronvold, H. Haraldsen, and J. Vihovde, "Phase and Structural Relations in the System Iron Tellurium," *Acta Chem Scand,* vol. 8, pp. 1927-1942, 1954.

[72] M. H. Fang, H. M. Pham, B. Qian, T. J. Liu, E. K. Vehstedt, Y. Liu, L. Spinu, and Z. Q. Mao, "Superconductivity close to magnetic instability in Fe(Se1-xTex)(0.82)," *Phys Rev B,* vol. 78, 2008.

[73] K. W. Yeh, T. W. Huang, Y. L. Huang, T. K. Chen, F. C. Hsu, P. M. Wu, Y. C. Lee, Y. Y. Chu, C. L. Chen, J. Y. Luo, D. C. Yan, and M. K. Wu, "Tellurium substitution effect on superconductivity of the alpha-phase iron selenide," *Epl-Europhys Lett,* vol. 84, 2008.

[74] S. L. Li, C. de la Cruz, Q. Huang, Y. Chen, J. W. Lynn, J. P. Hu, Y. L. Huang, F. C. Hsu, K. W. Yeh, M. K. Wu, and P. C. Dai, "First-order magnetic and structural phase transitions in Fe1+ySexTe1-x," *Phys Rev B,* vol. 79, 2009.

[75] Y. Mizuguchi and Y. Takano, "Review of Fe Chalcogenides as the Simplest Fe-Based Superconductor," *J Phys Soc Jpn,* vol. 79, 2010.

[76] Y. Mizuguchi, K. Deguchi, S. Tsuda, T. Yamaguchi, and Y. Takano, "Moisture-induced superconductivity in FeTe0.8S0.2," *Phys Rev B,* vol. 81, 2010.

[77] Y. Mizuguchi, K. Deguchi, S. Tsuda, T. Yamaguchi, and Y. Takano, "Evolution of superconductivity by oxygen annealing in FeTe0.8S0.2," *Epl-Europhys Lett,* vol. 90, 2010.

[78] M. K. Wu, F. C. Hsu, K. W. Yeh, T. W. Huang, J. Y. Luo, M. J. Wang, H. H. Chang, T. K. Chen, S. M. Rao, B. H. Mok, C. L. Chen, Y. L. Huang, C. T. Ke, P.

M. Wu, A. M. Chang, C. T. Wu, and T. P. Perng, "The development of the superconducting PbO-type beta-FeSe and related compounds," *Physica C,* vol. 469, pp. 340-349, 2009.

[79] E. L. Thomas, W. Wong-Ng, D. Phelan, and J. N. Millican, "Thermopower of Co-doped FeSe," *J Appl Phys,* vol. 105, 2009.

[80] A. J. Williams, T. M. McQueen, V. Ksenofontov, C. Felser, and R. J. Cava, "The metal-insulator transition in Fe1.01-xCuxSe," *J. Phys.: Condens. Matter,* vol. 21, 2009.

[81] A. Gunther, J. Deisenhofer, C. Kant, H. A. K. von Nidda, V. Tsurkan, and A. Loidl, "Improvement of superconducting properties of FeSe0.5Te0.5 single crystals by Mn substitution," *Supercond. Sci. Technol.,* vol. 24, 2011.

[82] Y. Mizuguchi, Y. Hara, K. Deguchi, S. Tsuda, T. Yamaguchi, K. Takeda, H. Kotegawa, H. Tou, and Y. Takano, "Anion height dependence of T(c) for the Fe-based superconductor," *Supercond. Sci. Technol.,* vol. 23, p. 054013, 2010.

[83] A. F. Wang, J. J. Ying, Y. J. Yan, R. H. Liu, X. G. Luo, Z. Y. Li, X. F. Wang, M. Zhang, G. J. Ye, P. Cheng, Z. J. Xiang, and X. H. Chen, "Superconductivity at 32 K in single-crystalline RbxFe2-ySe2," *Phys Rev B,* vol. 83, 2011.

[84] A. Krzton-Maziopa, Z. Shermadini, E. Pomjakushina, V. Pomjakushin, M. Bendele, A. Amato, R. Khasanov, H. Luetkens, and K. Conder, "Synthesis and crystal growth of Cs-0.8(FeSe0.98)2: a new iron-based superconductor with T-c=27 K," *J. Phys.: Condens. Matter,* vol. 23, 2011.

[85] J. Nagamatsu, N. Nakagawa, T. Muranaka, Y. Zenitani, and J. Akimitsu, "Superconductivity at 39 K in magnesium diboride," *Nature,* vol. 410, pp. 63-64, 2001.

[86] A. Y. Ganin, Y. Takabayashi, Y. Z. Khimyak, S. Margadonna, A. Tamai, M. J. Rosseinsky, and K. Prassides, "Bulk superconductivity at 38K in a molecular system," *Nat Mater,* vol. 7, pp. 367-371, 2008.

[87] S. Masaki, H. Kotegawa, Y. Hara, H. Tou, K. Murata, Y. Mizuguchi, and Y. Takano, "Precise Pressure Dependence of the Superconducting Transition Temperature of FeSe: Resistivity and Se-77-NMR Study," *J Phys Soc Jpn,* vol. 78, 2009.

[88] C. H. Lee, A. Iyo, H. Eisaki, H. Kito, M. T. Fernandez-Diaz, T. Ito, K. Kihou, H. Matsuhata, M. Braden, and K. Yamada, "Effect of structural parameters on superconductivity in fluorine-free LnFeAsO1-y (Ln = La, Nd)," *J Phys Soc Jpn,* vol. 77, 2008.

[89] N. C. Gresty, Y. Takabayashi, A. Y. Ganin, M. T. McDonald, J. B. Claridge, D. Giap, Y. Mizuguchi, Y. Takano, T. Kagayama, Y. Ohishi, M. Takata, M. J. Rosseinsky, S. Margadonna, and K. Prassides, "Structural Phase Transitions and Superconductivity in Fe1+delta Se0.57Te0.43 at Ambient and Elevated Pressures," *J Am Chem Soc,* vol. 131, pp. 16944-16952, 2009.

[90] K. Horigane, N. Takeshita, C. H. Lee, H. Hiraka, and K. Yamada, "First Investigation of Pressure Effects on Transition from Superconductive to Metallic Phase in FeSe0.5Te0.5," *J Phys Soc Jpn,* vol. 78, 2009.

[91] Y. Mizuguchi, F. Tomioka, K. Deguchi, S. Tsuda, T. Yamaguchi, and Y. Takano, "Pressure effects on FeSe family superconductors," *Physica C,* vol. 470, pp. S353-S355, 2010.

[92] K. Kuroki, H. Usui, S. Onari, R. Arita, and H. Aoki, "Pnictogen height as a possible switch between high-T-c nodeless and low-T-c nodal pairings in the iron-based superconductors," *Phys Rev B,* vol. 79, 2009.

[93] M. Tegel, C. Löhnert, and D. Johrendt, "The crystal structure of FeSe0.44Te0.56," *Solid State Commun,* vol. 150, pp. 383-385, 2010.

[94] S. A. Baily, Y. Kohama, H. Hiramatsu, B. Maiorov, F. F. Balakirev, M. Hirano, and H. Hosono, "Pseudoisotropic Upper Critical Field in Cobalt-Doped SrFe2As2 Epitaxial Films," *Phys Rev Lett,* vol. 102, 2009.

[95] H. Hiramatsu, T. Katase, T. Kamiya, M. Hirano, and H. Hosono, "Superconductivity in Epitaxial Thin Films of Co-Doped SrFe2As2 with Bilayered FeAs Structures and their Magnetic Anisotropy," *Appl Phys Express,* vol. 1, 2008.

[96] S. Lee, J. Jiang, Y. Zhang, C. W. Bark, J. D. Weiss, C. Tarantini, C. T. Nelson, H. W. Jang, C. M. Folkman, S. H. Baek, A. Polyanskii, D. Abraimov, A. Yamamoto, J. W. Park, X. Q. Pan, E. E. Hellstrom, D. C. Larbalestier, and C. B. Eom, "Template engineering of Co-doped BaFe2As2 single-crystal thin films," *Nat Mater,* vol. 9, pp. 397-402, 2010.

[97] T. K. Chen, J. Y. Luo, C. T. Ke, H. H. Chang, T. W. Huang, K. W. Yeh, C. C. Chang, P. C. Hsu, C. T. Wu, M. J. Wang, and M. K. Wu, "Low-temperature fabrication of superconducting FeSe thin films by pulsed laser deposition," *Thin Solid Films,* vol. 519, pp. 1540-1545, 2010.

[98] Y. Imai, R. Tanaka, T. Akiike, M. Hanawa, I. Tsukada, and A. Maeda, "Superconductivity of FeSe0.5Te0.5 Thin Films Grown by Pulsed Laser Deposition," *Jpn J Appl Phys,* vol. 49, 2010.

[99] T. G. Kumary, D. K. Baisnab, J. Janaki, A. Mani, A. T. Satya, R. M. Sarguna, P. K. Ajikumar, A. K. Tyagi, and A. Bharathi, "Superconducting Fe1+delta Se1-xTex thin films: growth, characterization and properties," *Supercond. Sci. Technol.,* vol. 22, 2009.

[100] L. Chen, C. F. Tsai, Y. Y. Zhu, Z. X. Bi, and H. Y. Wang, "Enhanced superconducting properties in epitaxial FeSe thin films with self-assembled Fe(3)O(4) nanoparticles," *Physica C,* vol. 471, pp. 515-519, 2011.

[101] M. Jourdan and S. ten Haaf, "Preparation, characterization, and upper critical field of epitaxial FeSe thin films," *J Appl Phys,* vol. 108, p. 023913, 2010.

[102] W. D. Si, Z. W. Lin, Q. Jie, W. G. Yin, J. Zhou, G. D. Gu, P. D. Johnson, and Q. Li, "Enhanced superconducting transition temperature in FeSe(0.5)Te(0.5) thin films," *Appl Phys Lett,* vol. 95, p. 052504, 2009.

[103] Y. Han, W. Y. Li, L. X. Cao, X. Y. Wang, B. Xu, B. R. Zhao, Y. Q. Guo, and J. L. Yang, "Superconductivity in Iron Telluride Thin Films under Tensile Stress," *Phys Rev Lett,* vol. 104, 2010.

[104] W. D. Si, Q. Jie, L. J. Wu, J. Zhou, G. D. Gu, P. D. Johnson, and Q. Li, "Superconductivity in epitaxial thin films of Fe1.08Te:O-x," *Phys Rev B,* vol. 81, 2010.

[105] Y. F. Nie, D. Telesca, J. I. Budnick, B. Sinkovic, and B. O. Wells, "Superconductivity induced in iron telluride films by low-temperature oxygen incorporation," *Phys Rev B,* vol. 82, 2010.

[106] Soon-Gil Jung, N. H. Lee, Eun-Mi Choi, W. N. Kang, Sung-Ik Lee, Tae-Jong Hwang, and D. H. Kim, "Fabrication of FeSe1−x superconducting films with bulk properties," *Physica C,* vol. 470, pp. 1977-1980, 2010.

[107] Q. Y. Wang, Z. Li, W. H. Zhang, Z. C. Zhang, J. S. Zhang, W. Li, H. Ding, Y. B. Ou, P. Deng, K. Chang, J. Wen, C. L. Song, K. He, J. F. Jia, S. H. Ji, Y. Y. Wang, L. L. Wang, X. Chen, X. C. Ma, and Q. K. Xue, "Interface-Induced High-Temperature Superconductivity in Single Unit-Cell FeSe Films on SrTiO3," *Chinese Phys Lett,* vol. 29, 2012.

[108] A. Kreyssig, M. A. Green, Y. Lee, G. D. Samolyuk, P. Zajdel, J. W. Lynn, S. L. Bud'ko, M. S. Torikachvili, N. Ni, S. Nandi, J. B. Leão, S. J. Poulton, D. N. Argyriou, B. N. Harmon, R. J. McQueeney, P. C. Canfield, and A. I. Goldman, "Pressure-induced volume-collapsed tetragonal phase of CaFe_{2}As_{2} as seen via neutron scattering," *Phys Rev B,* vol. 78, p. 184517, 2008.

[109] I. Tsukada, M. Hanawa, T. Akiike, F. Nabeshima, Y. Imai, A. Ichinose, S. Komiya, T. Hikage, T. Kawaguchi, H. Ikuta, and A. Maeda, "Epitaxial Growth of FeSe0.5Te0.5 Thin Films on CaF2 Substrates with High Critical Current Density," *Appl Phys Express,* vol. 4, p. 053101, 2011.

[110] A. J. Drew, C. Niedermayer, P. J. Baker, F. L. Pratt, S. J. Blundell, T. Lancaster, R. H. Liu, G. Wu, X. H. Chen, I. Watanabe, V. K. Malik, A. Dubroka, M. Rossle, K. W. Kim, C. Baines, and C. Bernhard, "Coexistence of static magnetism and superconductivity in SmFeAsO1-xFx as revealed by muon spin rotation," *Nat Mater,* vol. 8, pp. 310-314, 2009.

[111] J. T. Park, D. S. Inosov, C. Niedermayer, G. L. Sun, D. Haug, N. B. Christensen, R. Dinnebier, A. V. Boris, A. J. Drew, L. Schulz, T. Shapoval, U. Wolff, V. Neu, X. P. Yang, C. T. Lin, B. Keimer, and V. Hinkov, "Electronic Phase Separation in the Slightly Underdoped Iron Pnictide Superconductor Ba1-xKxFe2As2," *Phys Rev Lett,* vol. 102, 2009.

[112] L. Chen, C. F. Tsai, J. H. Lee, X. H. Zhang, and H. Y. Wang, "Highly Textured Superconducting FeSe0.5Te0.5 Thin Films on Glass Substrates," *Jpn J Appl Phys,* vol. 52, 2013.

[113] Li Chen, Chen-Fong Tsai, Aiping Chen, Qing Su, and Haiyan Wang, "Growth and Pinning Properties of Superconducting Nanostructured FeSe0.5Te0.5 Thin Films on Amorphous Substrates," *Ieee T Appl Supercon,* vol. 23, p. 7500904 2012.

[114] Weidong Si, Su Jung Han, Xiaoya Shi, Steven N Ehrlich, J Jaroszynski, Amit Goyal, and Qiang Li, "High current superconductivity in FeSe0. 5Te0. 5-coated conductors at 30 tesla," *Nature communications,* vol. 4, p. 1347, 2013.

[115] M.N. Wilson, *Superconducting Magnets*: Oxford University Press, Incorporated, 1987.

[116] S. R. Foltyn, L. Civale, J. L. Macmanus-Driscoll, Q. X. Jia, B. Maiorov, H. Wang, and M. Maley, "Materials science challenges for high-temperature superconducting wire," *Nat Mater,* vol. 6, pp. 631-642, 2007.

[117] A. Goyal, D. P. Norton, J. D. Budai, M. Paranthaman, E. D. Specht, D. M. Kroeger, D. K. Christen, Q. He, B. Saffian, F. A. List, D. F. Lee, P. M. Martin, C. E. Klabunde, E. Hartfield, and V. K. Sikka, "High critical current density superconducting tapes by epitaxial deposition of YBa2Cu3Ox thick films on biaxially textured metals," *Appl Phys Lett,* vol. 69, pp. 1795-1797, 1996.

[118] S. R. Foltyn, P. N. Arendt, P. C. Dowden, R. F. DePaula, J. R. Groves, J. Y. Coulter, Q. X. Jia, M. P. Maley, and D. E. Peterson, "High-T-c coated conductors

- Performance of meter-long YBCO/IBAD flexible tapes," *Ieee T Appl Supercon,* vol. 9, pp. 1519-1522, 1999.

[119] A. P. Malozemoff, S. Annavarapu, L. Fritzemeier, Q. Li, V. Prunier, M. Rupich, C. Thieme, W. Zhang, A. Goyal, M. Paranthaman, and D. F. Lee, "Low-cost YBCO coated conductor technology," *Supercond. Sci. Technol.,* vol. 13, pp. 473-476, 2000.

[120] M. S. Bhuiyan, M. Paranthaman, S. Sathyamurthy, T. Aytug, S. Kang, D. F. Lee, A. Goyal, E. A. Payzant, and K. Salama, "MOD approach for the growth of epitaxial CeO2 buffer layers on biaxially textured Ni-W substrates for YBCO coated conductors," *Supercond. Sci. Technol.,* vol. 16, pp. 1305-1309, 2003.

[121] S. Lee, J. Jiang, J. D. Weiss, C. M. Folkman, C. W. Bark, C. Tarantini, A. Xu, D. Abraimov, A. Polyanskii, C. T. Nelson, Y. Zhang, S. H. Baek, H. W. Jang, A. Yamamoto, F. Kametani, X. Q. Pan, E. E. Hellstrom, A. Gurevich, C. B. Eom, and D. C. Larbalestier, "Weak-link behavior of grain boundaries in superconducting Ba(Fe(1-x)Co(x))(2)As(2) bicrystals," *Appl Phys Lett,* vol. 95, p. 212505, 2009.

[122] T. Ozaki, Y. Mizuguchi, S. Demura, K. Deguchi, Y. Kawasaki, T. Watanabe, H. Okazaki, H. Hara, H. Takeya, T. Yamaguchi, H. Kumakura, and Y. Takano, "Enhancement of superconducting properties in FeSe wires using a quenching technique," *J Appl Phys,* vol. 111, 2012.

[123] T. Ozaki, K. Deguchi, Y. Mizuguchi, Y. Kawasaki, T. Tanaka, T. Yamaguchi, S. Tsuda, H. Kumakura, and Y. Takano, "Transport properties and microstructure of mono- and seven-core wires of FeSe(1-x)Te(x) superconductor produced by the Fe-diffusion powder-in-tube method," *Supercond. Sci. Technol.,* vol. 24, p. 105002, 2011.

[124] Z. Chen, F. Kametani, Y. Chen, Y. Xie, V. Selvamanickam, and D. C. Larbalestier, "A high critical current density MOCVD coated conductor with strong vortex pinning centers suitable for very high field use," *Supercond. Sci. Technol.,* vol. 22, 2009.

[125] D. C. Larbalestier and A. W. West, "New Perspectives on Flux Pinning in Niobium-Titanium Composite Superconductors," *Acta Metall Mater,* vol. 32, pp. 1871-1881, 1984.

[126] L. D. Cooley, P. J. Lee, and D. C. Larbalestier, "Flux-pinning mechanism of proximity-coupled planar defects in conventional superconductors: Evidence that magnetic pinning is the dominant pinning mechanism in niobium-titanium alloy," *Phys Rev B,* vol. 53, pp. 6638-6652, 1996.

[127] R. M. Scanlan, W. A. Fietz, and E. F. Koch, "Flux Pinning Centers in Superconducting Nb3sn," *J Appl Phys,* vol. 46, pp. 2244-2249, 1975.

[128] A. Godeke, "A review of the properties of Nb3Sn and their variation with A15 composition, morphology and strain state," *Supercond. Sci. Technol.,* vol. 19, pp. R68-R80, 2006.

[129] J. W. Ekin, "Unified scaling law for flux pinning in practical superconductors: I. Separability postulate, raw scaling data and parameterization at moderate strains," *Supercond. Sci. Technol.,* vol. 23, 2010.

[130] Jeremy A Good and Edward J Kramer, "Yield and recovery of the flux line lattice in a type II superconductor," *Philosophical Magazine,* vol. 24, pp. 339-357, 1971.

[131] C. F. Tsai, Y. Y. Zhu, L. Chen, and H. Y. Wang, "Correlation Between Flux Pinning Properties and Interfacial Defects in YBa(2)Cu(3)O(7-delta)/CeO(2) Multilayer Thin Films," *Ieee T Appl Supercon,* vol. 21, pp. 2758-2761, 2011.

[132] Y. Y. Zhu, L. Chen, J. Ciston, and H. Y. Wang, "Atomic-Scale Investigations of Intrinsic Chemical Inhomogeneity in Superconducting Fe1+ySe1-xTex Epitaxial Films," *J. Phys. Chem. C,* vol. 117, pp. 7170-7177, 2013.

[133] T. Yildirim, "Strong Coupling of the Fe-Spin State and the As-As Hybridization in Iron-Pnictide Superconductors from First-Principle Calculations," *Phys Rev Lett,* vol. 102, p. 037003, 2009.

[134] Q. Li, W. D. Si, and I. K. Dimitrov, "Films of iron chalcogenide superconductors," *Rep Prog Phys,* vol. 74, p. 124510, 2011.

[135] V Nelea, IN Mihailescu, M Jelinek, and R Eason, "Pulsed laser deposition of thin films: Applications-LED growth of functional materials," *Robert Eason I, Editor, J. Wiley & sons Inc., Hoboken, New Jersey,* pp. 421-456, 2007.

[136] R. K. Singh, O. W. Holland, and J. Narayan, "Theoretical-Model for Deposition of Superconducting Thin-Films Using Pulsed Laser Evaporation Technique," *J Appl Phys,* vol. 68, pp. 233-247, 1990.

[137] R. K. Singh and J. Narayan, "Pulsed-Laser Evaporation Technique for Deposition of Thin-Films - Physics and Theoretical-Model," *Phys Rev B,* vol. 41, pp. 8843-8859, 1990.

[138] T.C. Jeffrey, *History and fundamentals of pulsed laser deposition*: Wiley, New York, 1994.

[139] L. W. Martin, Y. H. Chu, and R. Ramesh, "Advances in the growth and characterization of magnetic, ferroelectric, and multiferroic oxide thin films," *Mat Sci Eng R,* vol. 68, pp. Iii-133, 2010.

[140] D. Fennell Evans Robert J. Stokes, *Fundamentals of Interfacial Engineering*. Minneapolis, MN: Wiley-VCH, 1997.

[141] J. Als-Nielsen and D. McMorrow, *Elements of Modern X-ray Physics*: Wiley, 2011.

[142] D.B. Williams and C.B. Carter, *Transmission Electron Microscopy: A Textbook for Materials Science*: Springer London, Limited, 2009.

[143] B. Fultz and J.M. Howe, *Transmission Electron Microscopy and Diffractometry of Materials*: Springer Berlin Heidelberg, 2013.

[144] H. Hiramatsu, T. Katase, T. Kamiya, M. Hirano, and H. Hosono, "Water-induced superconductivity in SrFe2As2," *Phys Rev B,* vol. 80, p. 052501, 2009.

[145] C. W. Schneider, M. Esposito, I. Marozau, K. Conder, M. Doebeli, Y. Hu, M. Mallepell, A. Wokaun, and T. Lippert, "The origin of oxygen in oxide thin films: Role of the substrate," *Appl Phys Lett,* vol. 97, p. 192107, 2010.

[146] C. F. Tsai, Y. Y. Zhu, L. Chen, and H. Y. Wang, "Flux Pinning Properties in YBCO Thin Films With Self-Aligned Magnetic Nanoparticles," *Ieee T Appl Supercon,* vol. 21, pp. 2749-2752, 2011.

[147] J. Wang, C. F. Tsai, Z. X. Bi, D. G. Naugle, and H. Y. Wang, "Microstructural and Pinning Properties of YBa(2)Cu(3)O(7-delta) Thin Films Doped With Magnetic Nanoparticles," *Ieee T Appl Supercon,* vol. 19, pp. 3503-3506, 2009.

[148] R. L. S. Emergo, F. J. Baca, J. Z. Wu, T. J. Haugan, and P. N. Barnes, "The effect of thickness and substrate tilt on the BZO splay and superconducting properties of YBa(2)Cu(3)O(7-delta) films," *Supercond. Sci. Technol.,* vol. 23, p. 115010, 2010.

[149] D. M. Feldmann, T. G. Holesinger, B. Maiorov, H. Zhou, S. R. Foltyn, J. Y. Coulter, and I. Apodoca, "1000 A cm(-1) in a 2 mu m thick YBa(2)Cu(3)O(7-x) film with BaZrO(3) and Y(2)O(3) additions," *Supercond. Sci. Technol.,* vol. 23, p. 115016, 2010.

[150] C. Tarantini, S. Lee, Y. Zhang, J. Jiang, C. W. Bark, J. D. Weiss, A. Polyanskii, C. T. Nelson, H. W. Jang, C. M. Folkman, S. H. Baek, X. Q. Pan, A. Gurevich, E. E. Hellstrom, C. B. Eom, and D. C. Larbalestier, "Strong vortex pinning in

Co-doped BaFe(2)As(2) single crystal thin films," *Appl Phys Lett,* vol. 96, p. 142510, 2010.

[151] S. R. Foltyn, H. Wang, L. Civale, Q. X. Jia, P. N. Arendt, B. Maiorov, Y. Li, M. P. Maley, and J. L. MacManus-Driscoll, "Overcoming the barrier to 1000 A/cm width superconducting coatings," *Appl Phys Lett,* vol. 87, p. 162505, 2005.

[152] D. Louca, K. Horigane, A. Llobet, R. Arita, S. Ji, N. Katayama, S. Konbu, K. Nakamura, T. Y. Koo, P. Tong, and K. Yamada, "Local atomic structure of superconducting FeSe(1-x)Te(x)," *Phys Rev B,* vol. 81, p. 134524 2010.

[153] S. X. Huang, C. L. Chien, V. Thampy, and C. Broholm, "Control of Tetrahedral Coordination and Superconductivity in FeSe(0.5)Te(0.5) Thin Films," *Phys Rev Lett,* vol. 104, p. 217002, 2010.

[154] K. Iida, J. Hanisch, M. Schulze, S. Aswartham, S. Wurmehl, B. Buchner, L. Schultz, and B. Holzapfel, "Generic Fe buffer layers for Fe-based superconductors: Epitaxial FeSe1-xTex thin films," *Appl Phys Lett,* vol. 99, p. 202503, 2011.

[155] Q. P. Ding, S. Mohan, Y. Tsuchiya, T. Taen, Y. Nakajima, and T. Tamegai, "Magneto-optical imaging and transport properties of FeSe superconducting tapes prepared by the diffusion method," *Supercond. Sci. Technol.,* vol. 25, p. 025003, 2012.

[156] L. Chen, C. F. Tsai, Y. Y. Zhu, A. P. Chen, Z. X. Bi, J. Lee, and H. Y. Wang, "Enhanced flux pinning properties in superconducting FeSe0.5Te0.5 thin films with secondary phases," *Supercond. Sci. Technol.,* vol. 25, p. 025020, 2012.

[157] Y. Imai, T. Akiike, M. Hanawa, I. Tsukada, A. Ichinose, A. Maeda, T. Hikage, T. Kawaguchi, and H. Ikuta, "Systematic Comparison of Eight Substrates in the Growth of FeSe_0. 5Te_0. 5 Superconducting Thin Films," *Appl Phys Express,* vol. 3, p. 043102, 2010.

[158] Z. S. Gao, Y. P. Qi, L. Wang, D. L. Wang, X. P. Zhang, C. Yao, and Y. W. Ma, "Superconducting properties of FeSe wires and tapes prepared by a gas diffusion technique," *Supercond. Sci. Technol.,* vol. 24, p. 065022, 2011.

[159] Y. Mizuguchi, H. Izawa, T. Ozaki, Y. Takano, and O. Miura, "Transport properties of single- and three-core FeSe wires fabricated by a novel chemical-transformation PIT process," *Supercond. Sci. Technol.,* vol. 24, p. 125003, 2011.

[160] P. Mele, K. Matsumoto, K. Fujita, Y. Yoshida, T. Kiss, A. Ichinose, and M. Mukaida, "Fe-Te-Se epitaxial thin films with enhanced superconducting properties," *Supercond. Sci. Technol.,* vol. 25, p. 084021, 2012.

[161] M. Hanawa, A. Ichinose, S. Komiya, I. Tsukada, T. Akiike, Y. Imai, T. Hikage, T. Kawaguchi, H. Ikuta, and A. Maeda, "Substrate Dependence of Structural and Transport Properties in FeSe0.5Te0.5 Thin Films," *Jpn J Appl Phys,* vol. 50, p. 053101, 2011.

[162] T. Ozaki, K. Deguchi, Y. Mizuguchi, H. Kumakura, and Y. Takano, "Microstructure and transport properties of FeTe0.5Se0.5 superconducting wires fabricated by ex-situ Powder-in-tube process," *Physica C,* vol. 471, pp. 1150-1153, 2011.

[163] Yuanyuan Zhu, Li Chen, James Ciston, and Haiyan Wang, "Atomic-Scale Investigations of Intrinsic Chemical Inhomogeneity in Superconducting Fe1+ ySe1-xTex Epitaxial Films," *J. Phys. Chem. C*.

[164] C. F. Tsai, J. H. Lee, and H. Y. Wang, "Microstructure and superconducting properties of YBa2Cu3O7-delta thin films incorporated with a self-assembled magnetic vertically aligned nanocomposite," *Supercond. Sci. Technol.,* vol. 25, 2012.